Università
degli Studi
di Ferrara

DOCTORAL COURSE IN

"PHYSICS"

CYCLE XXXIII°

DIRECTOR Prof. ELEONORA LUPPI

Use of Nanostructured Chemoresistive Sensors to Detect Tumor Cells, Analyzing Blood and Biopsy Samples and Development of a More Sophisticated Electronic Device for Sensors

Scientific/Disciplinary Sector (SDS) FIS/01

Candidate

Dott. Astolfi Michele

Supervisor

Prof. Cesare Malagù

Second Supervisor

Prof. Gabriele Anania

Years 2017/2021

Content Summary

1 Semiconductor Materials: An Overview

Semiconductor materials are characterized by an electrical conductivity falling between conductor (copper, gold, etc.) and insulator (glass, plastic, etc.) ones, that decreases with the temperature increasing, so defining a opposite behavior with respect to conductors. Semiconductors could be intrinsic or extrinsic [1]:

- intrinsic semiconductors are almost pure semiconducting materials, where the small amount of impurities ($10^{16} - 10^{18}$ acceptor/donor states density) does not affect in a determinant way their electrical behavior. All the charge carriers jump from valence to conduction band, because of thermal or optical electron excitation and, their number in conduction band is equal to the number of the holes left in valence band; this is obvious considering that the conduction electrons originate from the material pure crystalline material structural atoms themselves (Fig. 1.1a) and both electrons and holes contribute to the total current flowing. The Fermi level (i.e. the level with occupation probability equal to 1/2) is located in the middle of the gap, between conduction and valence band [2];

- Extrinsic semiconductors are obtained by introducing impurities (doping process) into the pure crystalline structure (Fig. 1.1b), so modifying their electrical properties. The carrier amount is increased introducing pentavalent (donors, i.e., they give an electron to the crystal) or tetravalent atoms (acceptors, i.e., they accept an electron from the crystal), obtaining a n-type or p-type doped semiconductor respectively. The Fermi level is located close to conduction band in the first case and to the valence band in the second one [3].

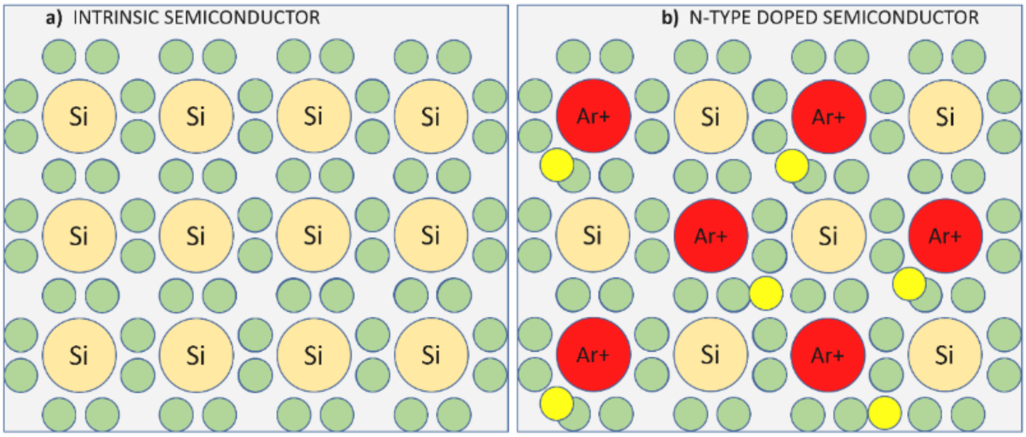

Figure 1.1: a) Intrinsic semiconductor structure: yellow and green circles are the semiconductor ions (Silicon in this example) and electrons; b) N-Type extrinsic semiconductor structure: red and yellow circles represent impurity atoms and their free electrons; green circles represent the bounded electrons.

Semiconductor junction occurs when two differently doped regions coexist in the same crystal volume. The electrical behavior of charge carriers, such as electron and holes, at the junctions is at the basis of all the modern electronics and sensor theory. The depletion approximation (DA), i.e., assumption that all' the crystal impurities are completely ionized an room temperature ($T = 300K$), has been applied here to treat with doped semiconductors; it is worth to note that DA is a rational assumption to work with the semiconductor materials of our interest [4].

In semiconductor physics, a crucial role is held by surface states, responsible for many phenomena occurring at the semiconductor surface. To highlight the real importance of the surface states in the sensor physics, they are widely treated in the next paragraph.

1.1 Surface States and Implication on Bands in Planar Geometry

Surface states are energy states, located very close to the crystal surface, energetically laying between valence and conduction band. They are generated by defects and atom rearrangements of the periodic structure of a semiconductor crystal at the surface where the regular bulk crystalline lattice terminates abruptly (it results perturbed). They outline an actual band of several acceptor and donor permitted states that can be occupied by conduction electrons with energy below Fermi Level.

Surface states, including both donor and acceptor states, are usually partially filled, so E_F is located within the surface states energy band [5].

For instance, a 2D n-Type doped semiconductor (Fig1.1.1) owns free electrons in its conduction band at room temperature. The surface states, being acceptor states, are characterized by energies lower than the conduction band ones, so the surface state electrons electrochemical potential is lower than the conduction band electrons one; this issue forces the electrons to migrate at the surface states to minimize the total energy of the system.

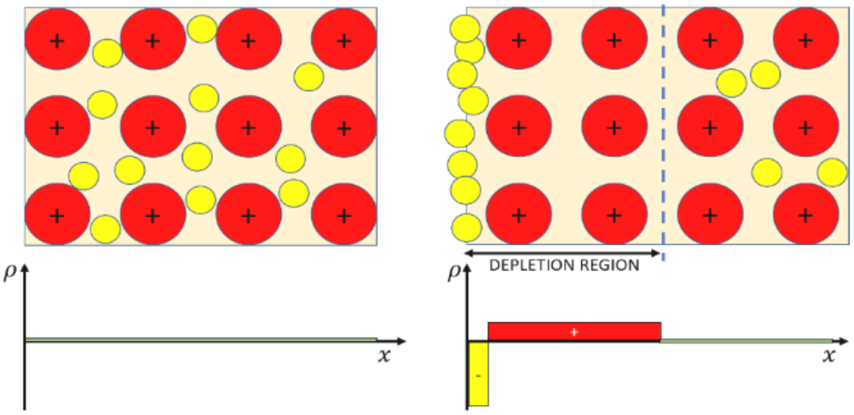

Figure 1.1.1: 2D Double Layer Effect for a n-type doped semiconductor crystal. Red and yellow circles are the doping ions and the free electrons and ρ is the charge density.

This mechanism generates a negative charge layer on the semiconductor surface and a positive charge region, so called depletion region, between the surface and the bulk (Fig. 1.1.1) [5].

The aforementioned negative charge, balanced by positive depletion region, is spread on a very thick surface layer with very low thickness leading to "**Double Layer**" configuration. The latter, representing a charge unbalance, generates an electric field, and consequently a potential difference, responsible of a surface potential barrier that hinders the in-out electron crossing (Fig 1.1.2) [6] [7].

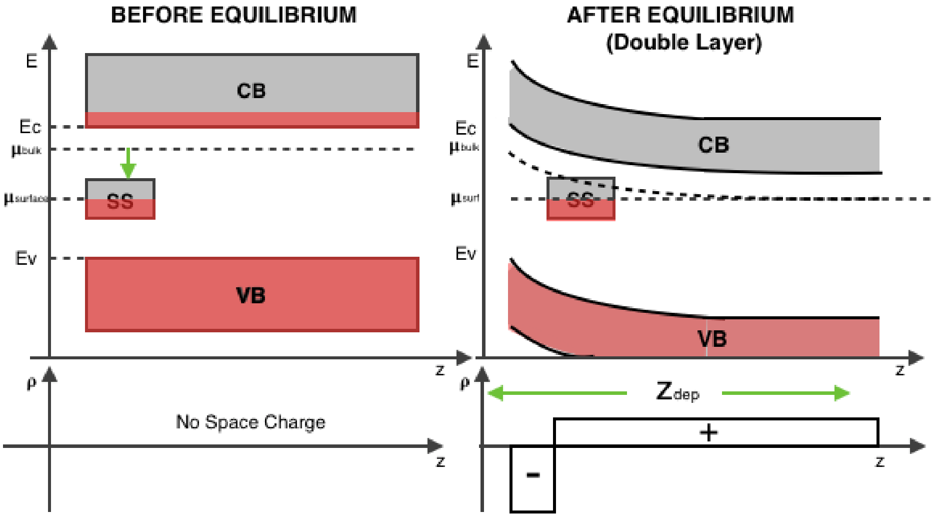

Figure 1.1.2: Band Bending Effect. CB and VB are the conduction and valence band respectively, SS is the surface state energy band.

Thick-film nanostructured metal-oxide sensing materials, on which the sensors used in this research are based, are composed by a flat and porous layer of semiconductor nanograins (with an average size of about 50-200 nm), where a 3D-double potential barrier occurs between each grains couple interface, due to the double layer effect explained above (Fig 1.1.3). The conduction band electrons have to cross several double barriers to pass through several nanograins (Fig. 1.1.3).

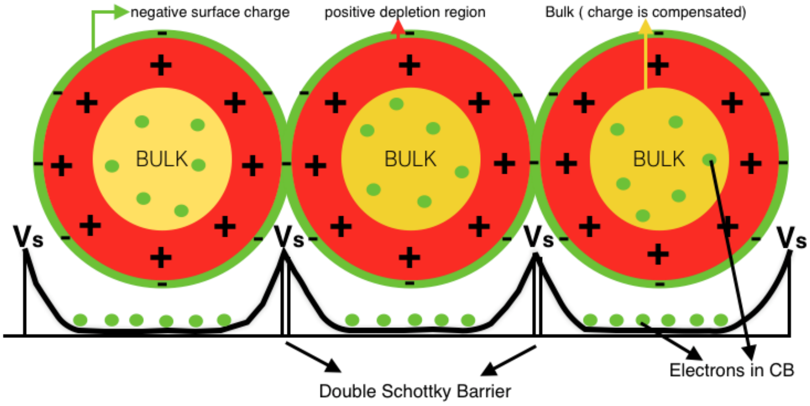

Figure 1.1.3: double layer effect and consequent potential barrier among nanograins (green, red and yellow areas are surface negative layer, positive depletion region and bulk respectively). On the bottom, stylized scheme showing electrons (green points) in conduction band and the barriers hindering the electron crossing through them.

The depletion region width for a n-Type semiconductor will be computed first in 1D, to further extend the result for 3D spherical grains.

Assuming that all semiconductor material donors or acceptors are completely ionized at $T_{room} = 300K$ (assumption always valid in semiconductors of our interest; DA), the **charge density** is:

$$\rho = qN_d \qquad (1.1.1)$$

where N_d is the impurity atom density and $q = -e$ is the electron charge.

Introducing now the 1D-Poisson equation (linking the electric potential with the charge density) and replacing ρ with (1.1.1) what outcomes is:

$$\frac{d^2\phi}{dx^2} = \frac{-eN_d}{\epsilon_r \epsilon_0} \qquad (1.1.2)$$

where ϕ is the electric potential, ϵ_r and ϵ_0 are the relative and vacuum dielectric constants respectively.

Electron electric potential as function of the distance from the surface x, $V(x)$, assuming the material uniformly doped (N_d = constant), is defined as:

$$V(x) = \phi_B - \phi(x) \qquad (1.1.3)$$

where ϕ_B is the bulk potential energy of the semiconductor [8].
Placing (1.1.3) in (1.1.2), the integration of the latter leads to the electric field relation:

$$\frac{dV(x)}{dx} = \frac{-eN_d}{\epsilon_r \epsilon_0}\left(x - x_{dep}\right) \qquad (1.1.4)$$

where x_{dep} is the space charge region thickness, determined recalling the neutrality condition for a planar charge distribution; it represents the need to have an opposite equal total charge between positive depletion and negative surface regions:

$$N_s = x_{dep} N_d \qquad (1.1.5)$$

where N_s is the surface state density.
Poisson equation is solved satisfying the electric field boundary condition, considering the fact that the electric field is equal to zero in the bulk region (1.1.6).

$$\left[\frac{dV(x)}{dx}\right]_{x=x_{dep}} = 0 \qquad (1.1.6)$$

The electric potential expression (1.1.7) comes out integrating (1.1.2) once more and stating $[V(x) = 0]_{x=x_{dep}}$ (the potential is equal to zero in the bulk region).

$$V(x) = \frac{-eN_d}{2\epsilon_r \epsilon_0}(x - x_{dep})^2 \qquad (1.1.7)$$

Solving the equation (1.1.7) at the surface ($x = 0$), the result is the so called **Schottky relation** (1.1.8), that relates the surface potential barrier Vs with the depletion region width and the donor states amount [8].

$$V_s = \frac{-eN_d}{2\epsilon_r \epsilon_0}(x_{dep})^2 \quad (1.1.8)$$

Equation (1.1.8) is also valid for p-type doped semiconductors, replacing – e and N_d with +e and N_a respectively.
A relationship between V_s, N_s, and N_d, for a n-type doped semiconductor can be written out combing (1.1.5) and (1.1.8):

$$V_s = \frac{-eN_s{}^2}{2\epsilon_r\epsilon_0 N_d} \qquad (1.1.9)$$

These results are obtained assuming a "clean" semiconductor surface (i.e., without any absorbed substance). Thinking to place the semiconductor in a real atmosphere, V_s would be affected by the surface absorbed oxygen ions ($O_2^- \; and \; O^-$) and the molecular oxygen (O_2) [7].

1.2 3D Nanograins (From Planar to 3D Geometry)

Metal-oxide nanostructured sensing film, representing the active material of the sensors employed in this work, is made by semiconductor nanograins in contact each other, well approximated with nanospheres of radius R; the passage from the planar to 3D spherical model is crucial to apply here the theory developed in the previous paragraph to spherical semiconducting nanograins, assuming the DA remains still valid.
Considering the particular symmetry, spherical coordinates will be used to solve the 3D-spherical problem.

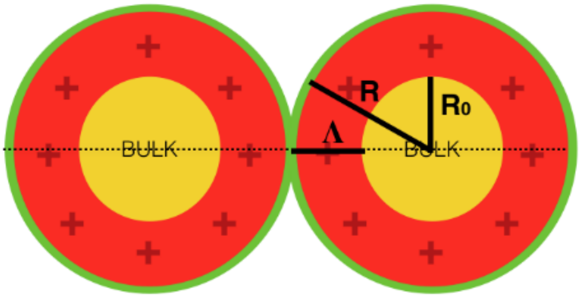

Figure 1.2.1: two nanograins in contact. R_0 and R are the bulk and grain radius, $\Lambda = R - R_0$ is the depletion region width. The green and red spherical shells represent the superficial negative charge and the positive depletion regions respectively and, the yellow nucleus is the bulk.

As first, let's consider the case where $\Lambda < R$ ($R_0 > 0$):

$$\Lambda = R - R_0 \qquad (1.2.1)$$

where Λ the depletion shell width, R and R_0 the grain and bulk radius (Fig. 1.2.1).
On this basis, the Poisson equation in polar coordinates is:

$$\frac{1}{r}\frac{d^2[r\phi(r)]}{dr^2} = \frac{-qN_d}{\varepsilon} \qquad (1.2.2)$$

where $\varepsilon = \varepsilon_0\varepsilon_r$ is the absolute dielectric constant of the material and $\phi(r)$ is the electric potential as a function of r.

The potential $\phi(r)$ and the electric field E are zero in $r \leq R_0$ and the potential difference between the grain surface and bulk is called *built-in potential* (i.e., a potential generated by the internal spherical charge unbalance).

The Boundary conditions to obtain a unique solution of polar Poisson equation are:

$$1)\ \frac{d\phi}{dr}|_{r=R_0} = 0 \quad and \quad 2)\ \phi|_{r=R_0} = 0; \qquad (1.2.3)$$

Equation (1.2.2) relation must be integrated once to obtain the functional form of the electric field E as function of r:

$$\frac{d[r\phi(r)]}{dr} = \frac{-qN_d}{2\varepsilon}r^2 + A \qquad (1.2.4)$$

The potential as function of r is obtained integrating twice the (1.2.2):

$$\phi(r) = \frac{-qN_d}{6\varepsilon}r^2 + A + \frac{B}{r} \qquad (1.2.5)$$

where A and B are two integration constants to be defined by exploiting the boundary conditions (1.2.3).

The final and unique solution of the 3D spherical Poisson equation for the potential is:

$$\phi(r) = \frac{-qN_d}{6\varepsilon}r^2 + \frac{qN_dR_0^2}{2\varepsilon} - \frac{qN_dR_0^3}{3\varepsilon r} \qquad (1.2.6)$$

The (1.2.6) includes three terms: a parabolic, a constant and a hyperbolic one.

- the parabolic term has the same functional form as in the planar case.
- the constant term has no physical meaning.
- the hyperbolic term represents the only difference between the spherical model and the planar one.

Revised charge neutrality condition for 3D-spherical geometry, assuming the negligibility of the negative surface layer width, is:

$$N_d V_{dep} = N_s A_{sur} \qquad (1.2.7)$$

where N_d and N_s are the depletion donor atoms density and the surface state one, V_{dep} is the depletion region volume and, A_{sur} is the grain surface.
Inserting the depletion region volume and grain surface area expressions in (1.2.7), it becomes:

$$qN_d\left(\frac{4}{3}\pi R^3 - \frac{4}{3}\pi R_0^3\right) = qN_s(4\pi R^2) \qquad (1.2.8)$$

and the surface potential V_s is:

$$\phi(r)|_{r=R} = \phi(R) = -V_s \qquad (1.2.9)$$

In conclusion, N_s and V_s are defined from (1.2.6) and (1.2.7), exploiting (1.2.1) ,in 3D spherical coordinates:

$$V_s = -\phi(R) = \frac{qN_d}{2\varepsilon}\Lambda^2\left(1 - \frac{2\Lambda}{3R}\right) \qquad (1.2.10)$$

$$N_s = \Lambda N_d\left(1 - \frac{\Lambda}{R} + \frac{\Lambda^2}{3R^2}\right) \qquad (1.2.11)$$

The main conclusions that can be stated observing (1.2.10) and (1.2.11) relations to understand in-depth some not trivial system dynamics are:

- if $\Lambda << R$ (the grain is strongly larger than bulk), the results are comparable with the planar model ones;
- if $\Lambda \rightarrow R$ (very small bulk) V_s and N_s estimates are 1/3 with respect to the planar case ones. It means that in 3D-spherical case, the depletion region positive charge is neutralized by 1/3 of the N_s negative charge, necessary for the depletion charge neutralization in the planar case.

Thus, assuming $\Lambda \equiv R$, the smaller is the grain size Λ, the smaller is N_s, the smaller is V_s, the greater is the grain flowing current [4].

1.3 Failure of the Depletion Approximation (DA)

The flattening of the band bending consists in the conduction band upward flattening inside the grains (Fig. 1.3.1). The difference $\Delta E_c = E^c_{max} - E^c_{min}$ decreases, where E^c_{max} and E^c_{min} are the conduction band maximum and the minimum energies.
If the grain is big enough to allow the bulk presence, E^c_{min} is the bulk conduction band energy; if the gain size decreases enough, leading to the bulk disappearing, the flattening of band bending occurs and E^c_{min} will increases; this effect occurs because the grain is not large enough to allow the complete potential extinction (Fig 1.3.1) [4].

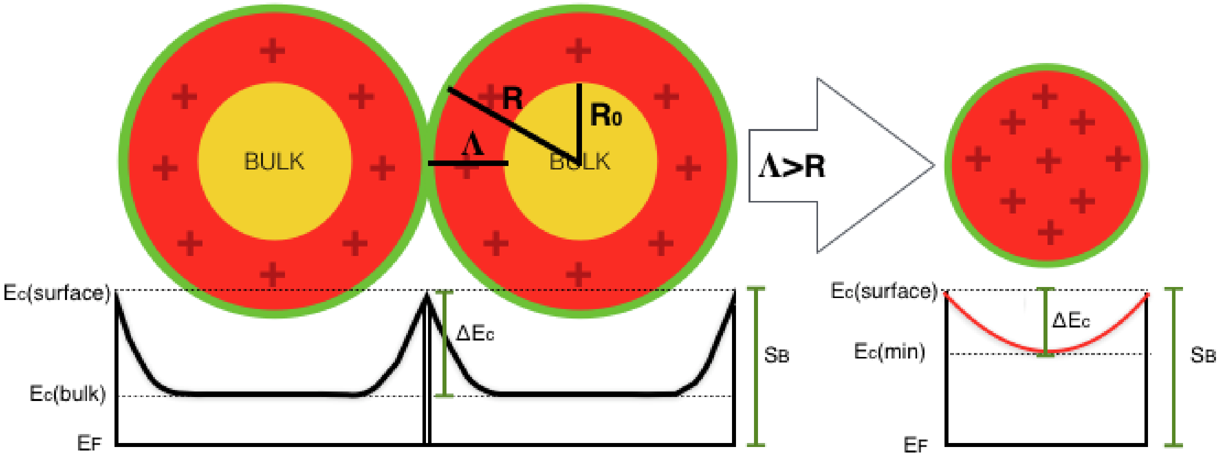

Figure 1.3.1: changing of ΔE_c due to the flattening of the band bending effect. The grains on the left are with bulk $(\Lambda < R)$ and the grain on the right is without bulk $(\Lambda > R)$.

Thus, if grains are in the flattening of band bending condition:

$$\Delta E_c = E_c^{surf} - E_c^{cent} \ll qV_s. \quad (1.3.1)$$

where E_c^{surf} and E_c^{cent} are the conduction band energy on the grain surface and center respectively.
In the limit $\Lambda \equiv R$ and $\Lambda \rightarrow 0$, the depletion approximation is no longer valid and the real charge density has to be taken into account and it is:

$$\rho = -qN_d + qN_d e^{\frac{q\phi}{K_b T}} \quad (1.3.2)$$

where the conduction band state density has been used.
Thus, the (1.2.2) become:

$$\frac{1}{r}\frac{d^2[r\phi(r)]}{dr^2}=\frac{\rho}{\varepsilon}=-\frac{qN_d}{\varepsilon}+\frac{qN_d}{\varepsilon}e^{\frac{q\phi}{K_bT}} \quad (1.3.3)$$

To solve uniquely the differential equation (1.3.3), three boundary conditions are required:

$$\phi(r)|_{r=R}=\phi(R)=-V_s \quad (1.3.4a)$$

$$-\frac{d\phi}{dr}|_{r=0}=0 \quad (1.3.4b)$$

The (1.3.4a) states that the surface potential is equal to V_s, the (1.3.4b) states that, the tangent to conduction band in the grain center is parallel to the x axes (Fig. 1.3.1). Furthermore, (1.3.5), imposing the grain charge neutrality, plays the role of the third boundary condition.

$$\int_V \rho\, d^3r=\int_l \left(\frac{qN_d}{\varepsilon}-\frac{qN_d e^{\frac{q\phi}{K_bT}}}{\varepsilon}\right)4\pi r^2 dr=\int_{surf}\frac{q}{\varepsilon}N_s d^2r=\frac{q}{\varepsilon}N_s 4\pi R^2 \quad (1.3.5)$$

and so:

$$-\frac{d\phi}{dr}|_{r=R}=\frac{q}{\varepsilon}N_s \quad (1.3.6)$$

This model puts in light that the unknown potential $\phi(r)$ is function of six parameters:

- T that is usually known;
- N_d and ε, that are measurable properties of the material;
- N_s and R;
- V_s that, after the setting of N_d, N_s, R, is influenced by from the grains surrounding atmosphere.

V_s behavior could be studied through an experimental procedure, called Arrhenius Plot , by measuring the material conductance. This procedure is made concurrently with a slow temperature variation, and, knowing the type of semiconducting material and the surrounding atmosphere composition, the potential $\phi(r)$ and the density of surface states N_s, as grain radius function, can be determined.

Until now, only the dynamics between semiconductor grains has been taken into account. The next paragraph will connect the widely described grains physics with the concept of metal-oxide nanostructured sensor, studying its conductivity, response and the sensing dynamics [4].

1.4 From Grains to Sensors and Responses

In the previous paragraphs, the physic foundations about semiconductor nanograins and the consequences of their bulk size decreasing have been introduced and detailed; in fact the sensors employed in this thesis study are based on this particular nanotechnology in form of thick film porous sensing materials [9]. A sensor is obtained by printing a viscous paste, made by a mixture of metal-oxide (MOX) semiconductor nano powder and some chemical additives, on a suitable insulating and stiff substrate, putting in contact two gold electrodes (the nano powder synthesis and sensor assembly will be further detailed throughout the next chapter; figure 1.4.1). The substrate is even equipped with a heater able to optimize the sensor qualities, heating it at the proper working temperature [10].

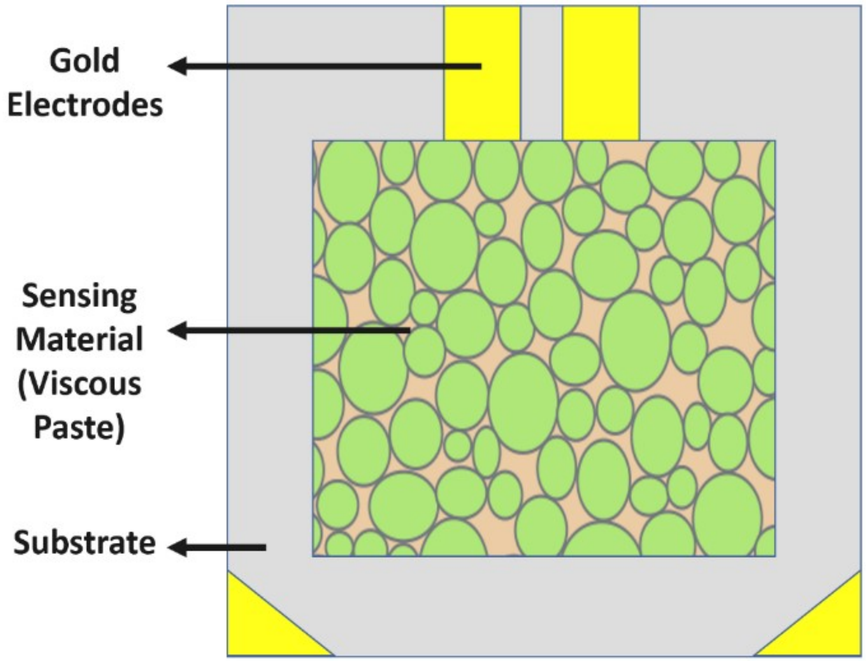

Figure 1.4.1: draft of a MOX nanostructured sensor. Green circles represent the nanograins contained in the sensing material; Top and bottom yellow shapes represent the sensing film gold electrodes and the heater ones respectively; grey enclosing shape represents the substrate.

Looking back to the physics of the system, conduction band electrons must exhibit enough energy to overcome the grain-grain potential barrier to generate current inside the sensing material. Across the next steps, thick-film MOX sensors sensing mechanism and their working principle will be explained in details. MOX sensors are based on chemoresistivity, i.e. the property of varying resistance/conductance as a function of the chemical reactions with the surrounding gaseous compounds, happening on the material surface. The reversible chemical adsorption of the ionized gas molecules on the surface of the grains affects the height of the grain-grain potential barriers and, accordingly, the macroscopic thick-film resistance. Various environmental molecules and ions, such as O^-, O_2^-, O^{2-}, can be adsorbed on the grain surfaces until their complete coverage. The adsorption rate depends on different variables such as sensor temperature, atmospheric composition, type of material and so on.

Considering that MOX sensors working temperatures range between 300 and 500°C, O_2^- and O^- are the most abundant ions at low temperatures (below 300-350°C) and high temperatures respectively (above 350°C), because the high temperature favors the complete dissociation of molecular oxygen.

The adsorbed oxygen ions generate some acceptor surface states (on the grain surface), attracting and capturing the bulk conduction band electrons, so emphasizing the double layer effect; for a n-type semiconductor (i.e. SnO_2, WO_3, ZnO), this configuration leads to an appreciable resistivity increase and a current-flow reduction. After enough time, the sensor surface coverage reaches the equilibrium state, where the coverage ratio (and accordingly also the sensor resistivity) remains constant in time, so providing the background response in air (R_{air}), properly called "baseline" (i.e., it is the reference response against which the sensor signal is then normalized).

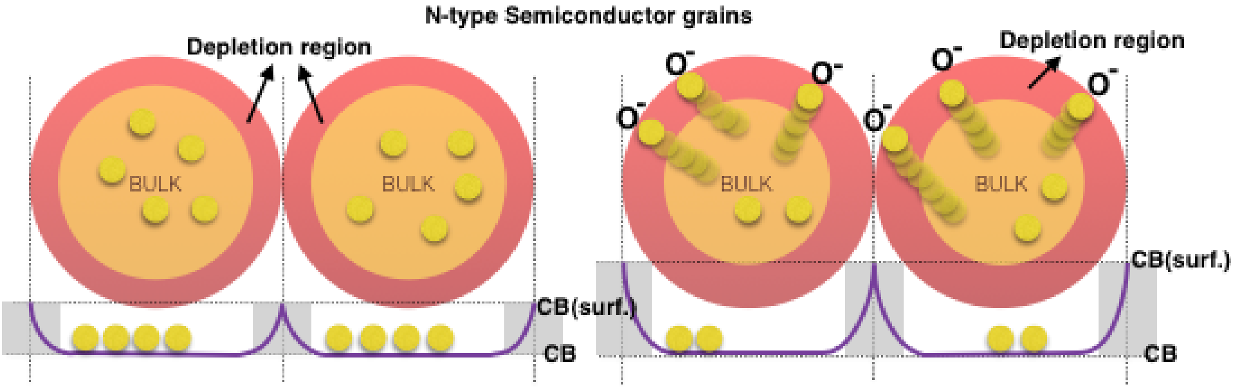

Figure 1.4.2: grain-grain potential barrier and surface oxygen adsorption. Yellow and orange circles, are conduction electrons and bulk region respectively, instead the red ring is the grain depletion region. Violet lines represent the grain-grain potential barriers.

When a sensor is exposed to a gaseous environment, the grain surface oxygen coverage undergoes to relevant modifications, due to the interaction with the gas ions and molecules surrounding it. For instance, considering the interaction with a reducing gas like CO, CO is highly oxidized by surface oxygen ions, freeing CO_2 molecule in the atmosphere and leaving empty a surface state; according with this mechanism, the grain surface coverage ratio decreases, allowing the release of the electrons, previously captured by adsorbed oxygen ions, in conduction band and the consequent current increase. The same analysis can be done for oxidizing gases (such as NO_2, O_3), that, instead, are reduced by the interaction with the semiconductor grain surface, leading to an oxygen coverage ratio and sensing film resistance increasing [11].

The choice to use thick-film sensors in this application is based on the high number of advantages that this devices exhibit with respect to the other available technologies. The main advantage is the wider gas diffusion within the sensing material layer (figure 1.4.3a), leading to a significative sensitivity and detection limit improving (up to tens of ppb).

On the other hand, the main downside of this approach is the complication in conduction mechanism, underlined by a not clear electronic path for the current flow inside the sensing material (red broken lines in figure 1.4.3a) that could abruptly change during the sensor usage period.

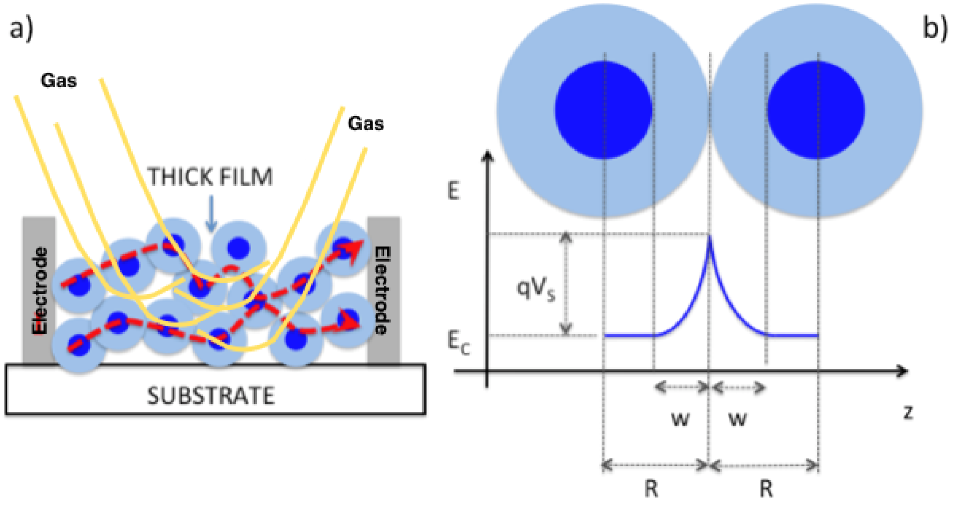

Figure 1.4.3: (a) thick film sensor working principle; (b) grain-grain double potential barrier (blue line).

The synthesis of metal-oxide nano-powder is crucial to maximize the reproducibility of the sensor performances: to prepare sensors sharing the same behavior, their sensing film must be composed by nanograins of about the same size. If this condition is not satisfied, the sensor reproducibility is easily compromised and measures on the same sample can provide results dramatically different. It is worth noting that this sensors, characterized by the sensing mechanism explained above, shows an high sensitivity to a wide range of chemicals, but at the same time, they exhibits poor selectivity in detecting single gases inside a mixture [12]. Different attempt were made to solve this problem and the main ones are:

- concurrent use of sensors in array;
- realization of mixtures of diverse metal oxides (e. g., mixing SnO_2 and TiO_2 the ST sensors were obtained)
- addition of a small percentage of other elements to the metal-oxide mixture, such as noble metals (e.g., palladium, gold, silver, platinum, copper, etc.).

In chapter 2 the sensor production process and assembly will be dealt with in detail, highlighting the occurring troubles and possible solutions to produce reproducible and reliable MOX sensors.

1.5 Sensor conductivity and response

The conduction band electron density $n(x)$, computed with in details in A.1, is:

$$n(x) = N_c e^{\frac{E_F - E_C}{K_b T}} = N_d e^{\frac{q\phi(x)}{K_b T}} \quad (1.5.1)$$

where N_c and N_d are the effective state density in conduction band and the donor density in the depletion region, E_F is the Fermi level, E_C is the conduction band energy, q is the electron charge, $\phi(x)$ is the potential as a function of x, k_b is the Boltzmann constant and T the temperature in Kelvin.

Let's introduce the quantity n_{surf}, representing the amount of conduction band electrons having energy enough to reach the grain surface and cross the surface potential barrier V_s, as:

$$n_{surf} = N_d e^{\frac{-qV_s}{K_b T}} \quad (1.5.2)$$

If the system is not subjected to an external bias, E_F is flat and no current flows, on the contrary, the current could flow if the system is placed in an external bias, where the Fermi level becomes a Quasi-Fermi level, and an electric field raises (1.5.3).

$$E = \frac{1}{q}\frac{\partial E_{Fn}}{\partial x} \quad (1.5.3)$$

where E_{Fn} is the quasi-Fermi level energy.
Since the current density and the conductivity are:

$$\boldsymbol{J}_n = n\mu_n \frac{\partial E_{Fn}}{\partial x} = n_{surf}\mu_n q\boldsymbol{E} = N_d e^{\frac{-qV_s}{K_b T}} \mu_n q\boldsymbol{E} = \sigma\boldsymbol{E} \quad (1.5.4\mathrm{a})$$

$$\sigma = N_d e^{\frac{-qV_s}{K_b T}} \mu_n q \quad (1.5.4b)$$

where: n is the conduction band electron density, μ_n is the electron mobility and σ the resulting conductivity of the material.

Whether the conductivity is multiplied for the junction geometry (length and size of the contacts), the conductance G results as shown by (1.5.5):

$$G = G_0 e^{\frac{-qV_s}{K_b T}} \quad (1.5.5)$$

The conductance G (1.5.5) depends on the temperature and the potential barrier: the higher is the absolute temperature, the larger is the conductance and, the smaller is V_s, the higher is the flowing current.

The sensor Response $R(t)$ is an dimensionless quantity, represented by the variation of G in percentage and, it is expressed as:

$$R(t) = \frac{G_{gas} - G_{air}}{G_{air}} = \frac{G_{gas}}{G_{air}} - 1 \propto e^{\frac{-q(V_{gas} - V_{air})}{K_b T}} \quad (1.5.6)$$

where G_{gas} and G_{air} are the sensor conductance in gas and in air respectively. Qualitatively, the sensor response (figure 1.5.1) is proportional to the exponential of the difference between the surface potential barrier in gas presence and in air.

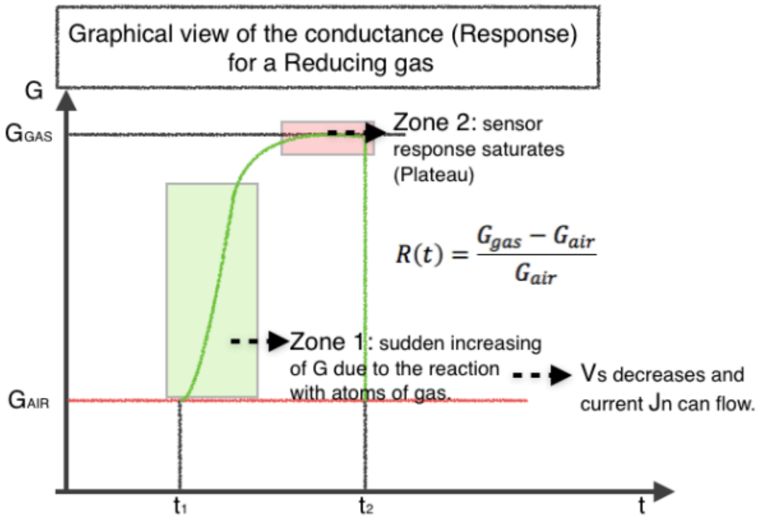

Figure 1.5.1: Typical sensor response $R(t)$. G_{air} and G_{gas} are the sensor conductance in dry air (red straight line) and in gas presence (black straight line) respectively; the green curve is the sensor signal, consisting in the conductance variation as a function of time t.

The choice to compute $R(t)$ through (1.5.6), is justified by the need to deal with dimensionless objects, not depending on G_{air} and the physical quantity measured [13].

1.6 Thick Film Sensors Working Principle

MOX sensors are devices very used nowadays thanks to their versatility and so their suitability in many application fields like environmental, agri-food, healthcare, automotive and so on. As told in the previous chapter, the sensor heating is a fundamental operation required to ionize the surrounding chemical compounds, so optimizing the sensor detecting performances. When a MOX sensor is placed in air, the surrounding oxygen ions or/and molecules are adsorbed on the surface of each inner and outer grain composing the porous sensing layer, acting as acceptor surface states. The adsorbed oxygen ,thanks to its electronegativity, steals electrons from the grain conduction band, trapping them at the surface and so reducing the grain conductivity. This reversible chemical phenomenon, called “ionosorption”, is the principal effect of the MOX sensing mechanism. When the surface reactions achieve the equilibrium state (adsorbate layer and coverage ratio do not change), the film conductivity remains constant, providing a ground sensor signal called “baseline”. The aforesaid oxygen adsorption forces the enlarging of the grain “depleted shell”, accentuating the band bending and, as a consequence, the sensor resistance. The two main reactions involved in ionosorption process on the grain surface are:

$$O_2(gas) + e^- \leftrightarrow O_2^-(ads) \quad (1.6.1)$$

$$O_2^-(ads) + e^- \leftrightarrow O_2^{2-}(ads) \leftrightarrow 2O^-(ads) \quad (1.6.2)$$

Focusing on the case of a n-type semiconductor, characterized by grains large enough to contain a well-defined bulk region, the electrons able to take part to the electric current must have an energy at least equal to qV_s (the minimum energy required to reach the grain surface and to overcome the potential barrier). The number of electrons reaching the surface is given by (1.5.2). For instance, introducing a reducing gas, like CO, in the gaseous environment surrounding a sensor, it approaches the sensing porous film surface and reacts with the adsorbed oxygen ions and molecules. CO combines itself with the surface adsorbed oxygen freeing CO_2 molecules in the environment and leaving free surface states (figure 1.6.1). The electrons, previously captured by surface-adsorbed oxygen, are released in conduction band, leading an increase in sensor conductivity and a decrease in band bending effect [4].

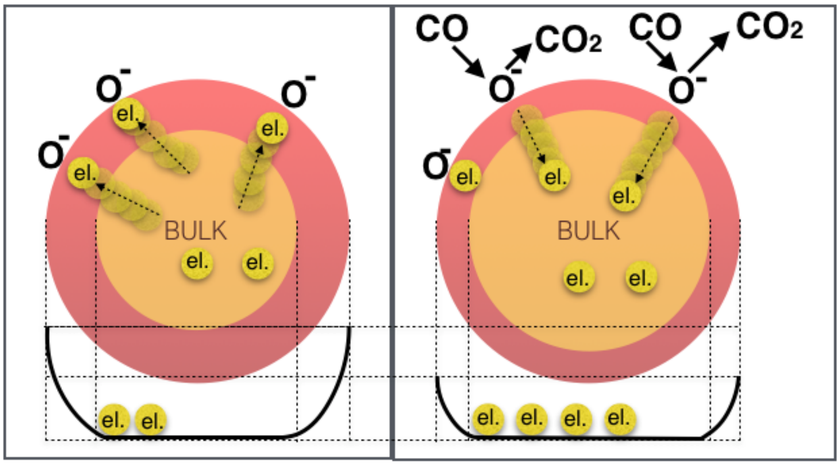

Figure 1.6.1: Electron entrapping due to adsorbed oxygen ions (left square) and CO_2 and electron release due to oxygen – reducing gas (CO) interactions (right square).

1.7 In-Out Diffusion

At this point, it should be understood that the sensing mechanism of chemoresistive sensors is based on the inter-grain potential variation due to the oxygen adsorption on the grain surface. This reflects a macroscopical sensor conductance variation as explained in details in the previous paragraphs. The idea is to write out the relation between the oxygen partial pressure of the surrounding atmosphere and the inter-grain surface barrier. It is generally accepted that oxygen adsorption at the grain surface directly implies a parabolic band bending, due to a constant donor density throughout the depletion region. However, the distribution of the oxygen vacancies, behaving as donor impurities, is far from constant, so implying a sort of dependence between the amount of adsorbed oxygen (surface coverage ratio) and the ambient oxygen partial pressure. At a certain temperature (from 350K up to 500K) some effects involving oxygen ions occur among sensor bulk, sensor surface and the external environment. The lattice oxygen ions can migrate outside the semiconductor grain, coming back ionized in the atmosphere. The following relation expresses the reversible reaction afore explained:

$$V^{++} + 2\mathrm{e}^{-} + O_{\mathrm{int}} \Leftrightarrow O_{latt} \quad (1.7.1)$$

Where: V^{++} is a doubly ionized oxygen vacancy (i.e. a twice positive vacancy), O_{int} is an interstitial oxygen (i.e., an oxygen ion dispersed, but not bound to the lattice) and O_{latt} is a lattice's oxygen (i.e., an oxygen ion bound to the lattice). It is possible to rewrite the previous formula as:

$$O_0 \Leftrightarrow V^{++} + 2\mathrm{e}^{-} + \frac{1}{2}O_2 \quad (1.7.2)$$

where O_0 is the lattice oxygen and the last term has been rewritten as $\frac{1}{2}O_2$, considering the atmosphere molecular oxygen.

Applying the Dalton mass action law at the thermodynamic equilibrium, the constant K is obtained as:

$$K = [V^{++}] \cdot n^2 \cdot p(O_2)^{1/2} \quad (1.7.3)$$

where, $[V^{++}]$ is the doubly ionized oxygen vacancy concentration, n^2 is the electron density in conduction band and $p(O_2)^{1/2}$ is the oxygen partial pressure, strictly proportional to its concentration. K is related to the energy involved in the reaction (1.7.2), that can be split into two sub-relations:

$$O_0 + S \Leftrightarrow V + O_s^0 \quad (1.7.4)$$

where S is a surface site, V is an oxygen vacancy and O_s^0 is an oxygen ion, occupying a surface site S. The (1.7.4) expresses the situation in which an oxygen atom is taken out from a lattice site inside the crystal, and carried to the grain surface (Figure 1.7.1).

$$O_s^0 \Leftrightarrow \frac{1}{2}O_2 + S \quad (1.7.5)$$

The (1.7.5) takes into account the case in which the oxygen ion lying in a surface site O_s^0, is desorbed in air as $\frac{1}{2}O_2$, freeing a surface site S (Figure 1.7.1).

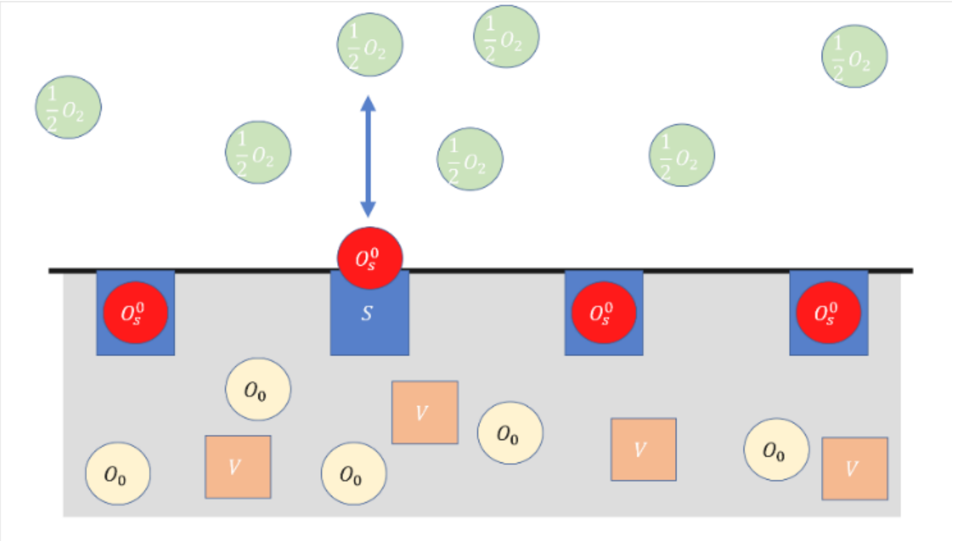

Figure 1.7.1: Sketch view of a crystal-environment interface. Green, red and yellow disks represent the environmental free oxygen molecules, oxygen ions lying in crystal surface sites and lattice's oxygen respectively. Instead the blue and orange squares represent surface sites and oxygen vacancies.

Applying the mass action law to (1.7.4) and (1.7.5), the following two relations are obtained:

$$\frac{[V]\cdot[O_s^0]}{[S]} \propto \mathrm{e}^{(-E_{sur}/KT)} \quad (1.7.6)$$

$$\frac{p(O_2)^{1/2}\cdot[S]}{[O_s^0]} \propto \mathrm{e}^{(-E_{ads}/KT)} \quad (1.7.7)$$

Where $[V]$ is the vacancy concentration, $[O_s^0]$ is the concentration of the surface sites occupied by an oxygen ion, $[S]$ is the surface state concentration, $p(O_2)^{1/2}$ is the oxygen partial pressure, E_{sur} and E_{ads} are the energies required to carry an oxygen ion from the lattice to the surface and from the surface to vapor phase respectively. Multiplying (1.7.6) and (1.7.7) and, explicating $[V]$, the vacancies concentration results to be:

$$[V] \propto p(O_2)^{-1/2}\mathrm{e}^{-(E_{sur}+E_{ads})/KT} \quad (1.7.8)$$

$$[V] \propto p(O_2)^{-1/2} e^{-(E_{for})/KT} \quad (1.7.9)$$

where $E_{for} = E_{sur} + E_{ads}$ is the total energy required to form an oxygen vacancy [14].

It is now useful to introduce the concept of enthalpy (H). H expresses how much internal energy the thermodynamic system is able to exchange with the external environment and it is calculated as the sum of the internal energy U and, the product of system pressure and volume:

$$H = U + PV \quad (1.7.10)$$

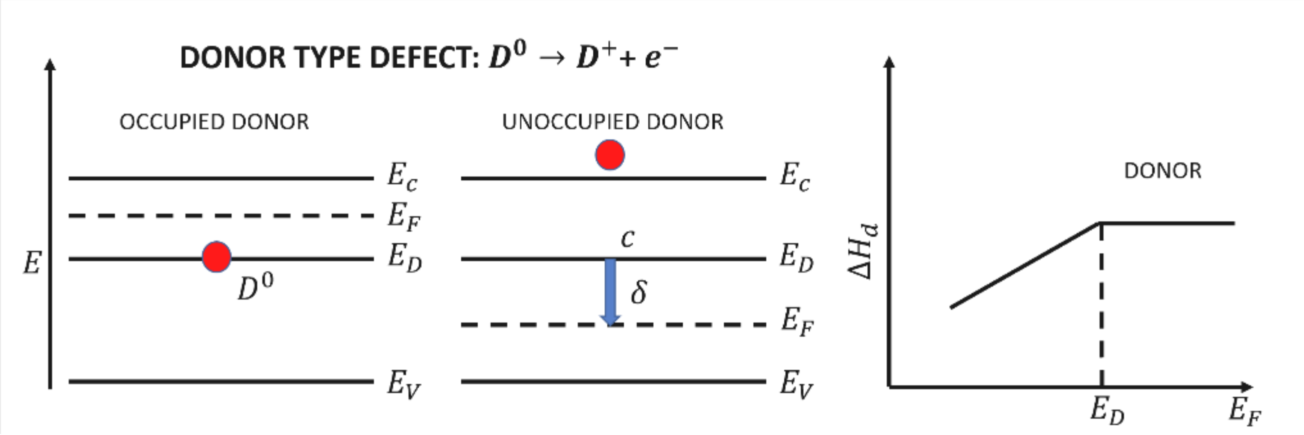

Figure 1.7.2: Energy band diagram of a crystal. In the left diagram, where the bulk condition is satisfied ($E_D < E_F < E_C$), the donor state is occupied; in the central one, where the surface condition is satisfied ($E_F < E_D$), the donor state is unoccupied and the energy δ is ceded back to the system.

Physically, if E_F is located between the donor energy level E_D and the conduction band energy (E_C), as it is in the bulk region, H relative to the oxygen vacancy formation is constant. In this case, the donor is occupied (resulting electrically neutral) and the enthalpy variation ΔH_d is independent from E_F; while, if E_F is between E_D and the valence band energy (E_V), ΔH_d relative to the oxygen vacancy formation decreases (it is easier to have vacancies; figure1.7.2, right). Therefore, in this last case, neutral donors become positively charged unoccupied donors and the electrons released are included in a electron reserve (E_F), leading to an energy gain δ.

A doubly ionized oxygen vacancy $[V^{++}]$ occur when a occupied donor releases two electrons to the Fermi level, carrying a system energy gain. The positive energy received from the system is:

$$E_{d_1} - E_F + E_{d_2} - E_F \quad (1.7.11)$$

where E_{d_1} and E_{d_2} are the energies of the donor levels.
The total energy required to have a vacancy formation is :

$$E_0 = E_{for} + 2E_c - E_{d_1} - E_{d_2} \quad (1.7.12)$$

and combining (1.7.12) with (1.7.9) the final relation for $[V^{++}]$ is:

$$[V^{++}] \propto p(O_2)^{-1/2} \mathrm{e}^{-[E_0-2(E_C-E_F)]/KT} \quad (1.7.13)$$

The last relation shows the oxygen vacancy density increasing while E_F goes down and down in band gap, fixing the O_2 partial pressure (Figure 1.7.3). The final result states the impossibility to have a uniform doping level along the whole space charge region, underlying in DA.

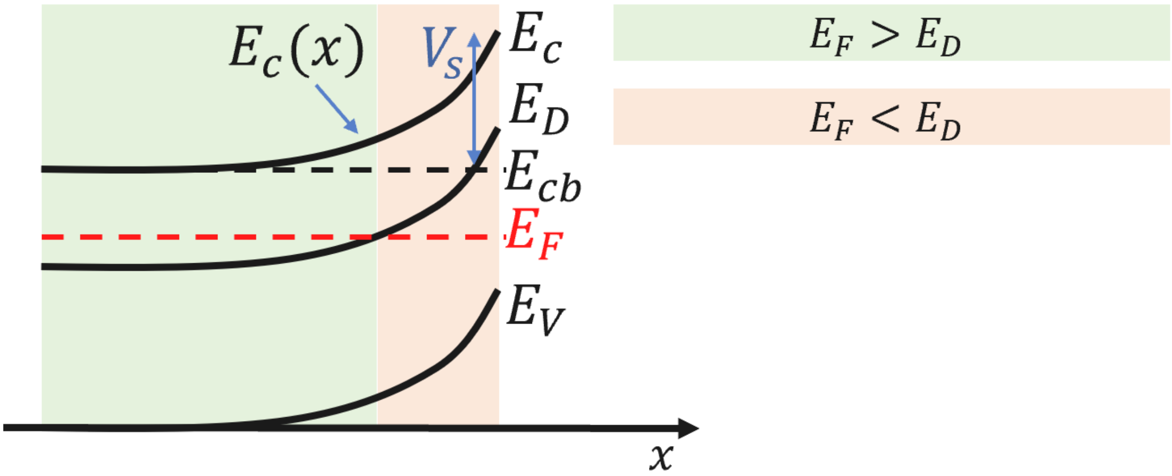

Figure 1.7.3: Energy band diagram of a crystal. Green and orange area are the bulk and the surface regions respectively.

N_d, the bulk donor density, is proportional to the oxygen partial pressure as:

$$N_d \propto p(O_2)^{-1/2} \mathrm{e}^{-[E_0-2(E_{cb}-E_F)]/KT} \quad (1.7.14)$$

where E_{cb} is the bulk conduction band energy.
Combining (1.7.13) and (1.7.14) the proportionality between the double ionized vacancies concentration ($[V^{++}]$) and N_d is:

$$[V^{++}] = N_d \mathrm{e}^{2(E_c(x)-E_{cb})/KT} \quad (1.7.15)$$

where $E_c(x)$ and $E_c(x) - E_{cb}$ are the generic conduction band energy and the potential barrier amplitude at the distance x (Figure 1.7.3).

$$[V^{++}] = N_d \mathrm{e}^{2eV(x)/KT} \quad (1.7.16)$$

At this point it is worth to note that the oxygen vacancy concentration at the equilibrium, strongly depends on the band bending effect.

Solving the Poisson equation exploiting (1.7.16) as charge density:

$$\frac{\mathrm{d}^2 V(x)}{\mathrm{d}x^2} = \frac{2\mathrm{e}}{\varepsilon} N_d \mathrm{e}^{\frac{2\mathrm{e}V(x)}{KT}} \quad (1.7.17)$$

the potential in the depletion region as a function of x is:

$$V(x) = \frac{kT}{2\mathrm{e}} ln\left[1 + tan^2\left(\frac{x}{\sqrt{2}L_D}\right)\right] \quad (1.7.18)$$

where $L_D = (\varepsilon kT \,/\, 4\mathrm{e}^2 N_d)^{1/2}$ is the Debye Length (a parameter that represent the potential extinction length).

Figure 1.7.4 represents the plot of the potential $V(x')$ as a function of $x' = \sqrt{\frac{x}{2}} L_D$, and it is noticeable its non-parabolic behavior in this region, highlighting its abruptness in the region close to the surface [14].

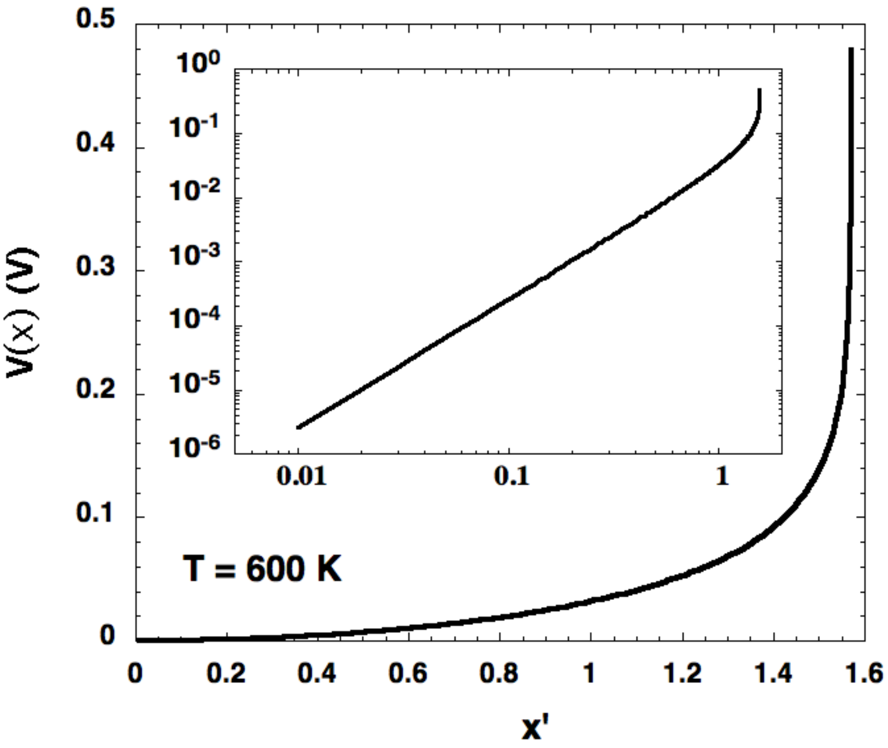

Figure 1.7.4: Plot of the potential in the region very close to the grain surface.

Imposing the charge neutrality condition, for which the negative surface charge must be equal to the positive charge lying in the depletion region, the depletion region width can be computed and it results:

$$x_0 = \sqrt{2}L_D \, arctan\left(\frac{N_s}{2\sqrt{2}N_d L_D}\right) \quad (1.7.19)$$

Where N_s is the density of electrons trapped on the surface.
Combining (1.7.18) and (1.7.19), the surface potential V_s results to be [14]:

$$V_s = \frac{kT}{2\mathrm{e}} ln\left[1 + \frac{N_s^2}{8N_d^2 L_D^2}\right] \quad (1.7.20)$$

2 Metal-oxide (MOX) sensors (Overview)

In this work, nanostructured chemoresistive MOX sensors have been employed to detect colorectal cancer (CRC) VOCs exhaled by different biological samples, such as feces, tumoral tissues, cell cultures and blood samples.

MOX sensors are widely used in diverse research fields, such as biology, agri-food, environmental applications and so on, thanks to their appreciable versatility, durability, reliability and sensitivity. In this chapter, the MOX sensor production and assembly processes will be illustrated in details, all entirely conducted in the clean room and Laboratorio Sensori (LS) of the University of Ferrara.

2.1 MOX gas sensor: a brief description

MOX sensors are powerful sensing devices based on semiconducting metal-oxide nanoparticles, which obey to the semiconductor grain physics (already detailed in the chapter 1). They are capable of detecting with high sensitivity a wide range of chemicals in concentrations up to tenth parts per billion, conserving a very low response and recovery times.

Their working principle consists in the conductance variation of the sensing material, induced by the reversible chemical adsorption of ionized gas particles on the sensor surface.

This kind of sensors are made up of three main components: a substrate, an active (sensing) layer, and a heater.

- The substrate covers two main roles: it is a rigid mechanical support for the sensor and, at the same time, it is an insulating layer (made of sintered alumina Al_2O_3 in our sensors). It hosts on the top the printed interdigitated gold contacts and, the heater on the bottom (a typical sensor is sketched in Figure 2.1.1).
- The sensing layer is made of semiconducting metal-oxide nanoparticles (average size about 50-200 nm), chemically transformed in a viscous paste, then distributed on the substrate between the two interdigitated gold contacts. The paste is spread by means of serigraphic technique with a screen printer machine (here a Aurel 920).
- The heater is a conducting metal coil (here made of platinum), whose temperature is precisely set by controlling its current flowing.

The substrate does not actively participate in the sensing mechanism, but a certain compatibility between the sensing layer and the substrate surface is required in order to avoid mechanical problems like tensions due to thermal expansions and so on.

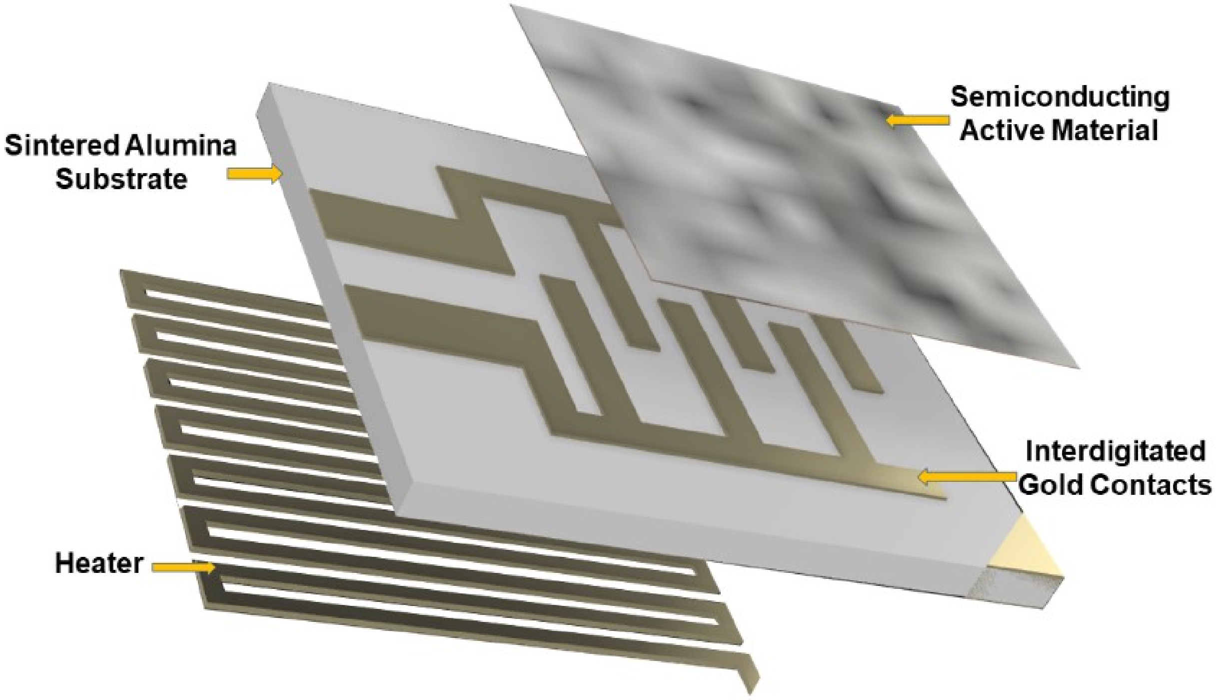

Figure 2.1.1: 3D representation of the components composing a MOX thick film sensor.

The heater is strictly necessary to heat the sensor at its proper working temperature, at which it exhibits the best working features in terms of sensitivity, detection limit, rapidity in response and recovery time.

To set the correct working temperature, it is necessary to know its resistance at room temperature R_{Room} and the corresponding room temperature T_{Room}. This two parameters are carried out by using a multimeter and a very precise environmental thermometer. The zero degree resistance R_0 is calculated inverting the (2.1.1) and imposing $R = R_{Room}$ and $T = T_{Room}$.

$$R = R_0(1 + \alpha T + \beta T^2) \quad (2.1.1)$$

where R and R_0 are the resistances at the temperatures T and $T = 0\ °C$ respectively, α and β are constants depending on material.

Finally, knowing α,β and R_0 and, monitoring the heater resistance through the (2.1.2), it is straightforward to calculate the current heater temperature by using (2.1.1) once again (figure 2.1.2) [15].

$$R(t) = \frac{V(t)}{i(t)} \quad (2.1.2)$$

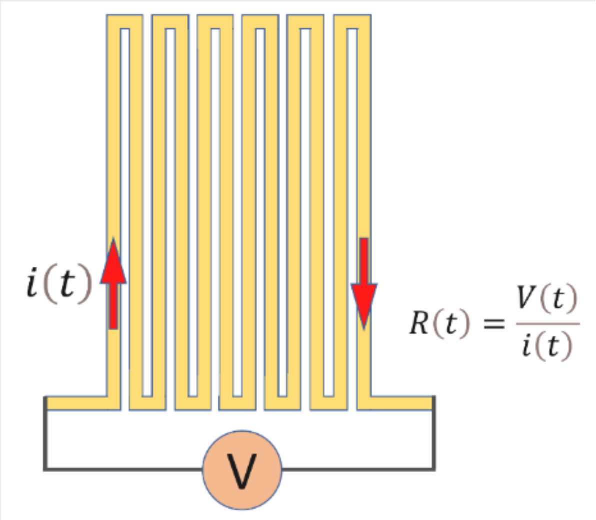

Figure 2.1.2: Sensor heater. A schematic view.

2.2 Production Process

Thick-film sensor production is based on the serigraphic technique, widely used to print graphic art subjects on a certain substrate. In serigraphy, a viscous ink is placed and spread on a flat and slick substrate by means of a stencil and a blade, to print the desired geometry with high precision and appreciable quickness. Thick-film MOX sensors used in this work are prepared exploiting this technique, necessary to spread the sensing material, in form of viscous paste, on the alumina substrate, to put in contact the two interdigitated gold electrodes.

The Sensors obtained through the serigraphic technique have many advantages and the main ones are listed below:

- good sensitivity, also at low gas concentrations;
- low production costs;
- low detection limit (up to tens ppb);
- good repeatability of results;
- low energy consumption;
- good portability (thanks to their small dimensions);
- excellent signal/noise ratio;
- simple using mechanism;
- high versatility;

The production process can be schematized in the following steps (explained one by one in the next paragraphs):

- the semiconducting nanostructured powder is transformed in a viscous paste, adding some chemical vehicles;
- the viscous paste is printed on the sensor substrate through serigraphic technique and, it is dried and fired inside an oven;
- finally, the sensor is assembled and tested to assess its correct functioning;

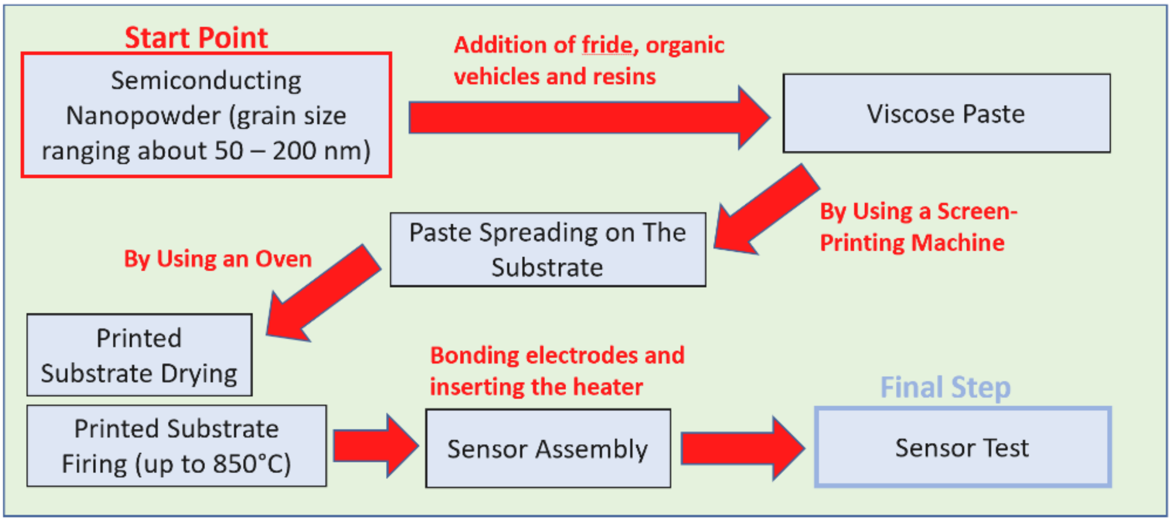

Figure 2.2.1: Scheme of the sensor production, assembly and test.

2.3 Sol-Gel Technique

First of all, the chemoresistive gas sensors require a wide sensing material surface-volume ratio to optimize their performances, maximizing the interaction with the surrounding gas. Hence, the thick sensing layer is composed by metal-oxide nanometric spherical grains, achieved through a chemistry process known as Sol-Gel technique. It is capable of synthetizing interconnected nano-grains, characterized by a radius ranging between 50 and 200 nm, with extreme precision. The achievement of nano-grains with almost the same size is crucial not to fall in the case of depletion approximation failure (Paragraph 1.3), and hence to realize reproducible sensing films. Sol-Gel technique is one of the most used and reliable methods to synthesize a great variety of inorganic networks (mainly ceramic and glassy materials), starting from a certain precursor (like silicon or other metal alkoxides). Thanks to its versatility and easiness in process controlling, it has been chosen to produce metal-oxide nano-powder composing our sensing materials. Furthermore, this approach is a cheap and low-temperature technique suitable to obtain inorganic oxide based materials, allowing a fine control of the product's chemical composition and properties of oxides, such as stiffness, resistance, porosity, electrical and thermal stability [16].

Sol-gel process is briefly explained through the four steps listed below (Figure 2.3.1):

1) hydrolysis of the organic precursor solution (reagents dissolved in water or alcoholic solutions);
2) formation of a colloidal and viscous suspension (sol);
3) transformation of the colloidal suspension in a gel through condensation;
4) removal of the remaining solvent through a thermal treatment (final oxide powder).

Using this technique, it is possible to obtain different gel types starting from the same precursor solution, simply controlling and changing the process parameters during the synthesis process (like reaction temperature, pH of the solution). The result consists in a powder containing a network of pure metal-oxide spherical nanoparticles, suitable to be transformed in a viscose paste for deposition [10]. To print the latter, in the case of this study, a screen-printing machine has been employed and the complete printing process is explained in the next Paragraph.

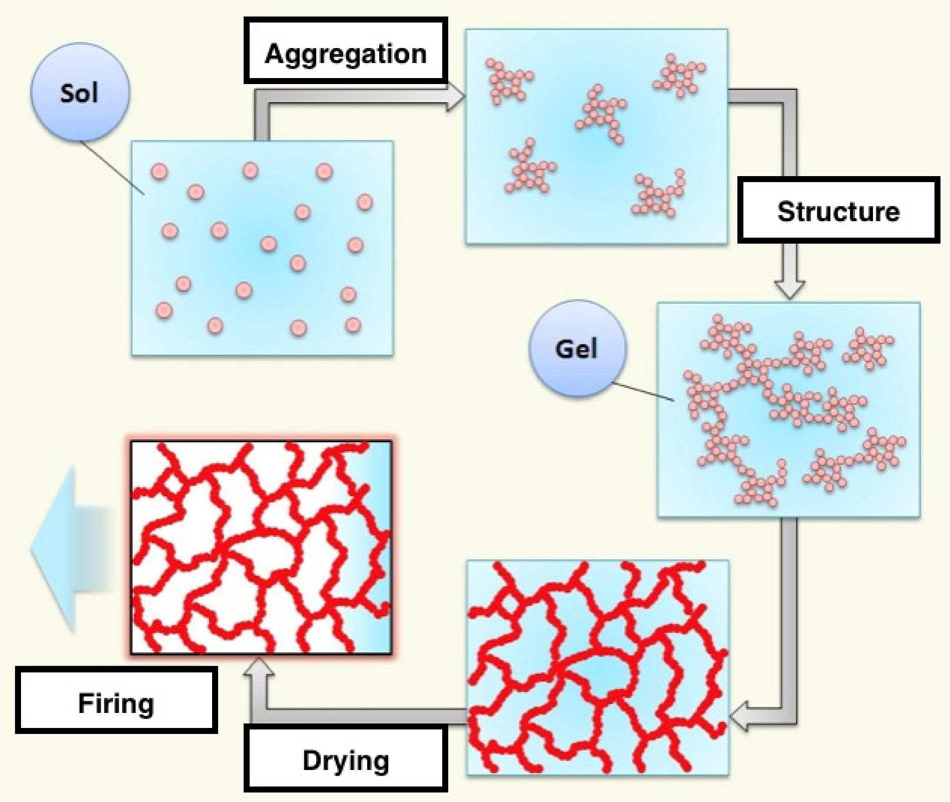

Figure 2.3.1: Illustration of the steps composing the Sol-Gel process.

2.4 Serigraphic Process

The interconnected and homogeneous nano-powder, carried out by exploiting the Sol-Gel technique, is added with some organic vehicles and glass frit, then

transformed in a viscous and porous paste. The latter is spread by means of a screen-printing machine on a substrate where a geometry defining mask was previously applied and fixed. At the end of the procedure, the mask is carefully removed, leaving a precise and clean paste deposition.
The main advantages of serigraphic technique are:

- possibility to obtain prints with very low deposition width (the minimum obtainable film width is of the order of 20 µm);
- many kind of material can be printed;
- miniaturization of devices;
- reliable mass production;
- possibility of realizing a great number of prints at the same time, also based on different materials.

2.5 Sensor Production Process: Substrate Production

The sensor substrate, has the double task of mechanical stiff support and insulator layer between the top placed sensing film, the circuit elements and the bottom placed heater. The substrate of the sensors produced and tested in LS is made of alumina (Al_2O_3), which is characterized by low cost, high thermal and corrosion resistance and good insulating properties. Alumina powder is obtained starting from Bauxite and, in form of paste, it undergoes to pressure treatments, where the pressure choice depends on the desired substrate thickness (in this case of about 1mm). After the shaping, the substrate undergoes thermal treatment (firing) for 12-24 hours. It includes two consequent thermal steps: pre-treatment at 300 – 600 °C to remove organic additives and sintering at 1500-1700 °C, that encourages the adhesion between powder particles, attributing stiffness to the crystalline structure. During firing process, the phenomena of densification and grain growth occur, reducing the material porosity and increasing the grain average size respectively. Moreover, the heater and the interdigitated gold contacts are placed on the bottom and on the top of the sensor substrate, respectively. The substrate does not affect the sensing mechanism, nevertheless its atomic structure must be strictly compatible with the sensing film one, in order to avoid tensions mainly generated by the thermal expansions of the material. A careful substrate surface preparation is required to have an optimal sensing film adhesion [10].

2.6 Sensor Production Process: Metal-Oxide Paste Deposition

Metal-oxide viscous spreadable paste is obtained adding a glass frit small amount and organic vehicles to the metal-oxide nano-powder. In particular:

- glass frit is a powder obtained by a mixture of glassy oxides based on silica (SiO_2) charged with alkaline-earth oxides or with oxides of the IV group, necessary to favor the paste anchoring to the substrate;
- organic vehicles are a mixture of organic solvents, resins and surfactants, that optimize the dispersion of the solid particles inside the medium.

Metal-oxide paste spreading is performed by using a screen-printing machine (Aurel C920). A mask defining a certain geometry is applied upon the substrate before the deposition, avoiding to spread paste in unwanted zones. Moreover, the paste spreading occurs homogeneously upon the substrate by means of a spreading blade (Figure 2.6.1). A second blade moves in the opposite direction with respect the spreading one, reporting the paste excess at the initial position, ready to start a new print [10].

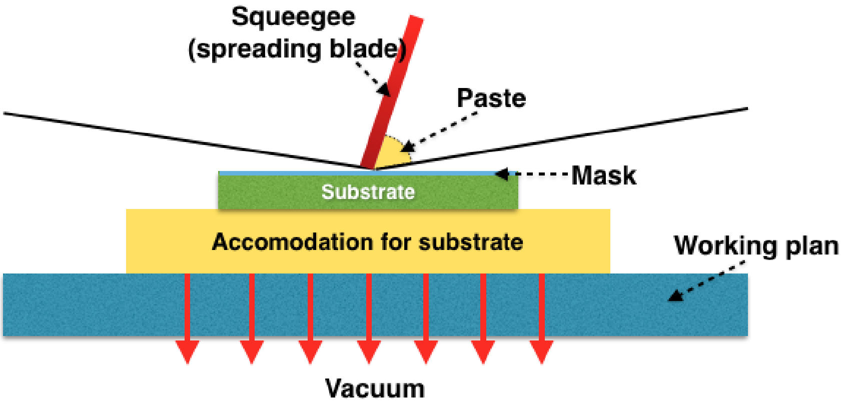

Figure 2.6.1: Sketched screen-printing working principle. Blue and yellow rectangles are the metallic working plan and the socket to fix the substrates, green rectangle represents the masked substrate, ready to be printed with the semiconductor paste, spread by means of the squeegee (red pipe).

2.7 Sensor Production Process: Drying and Firing

After the deposition of the metal-oxide paste upon the sensor substrate, it is subjected to two thermal treatments: Drying and Firing.

- Drying is a low-temperature treatment (around 100-150°C), necessary to remove the residual volatile organic solvents and to avoid the immediate draining of the printed wet paste on the substrate. The drying takes place in a common oven.

- Firing is a high-temperature process, up to 850°C, occurring in an common oven. It aims to the last organic additives removal and leaves the final stiff sensing film tightly anchored on the substrate (only a negligible percentage of glass frit could remain).

The temperature is rigorously controlled to avoid possible work compromising defects and a following sensor malfunctioning [10].

2.8 Sensor Production Process: Assembly and Test

The final steps concerning the sensor production, after the sensing film deposition, drying and firing treatments, are the sensor assembly and test. The sensor assembly process consists in its connection to a four pin TO-39 socket: two pins are welded to the heater contacts and the other two pins to the sensing film ones. The connections are made by using a very thin golden wire (purity at 99.99%, diameter about 0.06mm) and the welding process (properly named sensor bonding) takes place by using a bonding machine that uses the thermo-compression effect to weld metals (Figure 2.8.1). Once the sensor is completely assembled, it is tested in laboratory to assess its correct working, by heating and feeding it at various temperatures and voltages [10].

Figure 2.8.1: Bonding Machine.

3 SCENT B1 device

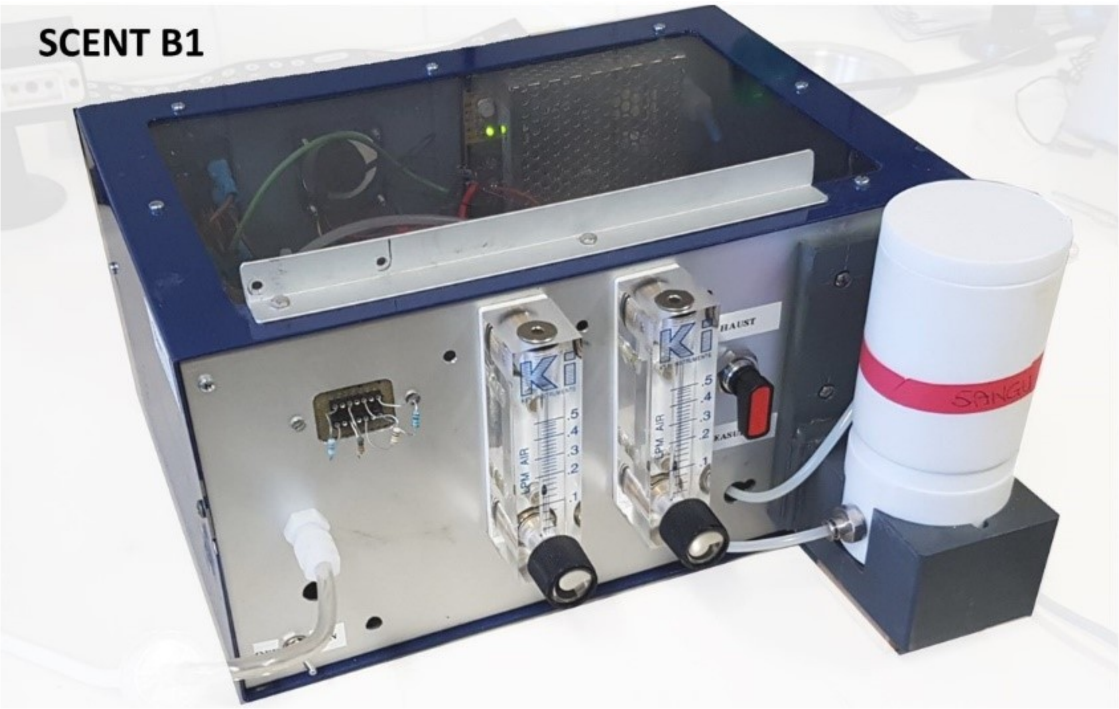

Figure 3.1: SCENT B1 device.

SCENT B1 (figure 3.1) is an enclosed device, hosting an array of four concurrently working nanostructured chemoresistive thick-film sensors, based on different semiconductor materials. It includes two principal independent parts: a pneumatic and an electronic system. Although the feces analysis and some reproducibility tests, included and discussed in Chapter 4, were carried out by means of an other prototype, named SCENT A. Here only SCENT B1 is described, considering the complete affinity between them. SCENT A1 and B1 devices are identical, but the first hosts a sensor more with respect to the second. The electronics, pneumatics and software systems are a full-fledged twins.

3.1 Pneumatic System

The pneumatic system (figure 3.1.1) aspirates air from the external environment by means of a electronic pump and blows it in 4 mm Teflon tubes, through a carbon filter (to stabilize as much as possible the air humidity and temperature) and a 0.2-micron filter (to remove pollutants like particulate matter or aerosols larger than 0.2 micron), keeping constant the air temperature and pressure ($T\sim23^{\circ}C, H\sim20\%$).

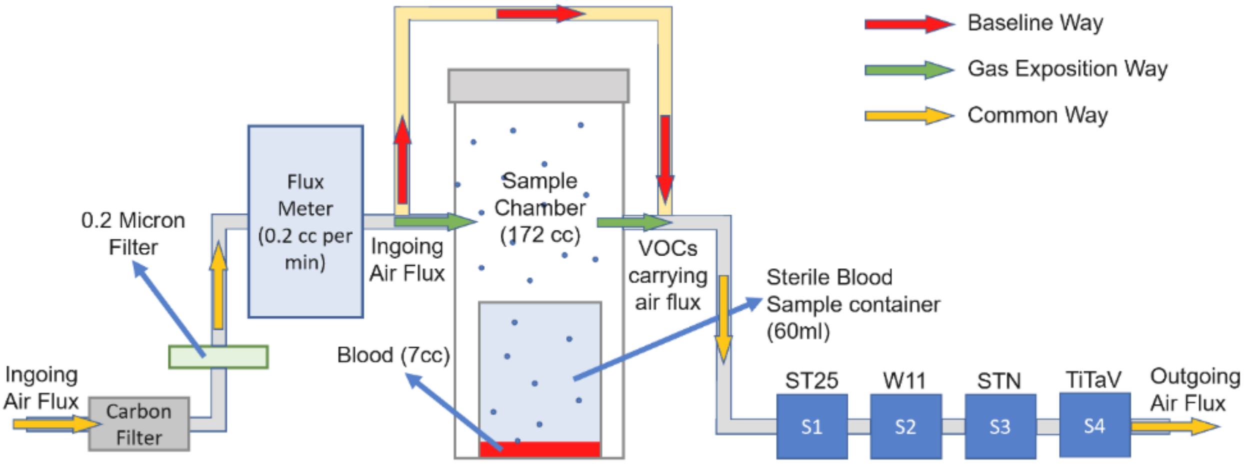

Figure 3.1.1: Block scheme of SCENT B1 Pneumatic system in the case of blood measure.

The resulting clean and dry air flux can be guided directly to the sensors (whose response in this condition is the “baseline”; Baseline Way), or into the sample chamber, where it fetches the sample headspace chemical compounds, before reaching the sensors (Gas Exposition Way) by means of a manual three-way valve. The air flux is regulated through a couple of fluxmeters (one for each flow-way), both set at 0.2 cc per minute.

3.2 Electronic System

The electronic system consists in five printed circuit boards (PCBs). The first PCB contains the SCENT B1 device power supply (mainly air pump and sensor boards supply) and the microcontroller (the CPU unit), suitable to execute calculations on the sampled values and to interface the device with the management software by means of a serial protocol. The other four PCBs, one for each sensor, contain the electronics to manage the sensor heating, film supply and signal acquisition.

The sensor heater, physically described and detailed in paragraph 2.1, is fed by a 8-bit DAC adjustable voltage source, able to provide a power up to 2W. The current flowing inside the heater and the related voltage to which it is subjected are revealed by means of a precision voltage/current sensor.

Furthermore, the electronic system allows to convert the resistance change of each sensor sensing film, when subjected to gas exposition, in a voltage variation by means of an inverting operational amplifier (figure 3.2.1);

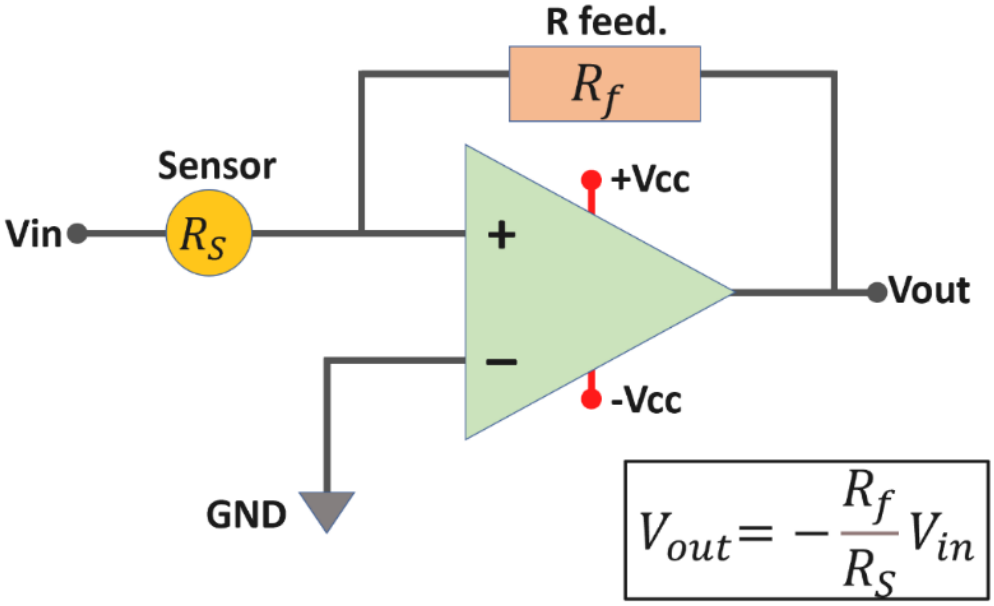

Figure 3.2.1: Inverting operational amplifier. It returns a voltage proportional to the ratio between the feedback and the sensor resistances as shown in the relation above.

The analogic output voltage is converted in a digital signal by using a 12-bit analog to digital converter (ADC) and plotted vs time (figure 3.2.2) through a management software developed ad hoc by SCENT research team. The acquired sensor signals are finally transformed in a response $R(t)$ vs time plot (figure 3.2.3) exploiting the formula (3.2.1).

$$R(t) = \frac{V_{Gas} - V_{Air}}{V_{Air}} \quad (3.2.1)$$

V_{Gas} and V_{Air} are the sensor signals in gas presence and in air (baseline) respectively. $R(t)$ represents a dimensionless result, independent by the measured physical quantity and the baseline amplitude (in general different for each sensor).

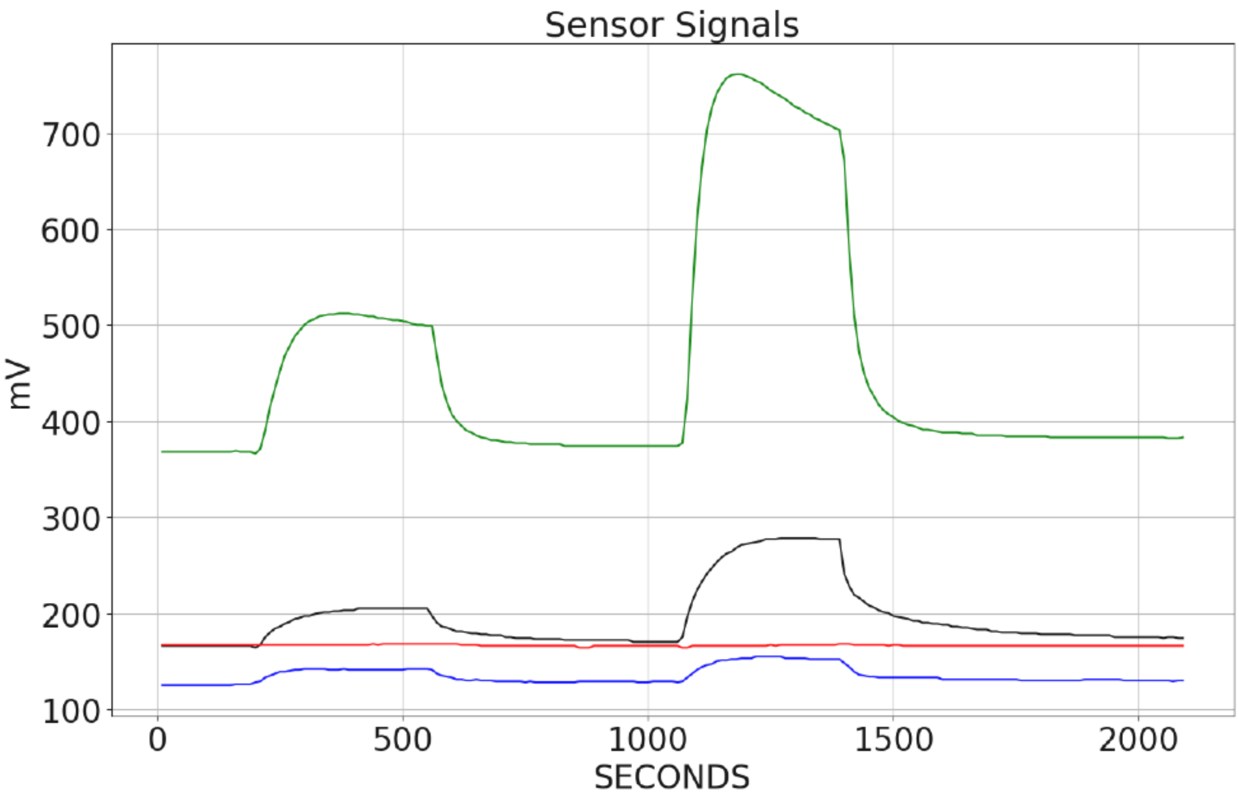

Figure 3.2.2: Acquired concurrently sensor signals (mV).

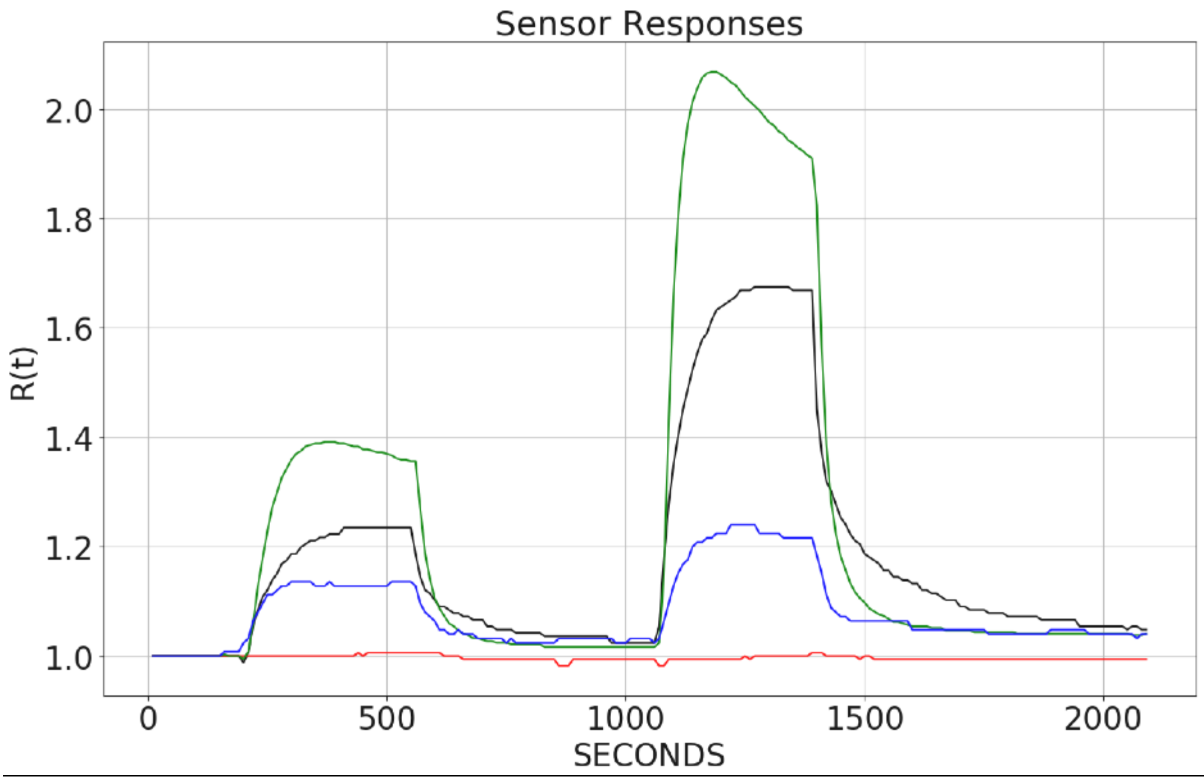

Figure 3.2.3: Sensor responses.

The data acquisition system returns one voltage value per sensor every 10 seconds. They are computed as the average value of the last 2 seconds sampling (about 10Hz). The values returned are plotted together and in real time by the SCENT B1 management software and stored in a .txt file in the connected external computer, to be further analyzed through other advanced data analysis techniques as principal components analysis (PCA) [17], support vector machine (SVM) [18], Receiver Operating Characteristic (ROC) [19], etc.

4 Results and Discussion

The results obtained in this work are not only concerning sensors and their applications, but they belongs to different topics summarized as follows:

1. analysis of biological samples (feces, tumoral tissues, cell cultures and blood) to detect CRC VOCs as tumor markers;
2. sensor repeatability tests and humidity effects in their responses;
3. design and construction of a new device for metal-oxide nanostructured sensors (electronics, enclosure and software).

The first point consists in the use of MOX nanostructured chemoresistive sensors (whose physics has been detailed in chap. 1 and 2) in CRC VOCs detection. The samples investigated with this aim and the related results are:

- **feces,** were investigated by using a patented device SCENT A1 (patent number) containing five MOX sensors working concurrently. This branch of research led to the publication of the article: "***Chemoresistive sensors for colorectal cancer preventive screening through fecal odor: Double-blind approach***", published in Sensors and Actuators Journal, 2019 [13];
- **tumoral tissues,** were investigated by using the patented device SCENT B1 (Italian patent number: 102015000057717) containing four different MOX sensors working in parallel. This work led to the article: "***Colorectal Cancer Study with Nanostructured Sensors: Tumor Marker Screening of Patient Biopsies***", published in Nanomaterials Journal, 2020 [20];
- **cell cultures and blood,** were investigated by using SCENT B1 device, and this branch of research led to the publication of two articles: "***Nanostructured Chemoresistive Sensors for Oncological Screening and Tumor Markers Tracking: Single Sensor Approach Applications on Human Blood and Cell Samples***" [21] and "***Tin, titanium, tantalum, vanadium and niobium oxide based sensors to detect colorectal cancer exhalations in blood samples***" [22], published in Sensors and Molecules Journals, respectively;

In addition, second point of the list, other two works were published:

- **Humidity interference on SnO_2 and $STNO_2$ sensor responses,** where the sensors were calibrated and used to detect CO gas in presence of various degrees of humidity. This study led us to the article: "***Humidity effects on SnO2 and (SnTiNb)O2 sensors response to CO and two -dimensional calibration treatment***", published in Materials Science & Engineering B Journal, 2020 [23];

- **Zinc-Oxide Based Chemoresistive MOX Sensors** were tested and characterized in LS of the Department of Physics and Earth Science (UNIFE), applying them to the detection of the most popular laboratory target gases as CO, NO, CH_4 and butanol to state zinc-oxide sensors reproducibility, fundamental for the medical device serial production. This work led to the publication of the article: "***Reproducibility tests with zinc oxide thick-film sensors***", published in Ceramics Journal, 2019 [24].

As a consequence of the published papers on blood VOCs investigation "***Tin, titanium, tantalum, vanadium and niobium oxide based sensors to detect colorectal cancer exhalations in blood samples"***, a further study has been started at the end of 2020, concerning a follow-up protocol requiring the examination of four blood samples from each oncological patient: the first is collected the same day or, at most, the day before the surgery treatment, the second, the third and the fourth ones after one week, one month and four months from the surgery, respectively. The aim of this study consists in monitoring the patient post-surgery hospitalization, detecting possible relapses and/or troubles during the healing process, through a systematic and periodical blood analysis. Till now, this follow-up protocol has been applied to twenty consentient patients and the first future target is to duplicate the acquired data in the next two/three months.

The third list point concerns the design, construction and assembly of a low-noise sensor device, improving the electronics, the pneumatics and the software, necessary to manage it and for data acquisition, storage and elaboration. It originates from the need to optimize the sensor signal quality, increasing the signal-to-noise ratio and refining the acquisition system. The details about this project are introduced and explained in section 4.2.

4.1 Feces Application

Sensors & Actuators: B. Chemical 301 (2019) 127062

Contents lists available at ScienceDirect

Sensors and Actuators B: Chemical

journal homepage: www.elsevier.com/locate/snb

Chemoresistive sensors for colorectal cancer preventive screening through fecal odor: Double-blind approach[★]

G. Zonta[a,c,*], G. Anania[a], M. Astolfi[a,c], C. Feo[e], A. Gaiardo[a,c,f], S. Gherardi[c], A. Giberti[d], V. Guidi[a], N. Landini[a,c], C. Palmonari[a,b], A. de Togni[b], C. Malagù[a,c]

[a] University of Ferrara, Via Savonarola, 9 – 44121, Ferrara, Italy
[b] Department of Public Health (AUSL) - UO Igiene Pubblica - Via Fausto Beretta, 7 – 44121 Ferrara, Italy
[c] SCENT S.r.l., Via Quadrifoglio 11, 44124, Ferrara, Italy
[d] MIST E-R s.c.r.l., Via P. Gobetti 101, 40129, Bologna, Italy
[e] Ospedale del Delta, Via Valle Oppio, 2 – Lagosanto, FE, Italy
[f] MNF - Micro Nano Facility, Bruno Kessler Foundation, Via Sommarive 18, 38123, Trento, Italy

A R T I C L E I N F O

Keywords:
Gas sensors
Nanostructures
Colorectal cancer
Screening
FOBT
Clinical validation

A B S T R A C T

Colorectal cancer screening is fundamental to decreased mortality related to the target disease. This pathology is diffused worldwide for both men and women and its curability rate, when identified at stage I, is up to 90%. Fecal occult blood test is currently the methodology adopted in many countries as a screening on population, but it shows a very high percentage of false positives, leading to non-operative colonoscopies performed on people who are often elderly and already debilitated. The use of an economic and easy-to-use method alongside fecal occult blood test would improve effectiveness of the screening. Here, the results so far obtained in the clinical validation protocol, started in May 2016, using a patented device with a core of chemoresistive gas sensors, are shown. The device can identify the difference between the fecal exhalation odor of two categories of subjects: healthy and those affected by high-risk adenomas or tumors. Moreover, further calibration of the instrument for the recognition of low-risk adenomas is on-going. The tests are compared to fecal occult blood test positives and colonoscopy results. In this work the most recent results as well as improvements in screening method are presented, useful for future large-scale production of the device.

1. Introduction

Tumor volatile biomarkers in human body fluids can be exploited to carry out non-invasive methods of cancer screening. The production of biomarkers is due to two main processes; namely, cell membrane peroxidation and metabolic alterations, different for each type of adenoma/carcinoma [1–7]. Our research on colorectal cancer (CRC) started in 2013 with the hypothesis that CRC- biomarkers are also present inside the intestinal atmosphere, affecting fecal composition. Based on works reported in references [1] and [2], we performed our preliminary studies on CRC-biomarkers (e.g., 1-iodo-nonane and decanal) [8–10] with the reconstruction of an artificial intestine within a laboratory setup. However, it being impossible to reproduce realistic population screening with this *a-priori* approach, starting with a list of CRC-biomarkers in breath, we moved towards the analysis of real fecal sample emanations. The identification of the difference between two diverse classes of fecal samples without knowing the real fecal odor composition (from healthy and tumor-affected subjects) is an *a-posteriori* approach that at first represented a bet, due to the unavailability of similar prior works in the literature, with the exception of a parallel study by de Meij et al [11] reporting a difference between fecal samples from healthy and CRC-affected subjects that employed a commercial electronic nose. Although the use of an electronic nose for preventive population screening is somewhat complicated and unspecific in a hospital setting, this research demonstrated that CRC-biomarkers really affect fecal odor. Our *a-posteriori* approach is not based on the calibration of a sensors system on specific colorectal biomarkers commercially bought, but on a statistical analysis of real fecal sample emanations with unknown composition. However, the device described in the present work differs from a commercial nose in that, after calibration, the algorithm does not require further training so as to be employed in other, identical devices.

[★] Presented at IMCS 2018 Conference, Vienna, Austria, July 15–19, 2018.

[*] Corresponding author at: Department of Physics and Earth Science, University of Ferrara, Via Saragat 1, I-44121, Ferrara, Italy.
E-mail address: giulia.zonta@unife.it (G. Zonta).

https://doi.org/10.1016/j.snb.2019.127062
Received 18 October 2018; Received in revised form 9 August 2019; Accepted 29 August 2019

Among the various types of cancer, CRC is a major worldwide problem. According to data from the American Cancer Society, CRC has been classified as the third most commonly diagnosed cancer type in the USA. Moreover, the lifetime risk of developing CRC is about 1 in 21 (4.7%) for men and 1 in 23 (4.4%) for women. However, it shows a high curability rate, up to 90%, when identified at stage I [12]. This is the reason for which an efficient preventive population screening is crucial to avoid degeneration of the disease into malignant stages. Fecal occult blood test (FOBT) has been adopted in many countries (e.g., Italy, France, UK) as a screening method. In Ferrara (Italy) it began in 2005 and is performed every two years on people aged between 50 and 69 years old [13]. Nevertheless, FOBT shows a very high percentage of false positives (more than 60% counting both low-risk adenomas and tumors) due to intestinal non-tumor bleeding, leading to a very high number of non-operative colonoscopies, performed on people often elderly and debilitated.

In this work, the current results of the clinical validation protocol of a device capable of distinguishing between fecal exhalation of healthy and CRC-affected patients are shown. SCENT A1 [14] is a patented device (Italy, UK and Germany), developed by the Sensors Laboratory (SL) at the University of Ferrara, capable of performing preventive screening for CRC using the odor of fecal samples. In fact, it has been shown that fecal odor can be altered by the presence of tumor biomarkers inside the intestine [15]. The device consists of a pneumatic system that conveys fecal exhalations to the sensing core, consisting of five MOX sensors, chosen following laboratory tests with specific CRC-biomarkers and a feasibility study [8–10,15]. In May 2016, the clinical validation protocol began, involving Santa Anna Hospital in Ferrara, the University of Ferrara (UNIFE), the Ospedale del Delta of Lagosanto, the AUSL of Ferrara and the start-up SCENT S.r.l. The SCENT A1 experimental test is proposed to all screening users in Ferrara (50–69 years of age) who showed positive for FOBT, before undergoing colonoscopy (gold standard). The protocol description is laid out in more detail in Section 2.3.

2. Materials and methods

2.1. The device

SCENT A1, already described in detail in a previous publication [10,15,16], is a portable device composed of a microfluidic system, specific electronics, a sensing core with five MOX sensors, and a sensing unit. Sensors are of chemoresistive type, capable of varying their resistance due to a change in the gaseous environment. Each sensor is composed of a thick-film of nanostructured semiconductor material printed onto an alumina substrate (sized 2,54 mm × 2,54 mm), two comb-shaped gold electrodes and a platinum heater [16]. The response (R) is defined as $\frac{\Delta G}{G}$ for n-type sensors, where ΔG is the difference between film conductance in the presence of a gas (G_{gas}) and in ambient air (G). For p-types, R is the negative reciprocal of the former quantity. Sensors chosen for the analysis after a feasibility study [10,15,16] are five MOX sensors made of iron and samarium oxide ($SmFeO_3$); two different solid solutions of tin and titanium oxides (ST20), the latter with the addition of gold nanoparticles (ST25 + Au); a solid solution of titanium, tantalum and vanadium oxide (TiTaV); and indium oxide (In_2O_3) [16]. The names in parentheses are the labels for each material. Fig. 1 shows a dynamic response curve for the five chosen sensors. From the shape of this curve, all the features required for the analysis are extracted, as described in Section 2.4.

2.2. Sample collection and conservation

Stool samples to be analyzed are conserved inside standard containers (ARTSANA SpA Feces Container STER 18140). The patient must follow the same collection procedure as for FOBT, with the only difference being that feces must be immediately placed in a freezer rather than a fridge so as to inhibit bacterial activity. Multiple tests with the same sample are avoided so as to guarantee perfect conservation of the fecal compound and to comply with the protocol directions. In this phase, the sample must not be disturbed or altered by the operator after thawing. Moreover, multiple samples from the same patient are not considered here, in order not to complicate the collection procedure for the patients and to comply with the FOBT protocol in Ferrara. Sample transportation takes place in a thermal bag. Half an hour before the beginning of analysis, feces can be defrosted by the operator and prepared inside the SCENT A1 sample box. The quantity of fecal sample inside the container must comply with certain guidelines so as to facilitate the analysis by the operator and is described in a leaflet. However, the amount of sample does not change the outcome of the measurement, as the latter depends strictly on the evaporation dynamics.

However, the sample is not divided into more parts to increase the statistics, as it would not add information to the algorithm and would complicate the procedure for the operator, departing from the guidelines established in the protocol.

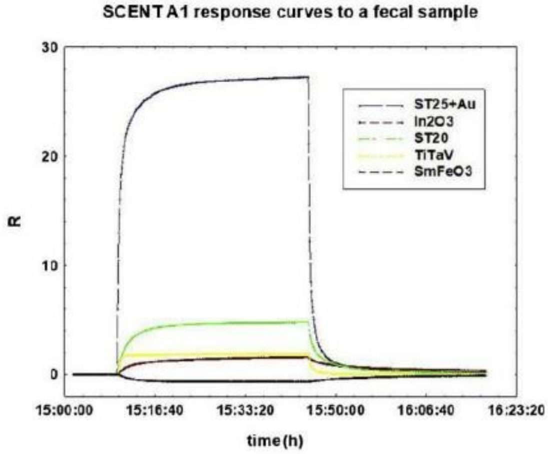

Fig. 1. example of the dynamic response (R) curve vs time, expressed in hours, of the five sensors of SCENT A1 to a fecal sample positive to FOBT coming from the protocol statistics. The p-type sensor SmFeO3 is maintained here with its original reversed shape signal, to better visualize the physical behavior of this material.

2.3. Clinical validation protocol

After a feasibility study performed in collaboration with the Department of Morphology, Surgery and Experimental Medicine at the University of Ferrara (UNIFE), described in detail in references [14–16], the approval of the Ethical Committee was obtained to begin a clinical survey. As mentioned, the clinical validation protocol began in May 2016 in Ferrara [17], and all patients being screened who show positive for FOBT are offered the SCENT A1 experimental test before undergoing colonoscopy, the widely accepted gold standard. Patients who agree to join the project, after signing a release at the time of the doctor's interview, are required to bring an additional sample of frozen feces to be submitted for SCENT A1 testing. From the beginning of the study about 90% of subjects agreed to take part in the experiment. Up to the present time, over 300 fecal samples from those who showed positive for FOBT have been measured using the device, 100 of which have already been compared to colonoscopy. This triple comparison database, among FOBT, SCENT A1 and the gold standard, is useful for obtaining important data on the efficiency of the current screening and on the potentialities of SCENT A1 to improve it.

2.4. Data collection and analysis

Specialized software, developed by the present authors using LabView, allows recording of the output voltage related to each sensor during the analysis and to automatically generate the dynamic response curve. In previous works by the present authors, [16] the method employed for data analysis relied on the use of a support vector machine (SVM) [18,19] method on a total of 20 parameters, four for each sensor of the array. The four parameters chosen are:

i) Maximum value of the derivative (D_{max}) of the response curve;
ii) time (t) to reach the 10% of D_{max} from the beginning of the analysis (t_0);
iii) response at time t (R);
iv) integral of response curve from t_0 to t;

t_0 has been chosen to be the time at which the derivative of the response curve reaches D_{max}, and therefore the response curve from flat (environmental air baseline) starts to grow due to the arrival of fecal fumes at the sensors. First, the SVM was employed as an indicator of how well data is classified by labelling populations into three categories, following colonoscopy outputs: i) cancer and high-risk adenomas (POS); ii) low-risk adenomas (LOW); iii) healthy control subjects (NEG). For high-risk adenomas we considered these categories: three or more adenomas; one adenoma larger than 10 mm in size; adenoma with villous component or high-grade dysplasia (HDG). For low-risk adenomas: 1–2 adenomas smaller than 10 mm in size; tubular adenoma; or low-grade dysplasia (LGD). SVM is not employed in its pure form but adapted to a three-classes classifier through one-by-one comparison. In Fig. 2, the confusion matrix updated to a total of 100 comparisons with the gold standard (colonoscopy outcomes) is shown. Here this method correctly classified 90% of NEG, 100% of CRC and 57% of LOW. This first approach was employed to set-up the database that will serve for double-blind tests. A double-blind test is a procedure in which neither the subjects nor the experimenters know which subjects are in the test and control groups during the actual course of the experiments. For "subjects" here we intend not only the patients but also the doctor performing the screening, while the "experimenter" is the expert performing data analysis of SCENT A1. With regard to this, by employing the prior statistics [16] without the inclusion of the last three additional positive samples, a first double-blind test was carried out. Six fecal samples (4 POS and 2 NEG) already with colonoscopy outcomes were employed for double-blind test simulation. These samples are indicated in Table 1 and were tested with the algorithm without any *a-priori* label. All positive samples with CRC were identified by the SCENT A1 test with classification probabilities near 100%. One of the two negatives was correctly identified, while the other was classified as a low risk with 60.9% probability (38.1% as negative and 1% as positive). This first double-blind approach highlights the discriminatory capacities of the method, especially with regard to positive subjects. Despite the encouraging results, this method suffers from two principal limitations with respect to the future production of the device on a large scale. First, it does not automatically consider a double-blind check, which must be performed at a second step after having obtained a robust database. This makes the analysis software not easy-to-use by a non-qualified operator. Second, the method is based on a five-sensor array [16], and the more sensors used the greater the difficulty in reproducing the device. To solve these problems, the method now employs only two sensors, thanks to the use of the k-fold cross validation test [20]. Here, the original sample is randomly partitioned into a number (k) of equal sized subsamples. A single subsample is kept for testing the model (validation data), while the remaining (k–1) subsamples serve as training data. The cross-validation process is repeated k times, rotating the validation data subsamples to produce a single estimation. In the analysis reported in the confusion matrices in Table 2, the subsample number was fixed at k = 8 after numerous attempts, being the choice with the largest score value even if with different k-value the results were all similar in substance. Matrices have been labelled as M1-M8. Actual classes are shown in the rows, while predicted classes in the

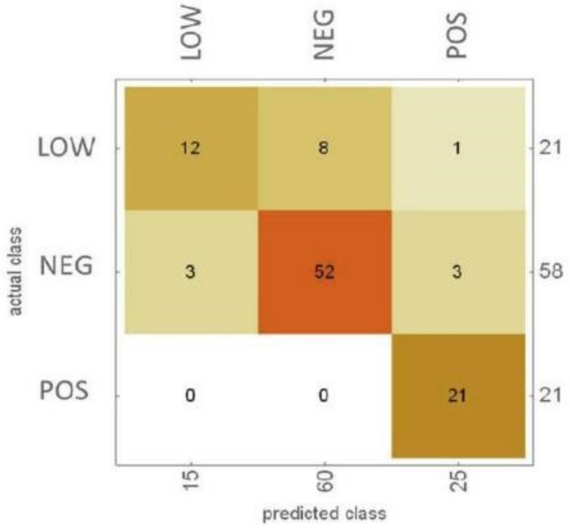

Fig. 2. confusion matrix made with 100 samples (21 LOW, 58 NEG, 21 POS) tested with SCENT A1, already resulted positives to FOBT and then compared with the gold-standard (colonoscopy).

Table 1
Six fecal samples (4 POS and 2 NEG) with colonoscopy outcomes employed for double blind test. Four positive samples with CRC have been identified by SCENT A1 test with classification probabilities near 100%. One of the two NEG has been correctly identified, while the other one has been classified as a low risk with 60.9% probability.

SAMPLE	STATUS	%LOW	%NEG	%POS
1	POS	0,5	0,2	99,3
2	POS	0,2	0	99,8
3	POS	0	0	100
4	POS	0	0	100
5	NEG	40,6	59.0	0,4
6	NEG	60,9	38,1	1

Table 2
Confusion matrices M1-M8 obtained with the k = 8 subsamples. In each of the 8 tests one subsample is employed as validation data set, while the other 7 as training data set. Actual classes are on the rows, while predicted classes on the columns.

	M1				M2				M3		
	POS	LR	NEG		POS	LR	NEG		POS	LR	NEG
POS	6	0	0	POS	4	0	0	POS	6	2	0
LR	2	8	0	LR	0	5	0	LR	0	7	2
NEG	4	0	51	NEG	2	0	60	NEG	2	2	50
	M4				M5				M6		
	POS	LR	NEG		POS	LR	NEG		POS	LR	NEG
POS	5	0	0	POS	4	0	0	POS	2	0	0
LR	0	10	0	LR	0	8	0	LR	0	8	0
NEG	2	0	54	NEG	0	0	58	NEG	0	2	58
	M7				M8						
	POS	LR	NEG		POS	LR	NEG				
POS	5	0	0	POS	8	0	0				
LR	0	5	0	LR	0	7	2				
NEG	0	0	60	NEG	0	0	53				

/

Table 3
Number of false positives (FP), false negatives (FN) and samples related to each matrix M1-M8 in Table 2.

	FP	FN	SAMPLES
M1	0.073	0	71
M2	0.032	0	71
M3	0.037	0	71
M4	0.036	0	71
M5	0	0	70
M6	0	0	70
M7	0	0	70
M8	0	0	70

columns, and for each cross-validation the number of false positives and negatives generated is reported. In Table 3 the number of false positives and negatives related to each of the 8 matrices M1-M8 is reported. On average, the false negatives (FN) are always zero, while the false positives (FP) are 0.013. The power of this method ensures an instantaneous outcome, which has been applied to the data just two sensors. The double-blind is guaranteed by the fact that both the doctor who performed the colonoscopy and the SCENT A1 data analyst (via project contract with an external institution) do not know the results of each other's work whilst carrying out their analysis. Only the referent of this research work is aware of the health status of the subjects through the gold standard results. Moreover, given that the population of positives is less than that of negatives, this method manages to re-normalize the information, balancing the two classes. The sensors chosen for this trial (out of the previous five-sensor array) are SmFeO3 and ST20. Details of the nanostructures and composition of these materials have already been published in previous work [16].

3. Discussion and conclusions

Previously reported results demonstrate the capability of the test in correctly identifying individuals with CRC among all FOBT-positive patients.

However, among FOBT positives (e.g., see Fig. 2), there are many more negatives (NEG 58%) than cancers (POS 21%) or low-risk adenomas (LOW 21%). For this reason, despite the method of analysis being able to take into account these numerical differences, it is crucial to augment the statistics in order to add information to the database. In parallel to this study, tests with another identical prototype and in a laboratory setup are on-going, in order to state the reproducibility of the sensing materials employed. Further research will focus on the determination of the surface reactions responsible for the different sensor response trends, dependent upon the fecal sample status obtained by FTIR (Fourier Transform Infrared Spectroscopy). Mass Spectrometry tests (MS) appear as a viable option to bring the research to a higher level of understanding and to identify the main tumor biomarkers that react with sensor surfaces. At the end of the present protocol, a multicenter research trial with three hospitals will begin, using three identical prototypes with a reduced number of sensor channels, a device which it is hoped will be suitable for certification and mass production. The absence of false negatives is a strong result that can most likely be explained by the huge difference in the exhalation composition of feces from healthy and tumor affected subjects. On the other hand, the absence of any type of dietary preparation before the test can add variables into the gastrointestinal flora of individuals, and this may be the reason for the imperfect classification of healthy subjects and low risk adenomas.

If the results are confirmed over a sufficiently large statistical base, the goal will be to combine FOBT with the SCENT A1 test in countries where FOBT is employed for population screening. If the outcome of FOBT is positive whilst that for SCENT A1 is negative, colonoscopy will be avoided until the next screening, which, for example, is after two years in Italy. By averaging the results shown in confusion matrices M1-M8 (Table 2), it emerges that, by performing the SCENT A1 test with the data compared so far, the percentage of colonoscopies avoided is 79%. This result does not lead to additional risks for the patient, since the SCENT A1 test does not report false positives, and less than 0.5 low risks unidentified. However, low-risk adenomas often do not degenerate into cancer or at least develop over a course of several years [21]. This leaves time for the patient to present at the next screening before the polyp becomes a carcinoma. This method may greatly improve the effectiveness of FOBT, avoiding a large number of non-operative colonoscopies on healthy subjects, without increasing the degeneration risk. Colonoscopy is in fact invasive and risky for subjects who are often not young or are debilitated.

The future application of SCENT A1 to FOBT positives as a second check makes it unnecessary to perform a protocol on the negatives. However, the present authors are considering a similar study in future on the population of FOBT negatives, opening the way to testing even in countries where there is no type of accepted pre-screening, according to the guidelines described in reference [22].

In conclusion, data currently analyzed in the clinical validation protocol of SCENT A1 since May 2016, demonstrate the discrimination capability of this non-invasive methodology with regard to CRC-affected subject fecal samples. SCENT A1 was able to identify, by means of a specific chemoresistive sensor core, all the true positives for CRC and a considerable decrease in non-operative colonoscopy is expected when the method is accepted as a test alongside the FOBT. This change will not result in an increase of tumor degeneration risk. However, SCENT A1 will allow the identification of FOBT false positives, estimated between 60% and 70% according to the data collected during the clinical validation protocol. The adjustments made to the data analysis method have made SCENT A1 more adaptable to future large-scale production, making it more easily reproducible and effective.

Acknowledgment

We thank LILT (Lega Italiana Lotta Tumori) for supporting this research through the funds obtained with the project "*Design Work Plan Call for Health Research 2016, Programma 5 per mille anno 2014*".We thank Dr. Nigel Blake, mother tongue native English speaker, for the revision of the text with regard to English language standard.

References

[1] G. Peng, M. Hakim, Detection of lung, breast, colorectal, and prostate cancers from exhaled breath using a single array of nanosensors, Br. J. Cancer 103 (2010) 542–551.

[2] D.F. Altomare, M. di Lena, Exhaled Volatile Organic Compounds Identify Patients with Colorectal Cancer, Wiley Online Library, 2013.

[3] H. Haick, Y.Y. Broza, P. Mochalsky, V. Ruzsanyi, A. Amann, Assessment, origin and implementation of breath volatile cancer markers, Chem. Soc. Rev. 43 (2014) 1423–1449.

[4] B. Tan, Y. Qiu, X. Zou, T. Chen, G. Xie, Y. Cheng, T. Dong, L. Zhao, B. Feng, X. Hu, L.X. Xu, A. Zhao, M. Zhang, G. Cai, S. Cai, Z. Zhou, M. Zheng, Y. Zhang, W. Jia, Metabonomics identifies serum metabolite markers of colorectal cancer, J. Proteome Res. 12 (6) (2013) 3000–3009.

[5] B. Szachowicz-Petelska, I. Dobrzyńska, S. Sulkowski, Z.A. Figaszewski, Characterization of the cell membrane during cancer transformation, NMR Biomed. V5 (September/October (5)) (1992) 226–233.

[6] B. Tan, Y. Qi, X. Zou, T. Chen, G. Xie, Y. Cheng, T. Dong, L. Zhao, B. Feng, X. Hu, L.X. Xu, A. Zhao, M. Zhang, G. Cai, S. Cai, Z. Zhou, M. Zheng, Y. Zhang, W. Jia, Metabonomics identifies serum metabolite markers of colorectal cancer, J. Proteome Res. 12 (6) (2013) 3000–3009.

[7] C.S. Probert, I. Ahmed, T. Khalid, E. Johnson, S. Smith, N. Ratcliffe, Volatile organic compounds as diagnostic biomarkers in gastrointestinal and liver diseases, J Gastrointestin Liver Dis. 18 (3) (2009) 337–343.

[8] C. Malagù, B. Fabbri, S. Gherardi, A. Giberti, V. Guidi, N. Landini, G. Zonta, Chemoresistive gas sensors for detection of colorectal cancer biomarkers, Sensors 14 (2014) 18982–18992.

[9] G. Zonta, G. Anania, B. Fabbri, A. Gaiardo, S. Gherardi, A. Giberti, V. Guidi, N. Landini, C. Malagù, Detection of colorectal cancer biomarkers in the presence of interfering gases, Sens. Actuators B Chem. 218 (2015) 289–295.

[10] N. Landini, G. Zonta, C. Malagù, Detection of Tumor Markers on Feces With

Nanostructured Sensors, Scholars' Press, 2015 ISBN-13: 978-3-639-76538-0.

[11] T.G. de Meij, I. Ben Larbi, M.P. van der Schee, Y.E. Lentferink, T. Paff, J.S. Terhaar sive Droste, C.J. Mulder, A.A. van Bodegraven, N.K. de Boer, Electronic nose can discriminate colorectal carcinoma and advanced adenomas by fecal volatile biomarker analysis: proof of principle study, Int. J. Cancer 134 (2014) 1132–1138.

[12] http://www.cancer.org/cancer/colonandrectumcancer/detailedguide/colorectal-cancer-key-statistics.

[13] http://www.ausl.fe.it/azienda/dipartimenti/sanita-pubblica/u-o-organizzazione-oncologica/colon-retto/opuscolo-colon-2011.

[14] SCENT A1, Italian patent number: RM20144000595, extended in Germany and UK: 3210013; patent and intellectual property of SCENT S.r.l.;.

[15] G. Zonta, G. Anania, B. Fabbri, A. Gaiardo, S. Gherardi, A. Giberti, N. Landini, C. Malagù, L. Scagliarini, V. Guidi, Preventive screening of colorectal cancer with a device based on chemoresistive sensors, Sens. Actuators B Chem. 238 (2016) 1098–1110.

[16] G. Zonta, G. Anania, C. Feo, A. Gaiardo, S. Gherardi, A. Giberti, V. Guidi, N. Landini, C. Palmonari, L. Ricci, A. de Togni, C. Malagù, Use of gas sensors and FOBT for the early detection of colorectal cancer, Sens. Actuators B Chem. 262 (2018) 884–891.

[17] Acceptance Letter from the Ethics Committee of Ferrara, Valutazione dell'accuratezza della determinazione di composti organici volatili qualibiomarker di neoplasia colo-rettale nelle feci di soggetti FOBT-positivisottoposti a colonscopia, (2016).

[18] A.J. Izenman, Modern Multivariate Statistical Techniques, Springer-Verlag, New York, 2008, https://doi.org/10.1007/978-0-387-78189-1 (ISSN1431-875X, ISBN 978-0-387-78188-4);.

[19] B. Scholkopf, A.J. Smola, Learning With Kernels: Support Vector Machines, Regularization, Optimization and Beyond, (2001) (ISBN: 9780262253437);.

[20] Michal Aharon, Michael Elad, Alfred Bruckstein, K-SVD: an algorithm for designing overcomplete dictionaries for sparse representation" (PDF), Ieee Trans. Signal Process. 54 (11) (2006) 4311–4322, https://doi.org/10.1109/TSP.2006.881199.

[21] https://www.medicitalia.it/minforma/gastroenterologia-e-endoscopia-digestiva/1598-la-colonscopia-di-sorveglianza-post-polipectomia.html.

[22] G.P. Young, C. Senore, J.S. Mandel, Recommendations for a step-wise comparative approach to the evaluation of new screening tests for colorectal cancer, Cancer 122 (2016) 826–839.

/

4.2 Tumoral Tissue Application

nanomaterials

MDPI

Article

Colorectal Cancer Study with Nanostructured Sensors: Tumor Marker Screening of Patient Biopsies

Michele Astolfi [1,2], Giorgio Rispoli [3], Gabriele Anania [4], Veronica Nevoso [4], Elena Artioli [4], Nicolò Landini [1,2], Mascia Benedusi [3], Elisabetta Melloni [3], Paola Secchiero [4], Veronica Tisato [4], Giulia Zonta [1,2] and Cesare Malagù [1,2,*]

[1] Department of Physics and Earth Sciences, University of Ferrara, Via Saragat 1/C, 44122 Ferrara, Italy; stlmhl@unife.it (M.A.); lndncl@unife.it (N.L.); zntgli@unife.it (G.Z.)

[2] SCENT S.r.l (SME company), Via Quadrifoglio 11, 44124 Ferrara, Italy

[3] Department of Biomedical and Specialist Surgical Sciences, University of Ferrara, Via Luigi Borsari 46, 44121 Ferrara, Italy; rsg@unife.it (G.R.); bndmsc@unife.it (M.B.); mlllbt@unife.it (E.M.)

[4] Department of Morphology, Surgery and Experimental Medicine, University of Ferrara, Via Luigi Borsari 46, 44121 Ferrara, Italy; ang@unife.it (G.A.); veronica.nevoso@student.unife.it (V.N.); elena01.artioli@student.unife.it (E.A.); paola.secchiero@unife.it (P.S.); veronica.tisato@unife.it (V.T.)

* Correspondence: malagu@fe.infn.it

Received: 13 February 2020; Accepted: 19 March 2020; Published: 26 March 2020

Abstract: Despite the great progress in screening techniques and medical treatments, colorectal cancer remains one of the most widespread cancers in both sexes, with a high death rate. In this work, the volatile compounds released from human colon cancer tissues were detected by a set of four different chemoresistive sensors, made with a nanostructured powder of metal-oxide materials, inserted into an innovative patented device. The sensor responses to the exhalation of a primary cancer sample and of a healthy sample (both of the same weight, collected during colorectal surgery from the intestine of the same patient) were statistically analyzed. The sensors gave reversible, reproducible, and fast responses for at least one year of continuous use, making them quite superior in respect to the existing diagnostic methods. Preliminary results obtained using principal component analysis of the sensor responses to samples removed from 13 patients indicate that the nanostructured sensors employed in this study were able to distinguish between healthy and tumor tissue samples with coherent responses (the discrimination power of the most sensitive sensor was about 17%), highlighting a strong potential for clinical practice.

Keywords: nanostructured sensors; tumor markers; colorectal cancer; human cancer biopsies; chemoresistivity; volatile organic compounds

1. Introduction

Colorectal cancer (CRC) is the third most common cancer worldwide with an increasing trend with age, and second in causing mortality in both sexes [1]. Considering the increasing incidence of this disease [1], its mortality and lethality, the impossibility of preventing its insurgence solely by changing the patient's habits, and the lack of symptoms when it is reaching an advanced phase, screening programs are of paramount importance. Equally important is the follow-up of patients that have undergone surgery and/or chemo-radiotherapy, to assess the therapy's efficacy. Therefore, it is necessary to develop new devices able to detect known tumoral markers with higher sensitivity, or to detect new ones. Since tumor growth is associated with modifications in cell metabolism, in recent years, the scientific community has focused on detecting molecules discharged by this metabolism in blood, feces, urine, breath, etc., or in samples surgically removed from patients. The molecules so far identified are:

- Vascular endothelial growth factors;
- Wastes from circulating tumor cells;
- Molecules produced by the cellular metabolism;
- Products of lipid membrane peroxidation, known as volatile organic compounds (VOCs) [2–4].

In particular, many CRC tumors are often associated with specific VOC patterns (such as benzene, alkanes, aldehydes or their derivatives) that can be detected in the body at different concentrations in healthy people [4]. Therefore, VOC detection appears highly promising as a possible marker of CRC, and more generally of other neoplastic diseases.

A project aiming to detect VOCs released by colorectal neoplasms started in 2014, with the development of a device based on an array of chemoresistive nanostructured sensors, optimized to detect these gases [5]. This device, built by the research team of a startup named SCENT S.r.l., is not invasive and is fast responding; therefore, it could be employed in the future with existing methods to improve the diagnostic ability to detect CRC at the screening stage. The instrument could also be employed in the follow-up phase of patients who have already undergone surgery and/or radiotherapy and/or chemotherapy, to assess the therapies' efficacy. The ultimate goal is to significantly decrease the number of false negatives or positives, which still affect other commonly employed pre-screening tests (such as fecal immunochemical techniques and colonoscopy).

1.1. Metal-Oxide Chemoresistive Sensors

MOX(Metal-Oxide) sensors are based on semiconducting metal-oxide material that are able to detect chemicals up in the range of tenth parts per billions, despite their rapid response. The working principle relies on the conductance change of the sensitive material induced by the reversible adsorption of ionized gas particles on the sensor surface [6–8]. The sensors are typically made from three components: a substrate, an active (sensitive) material, and a heater. The latter is in general necessary because MOX sensors are active at a specific working temperature. The substrate is an insulating layer, made in this work of sintered alumina, hosting on top the active material with interdigitated gold contacts, and on the bottom, the heater (a typical sensor is sketched in Figure 1) [9]. The active material is made of semiconducting metal-oxide nanoparticles (having a mean size between 50 and 200 nm), which was chemically transformed here in a viscose paste that was distributed on the top of the insulating substrate using a lithographic technique. The heater is usually a metal coil (in this work made of platinum) whose temperature is precisely set by controlling the current flowing through it.

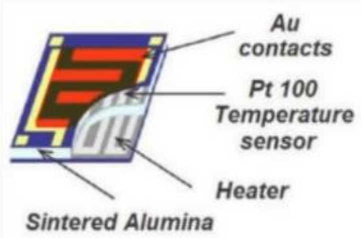

Figure 1. Top view of a sensor. The light blue central layer is the alumina substrate; the yellow lines are the gold contacts employed to connect the sensor to the external circuits; the grey coil at the bottom face of the substrate is the heater; the red area is the active material, distributed between the gold contacts.

1.2. Prototypes

A first prototype, SCENT A1, has been used to date as a CRC screening method by measuring feces samples, and it gave significant and reproducible results [5]. Since neoplasms discharge a substantial amount of specific VOCs in the blood stream [9,10], being lesions that are highly vascularized, a second prototype (named SCENT B1) was specifically developed to detect blood [9] and human tissue VOC exhalations (this study). The statistical analysis of SCENT B1 sensor responses to blood samples allowed reliable discrimination between healthy and tumor-affected subjects, and it was even able to identify tumors at evolutionary stage [9]. On this basis, SCENT B1 was then used in the present work to analyze VOCs exhaled by biopsies explanted from patients who underwent colon and/or rectal resections. The main advantage of this approach lies in measuring directly the VOCs exhaled by tumor tissue, and not altered by other chemical reactions that take place inside the human body.

2. Materials and Methods

2.1. SCENT B1 device

The patented device SCENT B1 employed in this work [11] has been widely described in a previous publication of the team [9]. In detail, the sensors used were:

TiTaV, based on titanium, tantalum and vanadium oxides;
STN, based on tin, titanium, and niobium oxides;
ST 25 + 1%Au, based on tin oxides and titanium (25%) and gold (1%);
W11, based on tungsten oxide.

All sensors were fired to a temperature of 650 °C and worked at a temperature set to 450 °C to activate the semiconductor layer, allowing chemoresistivity to occur. As shown in the literature [9,10,12], this high temperature does not affect substantially the analyte's composition nor the laminarity of the flux entering the sensing chambers. The sensors listed above were chosen according to their capability of recognizing tumor markers, which was assessed in previous research by using standard pure gases, feces [5], and blood [9].

To make the results independent of the voltage baseline at which each sensor worked, the response $R(t)$ was computed as:

$$R(t) = \frac{V_{sens}(t)}{V_0(t)} \tag{1}$$

where V_{sens} is the average voltage output of the operational amplifier connected to the sensor, used in inverting configuration, in the presence of the sample, and V_0 is the average voltage measured in its absence (i.e., when the sensor is exposed to a flux of clear air; Figure 2a).

2.2. Patient recruitment and sample collection

Colorectal tissue samples and related clinical data were obtained upon written consent from patients who underwent open or laparoscopic surgery for CRC in the Hospital of Cona, Ferrara, Italy. All patients were more than eighteen years old, of both sexes, and did not have any radiotherapy and chemotherapy before surgery; minors and pregnant women were excluded from the study; all tumors tested were malignant, and some had already metastasized to liver (multicentric bilobar replications).

The tumor and the healthy samples were cut out from the same intestine piece, trying to collect as much tumor mass as possible (since the healthy mass around the tumor was always much larger than the tumor itself), to maximize the sensor response and consequently the signal-to-noise ratio.

The time elapsed between the surgical removal of the sample and the SCENT B1 tests was kept as brief as possible. However, an average of 45 minutes elapsed between devascularization and sample explant, which was immediately immersed in culture medium. The latter, named DMEM throughout the paper, was Dulbecco's modified Eagle's medium high glucose (DMEM, Lonza®, Milan, Italy) supplemented with 10% fetal bovine serum (Euro Clone, Milan, Italy), l-glutamine at 1% (Lonza), and the antibiotics penicillin (100 U/ml) and streptomycin (100 μg/ml) at 1% (Lonza). Moreover, about two additional hours elapsed between the transport and sample preparation; therefore, a significant number of cells were lost during these three hours, but this was roughly the same for both healthy and tumor cells.

2.3. Sample handling

Careful dissection was employed to isolate as much as possible of the cancer and the healthy tissue, both trimmed to have the same mass, which was assessed with mg accuracy (average sample mass 0.282±0.052 gr; range: 0.0432 gr–0.676 gr; n=13). The samples were then carefully washed with phosphate buffered saline (PBS, 1X, Lonza) supplemented with penicillin (100 U/ml), streptomycin (100 μg/ml), and amphotericin B (250 μg/ml) at 1% (Lonza), to eliminate as much blood, feces residue, and other organic debris as possible, and to further sterilize the samples. The cleanliness of the latter was routinely checked by viewing them on a screen connected to a high-sensitivity digital CMOS camera, using a 2.3 megapixel CMOS sensor (C11440-36U, Hamamatsu Photonics, Tokyo, Japan) coupled to a microscope (TE 300, Nikon, Tokyo, Japan) with high magnification (Figure S1). Further details of sample handling are described in the supplementary materials.

2.4. Ethics approval and informed consent

The trial protocol and the informed consent form were presented, accepted, and retrospectively registered by the Ethical Committee of the District of Ferrara, with trial number 170484, on 13 July 2017.

3. Results

First, we analyzed the average ratio of the response of each sensor to VOCs exhaled by a sample and the response of the sensor to a flux of clean air, using Formula 1, (Figure 2; see Section 2). The samples were DMEM (see Section 2), a healthy tissue sample, and its tumor tissue counterpart (i.e., both taken from the same surgical sample); all sensors were simultaneously exposed to the VOCs exhaled by the samples. The sensors gave responses that were reversible (the baseline was fully recovered following a sample measurement), reproducible (an example is shown in Figure 2a, where the response of a sensor to DMEM had similar amplitude to the one recorded after the healthy and tumor sample measurement), and quite fast (the sensor response reached a steady state typically in less than half an hour) for at least one year of continuous use.

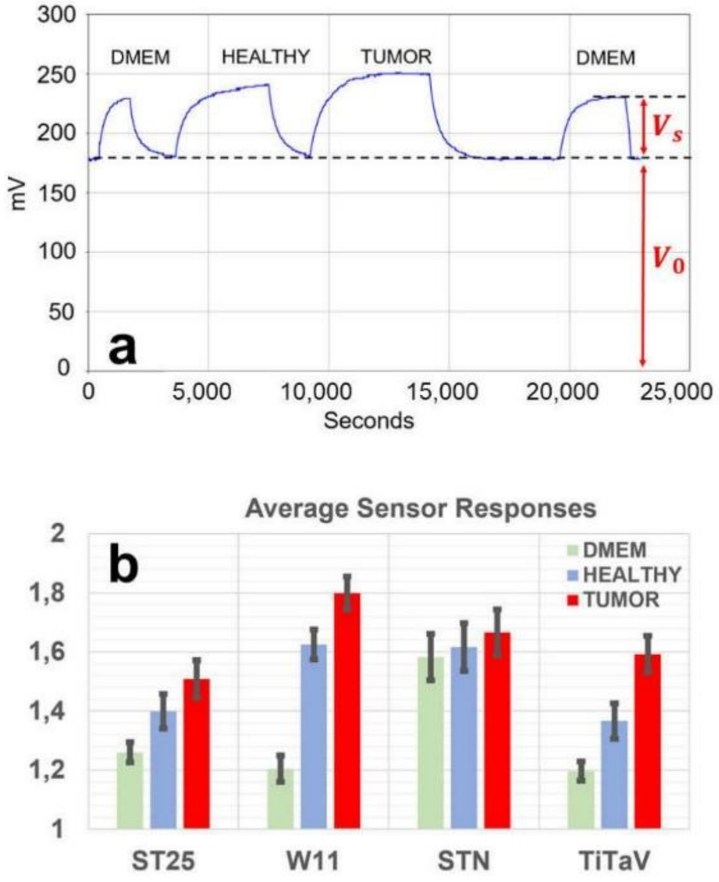

Figure 2. a) Experimental protocol and time-course of a representative sensor response. The response amplitude of the sensor with the highest discrimination power, TiTaV, (titanium, tantalum, and vanadium oxide) is plotted vs. time; the sensor was exposed to the following sample sequence: clean air/DMEM/clean air/healthy sample/clean air/tumor sample/clean air/DMEM/clean air. **b**) Average sensor responses. Bar graph of the average ratio (n=13) between the sensor response to a flux of air containing the gasses exhaled by DMEM (green bars), healthy tissue (light blue), and tumor tissue (red); and its response to a flux of clean air (baseline); error bars represent the standard error. The sensors employed were ST25 (tin and titanium oxide), W11 (tungsten oxide), STN (tin, titanium, and niobium oxide), and TiTaV.

The sensor discrimination power to discern between healthy and tumor samples, given by:

$$discrimination\ power = \left(\frac{T}{H} - 1\right) \times 100 \tag{2}$$

resulted in: ~7.8% for ST25, ~10.7% for W11, ~3% for STN, and ~16.6% for TiTaV (H is the average ratio of each sensor response to a healthy sample; i.e., the light blue bar height of Figure 2b; T the tumor one; i.e., the red bars). Given the poor selectivity exhibited by the STN sensor for the sample type considered here, its responses were therefore not considered in the following statistical analysis.

To better assess the discrimination power of the set of three sensors (ST25, W11, and TiTaV), their responses were further analysed with principal component analysis (PCA). The three eigenvectors of the covariance matrix (PC1, PC2, PC3), calculated from the three-dimensional plot of the sensor responses, were plotted one vs. the other (PC1 vs. PC2, PC2 vs. PC3, and PC1 vs. PC3) to construct the two-dimensional dispersion graphs.

The plot of PC1 vs. PC3 was the most discriminating one, and it contained the largest share of the total variance of the covariance matrix (about 90.3% of information, Figure 3). The confidence ellipses resulting from the score plot of PC1 vs. PC3 were well separated, further indicating that the strategy employed to develop SCENT B1 to discriminate between healthy tissues and cancerous ones was promising.

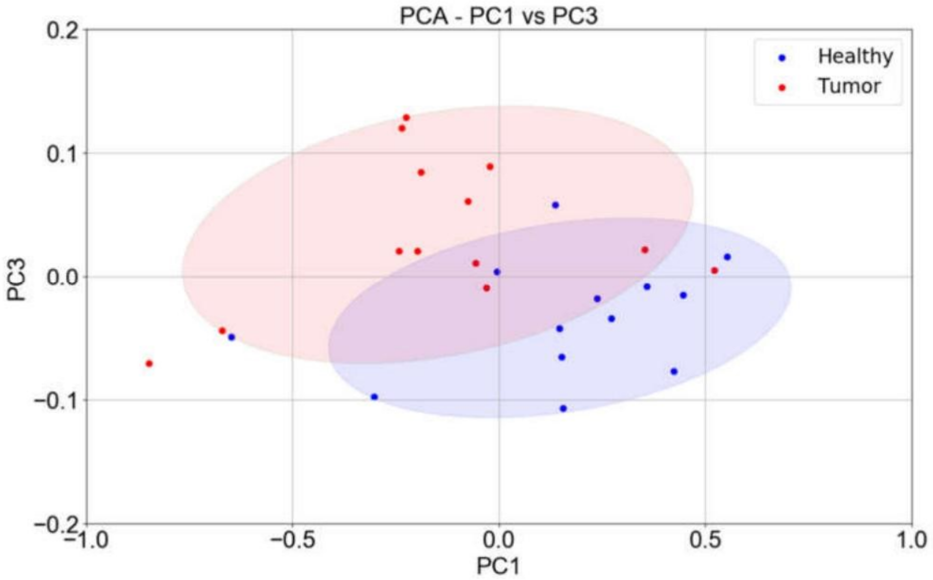

Figure 3. PCA (principal component analysis) of sensor responses—PC1 vs. PC3. PCA score plot (blue points: healthy tissues; red points: tumor tissue) constructed with the responses (*n*=13) of the ST25, W11, and TiTaV sensors only.

To further explore the discriminating power of SCENT B1, we also considered the tumor grade index, which quantifies the differentiation grade of tumor cells [13], therefore expressing the tumor's malignancy. In principle, a high-grade tumor, growing faster than a low-grade one, should have a higher metabolism and consequently a larger production of known VOCs and/or different ones because of cell indifferentiation. Therefore, it is expected that high-grade tumors generate sensor responses different to the low-grade ones. As a control, we plotted PC1 vs. PC3 of the healthy tissue only to distinguish the healthy counterparts of the high-grade tumors from the low-grade ones.

As expected, the points relative to the healthy tissue counterparts of the high-grade tumors (red) were completely confused with the low-grade ones (blue; Figure 4a). Indeed, a healthy sample removed from a certain intestine area is believed to produce the same type and amount of VOCs independent of the presence or not of a tumor (of whatsoever grade) in another area. The PCA performed on tumor tissue responses (Figure 4b) produced instead two concentric confidence ellipses, where all the points (but one) relative to the low-grade tumor samples (blue) were concentrated in an ellipse (violet), while all the points relative to the high-grade tumor samples (red) were outside of the violet ellipse and inside the larger one (pink).

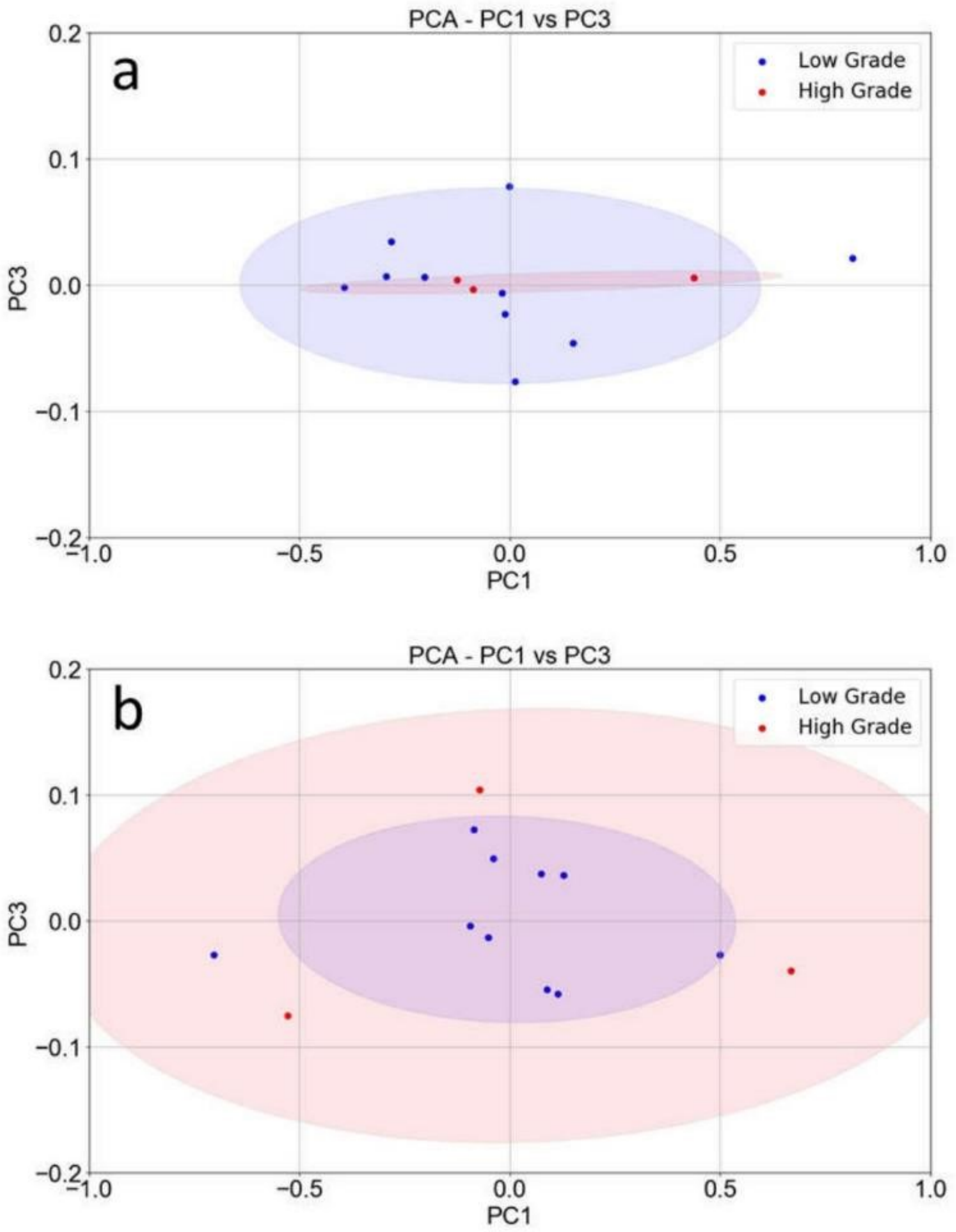

Figure 4. PCA of sensor responses related to tumor grade index: **a**) PC1 vs. PC3 score plot constructed with the responses (n=13) of the ST25, W11, and TiTaV sensors to the healthy sample counterparts of the low-grade tumors (blue points) and to the high-grade ones (red points). **b**) PC1 vs. PC3 score plot constructed with the responses (n=13) of the same sensors to the low-grade tumor samples (blue points) and to the high-grade ones (red points).

4. Discussion

As expected, the sensor response amplitudes were larger in the presence of the tumor tissue in respect of the same mass of healthy tissue. Indeed, tumor cells exhale more VOCs than the healthy ones because of a higher growth rate and, consequently, an accelerated metabolism of the former in respect to the latter.

Despite the poor selectivity and discrimination power exhibited by the STN sensor for the sample types considered here, the other three sensors (ST25, W11, and mainly TiTaV) were instead able to distinguish healthy from tumor samples, with a different selectivity (Figure 2b): This gives a key rationale to design sensors with better and better sensitivity and discriminating power.

In general, the sensitivity (TPR) and specificity (TNR) of the performance of a binary classification test are defined as:

$$TPR = \frac{TP}{P} \qquad\qquad TNR = \frac{TN}{N} \tag{3}$$

where P is the number of subjects of the total, N_t, that are positive to the test, $N_t - P = N$ are the negative ones (control subjects), and TP and TN are the number of true positives and true negatives (to the test), respectively. This approach cannot be applied here, because the population of N_t subjects are all positive, i.e., affected by CRC tumors, and from these patients, an intestine piece was surgically removed from which both a tumor and healthy sample were isolated. Therefore, strict interpretation of TPR and TNR is meaningless here, since no measures were performed on healthy subjects. It is still possible to give an estimate of these parameters, reinterpreting them on the basis of the PCA analysis (Figure 3) if P is considered the number of tumor samples and $N_t - P = N$ the number of healthy control samples. On the basis of Figure 3, excluding the points outside the confidence ellipses and considering the points inside the common area as false positives and false negatives, the sensitivity and specificity results are $TPR = 66.6\%$ and $TNR = 69.2\%$. These values must be considered with caution, since PCA is a qualitative method to classify data and, in general, an accurate evaluation of sensitivity and specificity requires much larger samples than the one presented here.

These results were quite encouraging considering the strong limits of the measurements performed: First of all, the tumor mass extracted after surgery was limited because of the necessity to perform a histological analysis for cancer staging. Moreover, the samples were composed of different kinds of healthy connective tissue and intestine cells—fat, red, and white blood cells, floral bacteria, feces residues, and neoplastic cells—possibly in different development stages, making it impossible even to distinguish healthy samples from tumor ones, despite the high quality of their microscope images (Figure S1, Supplementary Materials). Another limitation is due to the possible tissue damage occurring during the elapsed time between surgery and the experimental session (see Section 2).

5. Conclusions

This paper is intended as a feasibility study to find the most suitable sensors and statistical analysis to discriminate as well as possible between the VOCs exhaled by tumors and healthy samples. The set of nanostructured chemoresistive sensors—ST25, W11, and TiTaV—employed in this study proved to be capable of discriminating between healthy and tumor-affected biopsies, and even able to distinguish their grade of differentiation. These encouraging results will be followed by a wider study, which will involve many more cases and broaden the ongoing collaboration with pathologists. The final goal is the future development of pre- and post-screening devices that could add to existing methods, such as conventional colonoscopy, to improve tumor detection.

6. Patents

The Scent B1 device is patented in Italy with patent number: 102015000057717 [11].

Supplementary Materials: The following are available online at www.mdpi.com/xxx/s1: Figure S1: Optical microscope images from colorectal tissue.

Author Contributions: Conceptualization, M. Astolfi, G. Rispoli, N. Landini, G. Zonta, and C. Malagù; data curation, M. Astolfi and G. Rispoli; formal analysis, M. Astolfi; investigation, M. Astolfi and G. Rispoli; methodology, G. Anania, V. Nevoso, E. Artioli, N. Landini, M. Benedusi, E. Melloni, P. Secchiero, and V. Tisato; project administration, C. Malagu'; resources, G. Anania, V. Nevoso, E. Artioli, M. Benedusi, E. Melloni, P. Secchiero, and V. Tisato; software, M. Astolfi; supervision, P. Secchiero and C. Malagu'; validation, M. Astolfi and G. Zonta; visualization, G. Rispoli; writing—original draft, M. Astolfi, G. Rispoli, and G. Anania; writing—

review and editing, M. Astolfi and G. Rispoli. All authors have read and agreed to the published version of the manuscript.

Funding: Financial support was provided by SCENT s.r.l., grants from the Project FAR (Fondo di Ateneo per la Ricerca, University of Ferrara) 2016-2018 to G. R. and C. M., and Project FIR 2016 to G. R. (Fondi perl'Incentivazione della Ricerca, University of Ferrara).

Acknowledgments: Many thanks to Andrea Margutti and Sandro Gherardi for technical assistance.

Conflicts of Interest: The authors declare no conflicts of interest.

References

1. Bray, F.; Ferlay, J.; Soerjomataram, I.; Siegel, R.; Torre, L.; Jemal, A. Global cancer statistics 2018: GLOBOCAN estimates of incidence and mortality worldwide for 36 cancers in 185 countries. *CA Cancer J. Clin*. **2018**, *6*, 394–424.
2. Phillips, M.; Gleeson, K.; Hughes J.M.B.; Greenberg, J.; Cataneo, R.N.; Baker, L.; McVay, W.P. Volatile organic compounds in breath as markers of lung cancer: A cross-sectional study. *Lancet* **1999**, *353*, 1930–1933.
3. Probert, C.S.; Khalid, T.; Ahmed, I.; Johnson, E.; Smith, S.; Ratcliffe, N.M. Volatile organic compounds as diagnostic biomarkers in gastrointestinal and liver diseases. *J. Gastrointest. Liver Dis*. **2009**, *18*, 337–343.
4. Altomare, D.F.; Di Lena, M.; Porcelli, F.; Trizio, L.; Travaglio, E.; Tutino, M.; Dragonieri, S.; Memeo, V.; De Gennaro, G. Exhaled volatile organic compounds identify patients with colorectal cancer. *Br. J. Surg*. **2013**, *100*, 144–150.
5. Zonta, G.; Anania, G.; Feo, C.; Gaiardo, A.; Gherardi, S.; Giberti, A.; Guidi, V.; Landini, N.; Palmonari, C.; Ricci, L.; et al. Use of gas sensors and FOBT for the early detection of colorectal cancer. *Sens. Actuators B* **2018**, *262*, 884–891.
6. Ponzoni, A.; Comini, E.; Concina, I.; Ferroni, M.; Falasconi, M.; Gobbi, E.; Sberveglieri, V.; Sberveglieri, G. Nanostructured Metal Oxide Gas Sensors, a Survey of Applications. *Sensors* **2012**, *12*, 17023–17045.
7. Malagù, C.; Benetti, M.; Carotta, M.C.; Giberti, A.; Guidi, V.; Milano, L.; Martinelli, G. Investigation of the humidity effects on SNO2-based sensors in CO detection. *Mater. Res. Soc. Symp. Proc.* **2006**, *915, 0915-R07-05*.
8. Wang, C.; Yin, L.; Zhang, L.; Xiang, D.; Gao, R. Metal Oxide Gas Sensors: Sensitivity and Influencing Factors. *Sensors* **2010**, *10*, 2088–2106.
9. Landini, N.; Anania, G.; Fabbri, B.; Gaiardo, A.; Gherardi, S.; Guidi, V.; Rispoli, G.; Scagliarini, L.; Zonta, G.; Malagù, C. Neoplasms and metastasis detection in human blood exhalations with a device composed by nanostructured sensors. *Sens. Actuators B* **2018**, *271*, 203–214.
10. Wang, C.; Li, P.; Lian, A.; Sun, B.; Wang, X.; Guo, L.; Chi, C.; Liu, S.; Zhao, W.; Luo, S.; et al. Blood volatile compounds as biomarkers for colorectal cancer. *Cancer Biol. Ther*. **2014**, *15*, 200–2016.
11. SCENT B1. Italian Patent No. 102015000057717, Malagù C., Gherardi S., Zonta G., Landini N., Giberti A., Fabbri B., Gaiardo A., Anania G., Rispoli G., Scagliarini L., 02-10-2015.
12. Giberti, A.; Benetti, M.; Carotta, M.C.; Guidi, V.; Malagu, C.; Martinelli, G. Heat exchange and temperature calculation in thick-film semiconductor gas sensor systems. *Sens. Actuators B* **2008**, *130*, 277–280.
13. National Cancer Institute. Tumor Grade, 2013. Available online: https://www.cancer.gov/about-cancer/diagnosis-staging/prognosis/tumor-grade-fact-sheet (accessed on 25 November 2019).

4.3 Blood Application

molecules

MDPI

Article

Tin, Titanium, Tantalum, Vanadium and Niobium Oxide Based Sensors to Detect Colorectal Cancer Exhalations in Blood Samples

Michele Astolfi [1,2], Giorgio Rispoli [3], Gabriele Anania [4], Elena Artioli [4], Veronica Nevoso [4], Giulia Zonta [1,2] and Cesare Malagù [1,2,*]

[1] Department of Physics and Earth Sciences, University of Ferrara, 44122 Ferrara, Italy; stlmhl@unife.it (M.A.); zntgli@unife.it (G.Z.)
[2] SCENT S.r.l (SME company), Via Quadrifoglio 11, 44124 Ferrara, Italy
[3] Department of Neuroscience and Rehabilitation, University of Ferrara, 44121 Ferrara, Italy; rsg@unife.it
[4] Department of Medical Sciences, University of Ferrara, 44121 Ferrara, Italy; ang@unife.it (G.A.); elena01.artioli@student.unife.it (E.A.); veronica.nevoso@student.unife.it (V.N.)
* Correspondence: malagu@fe.infn.it

Abstract: User-friendly, low-cost equipment for preventive screening of severe or deadly pathologies are one of the most sought devices by the National Health Services, as they allow early disease detection and treatment, often avoiding its degeneration. In recent years more and more research groups are developing devices aimed at these goals employing gas sensors. Here, nanostructured chemoresistive metal oxide (MOX) sensors were employed in a patented prototype aimed to detect volatile organic compounds (VOCs), exhaled by blood samples collected from patients affected by colorectal cancer and from healthy subjects as a control. Four sensors, carefully selected after many years of laboratory tests on biological samples (cultured cells, human stools, human biopsies, etc.), were based here on various percentages of tin, tungsten, titanium, niobium, tantalum and vanadium oxides. Sensor voltage responses were statistically analyzed also with the receiver operating characteristic (ROC) curves, that allowed the identification of the cut-off discriminating between healthy and tumor affected subjects for each sensor, leading to an estimate of sensitivity and specificity parameters. ROC analysis demonstrated that sensors employing tin and titanium oxides decorated with gold nanoparticles gave sensitivities up to 80% yet with a specificity of 70%.

Keywords: nanostructured sensors; tumor markers; colorectal cancer; blood; chemoresistivity; volatile organic compounds

check for updates

Citation: Astolfi, M.; Rispoli, G.; Anania, G.; Artioli, E.; Nevoso, V.; Zonta, G.; Malagù, C. Tin, Titanium, Tantalum, Vanadium and Niobium Oxide Based Sensors to Detect Colorectal Cancer Exhalations in Blood Samples. *Molecules* **2021**, *26*, 466. https://doi.org/10.3390/molecules26020466

Academic Editor: Luigi Perbellini
Received: 30 November 2020
Accepted: 14 January 2021
Published: 17 January 2021

1. Introduction

Nowadays, cancer is a ubiquitous pathology of crucial impact, and it is expected to rank as the leading cause of death worldwide in the 21st century. Its incidence and mortality are progressively increasing due to the fast population growth and the increase in average age. For this reason, early cancer detection is a challenge for many researchers working in many different fields, and different techniques have been implemented to allay the cancer threat. The main techniques proposed till now range from the main risk factor reduction to longer standing screening and early detection programs [1]. The reduced mortality for some types of cancer, following the adoption of these practices [2], is forcing the scientific community to develop more and more efficient screening techniques and follow-up protocols, in particular to defeat one of the most common localized cancer pathologies, such as colorectal cancer (CRC).

CRC has an important impact on public health, being the third most common malignancy for incidence and second for mortality worldwide [3] accounting for 11% of all cancer diagnoses. It affects people of both sexes, typically aged 65 or over [4] and its symptoms are various, although it may be asymptomatic for a long time, so delaying its detection. The most common CRC symptoms are: rectal bleeding, followed by chronic blood loss leading to physical fatigue and anemia [5]. Usually, endoscopic procedures are recommended as first investigation if CRC is suspected, allowing to collect specimens from presumable tumor lesions and to obtain a reliable and suitable anatomopathological examination (cancer diagnosis validation and histological characterization) [6].

The nowadays available CRC screening techniques, crucial in early-stage tumor detection, are divided into non-invasive and invasive tests. The main non-invasive tests are:

- Guaiac-based fecal occult blood test (gFOBT) and the newer fecal immunochemical test (FIT), based on the detecting blood in stools through chemical and immunochemical reactions respectively [7,8];
- The novel multitarget stool DNA (MT-sDNA), combining FIT and altered DNA biomarkers detection in CRC cells entrapped into the stool [7,8];
- Radiologic examinations including capsule endoscopy [9] and Computed tomographic colonography (CTC) [10].

The most widely used invasive tests are the flexible sigmoidoscopy (FS) and colonoscopy that, in addition to the direct visualization, allow to collect a pathology specimen. For instance, Italian guidelines recommend pancolonoscopy or alternatively recto-sigmoidoscopy associated with virtual colonoscopy and double contrast barium enema [11,12]. European Member States recommend to men and women with ages ranging between 50 and 74 years to undergo screening programs, such as annual or biennial FOBTs, eventually followed by colonoscopy in case of positive results [13]. FIT is the most used screening test worldwide, because it is particularly user friendly, more reliable than gFOBT and does not require dietary restrictions, though it counts a 65% of false positives (due to non-tumoral bleedings) so leading to a huge amount of non-operative colonoscopies [14].

In the last years, many efforts have been made by the research community in CRC screening, introducing new solutions that improve the efficiency and reliability of CRC detection in respect to the commonly used aforementioned techniques. The most common approach is to detect CRC by analyzing easily collectable biological samples (by means of low invasive processes) such as urine, breath, blood, serum and stools. In the last decade, the technologies developed for this scope have shown a significant clinical impact, improving the understanding of disease genesis, the related processes and its evolution [15].

Many current studies demonstrate that neoplastic lesions, such as CRC, emit specific VOCs (volatile organic compounds, such as benzene, alkanes, aldehydes or their derivatives), that can be exploited as reliable cancer markers [16]. VOCs are generally wastes discharged in a living organism, produced by the altered metabolism of cancer cells and, their detection is nowadays a promising and popular topic among researchers. With this aim, the company SCENT S.r.l. started a project in 2014 to detect VOCs exhaled by stool samples by using a hand-made prototype, named SCENT A1, based on an array of five MOX sensors, to identify CRC presence [14,17–20]. The reproducibility, the reliability, the non-invasiveness, and the quickness in detecting CRC exhibited by SCENT A1, made it suitable to be combined to the current screening methods, sensibly improving their ability to detect this pathology.

A second hand-made prototype, named SCENT B1 [21], was developed from the same company, to detect VOCs in CRC human tissue samples, cell cultures [22] and blood [23]. Encouraging results were achieved in the human tissue application where the statistical analysis of its sensor responses, performed by using principal component analysis approach, showed the SCENT B1 ability to discriminate between healthy and tumor samples [24]. Moreover, this device was even able to identify the tumor grade, that assesses the undifferentiation level of the tumor cells [24]. On this promising basis, knowing that neoplasms are highly vascularized lesions discharging a substantial amount of VOCs in the blood stream [25], the SCENT B1 device is used here to detect VOCs exhaled by blood samples collected from CRC affected subjects and blood samples collected from healthy ones (as controls), by using a novel sensor combination. The final goal is to find the sensors that perform the best discrimination between healthy and tumor affected subjects.

2. Results

A typical voltage sensor signal, generated by the electronics of SCENT B1 prototype and acquired by the dedicated software LSS4 (“Laboratorio Sensori—Sensori 4 v1.0”), is shown in Figure 1. The response was firstly characterized by a baseline of amplitude V_0 when the sensor (ST25 + 1%Au in Figure 1) was exposed to a dry and clean air stream. A large voltage change occurred when it was exposed to the sample chamber headspace VOCs of a blood sample collected from a healthy subject (HB; the application timing is shown by the thick blue line, and is about 5 min), attaining a steady state amplitude V_{GH}, and an even larger voltage change when it was exposed to a blood sample collected from a tumor affected one (TB; thick red line), attaining a steady state amplitude V_{GT} (Figure 1).

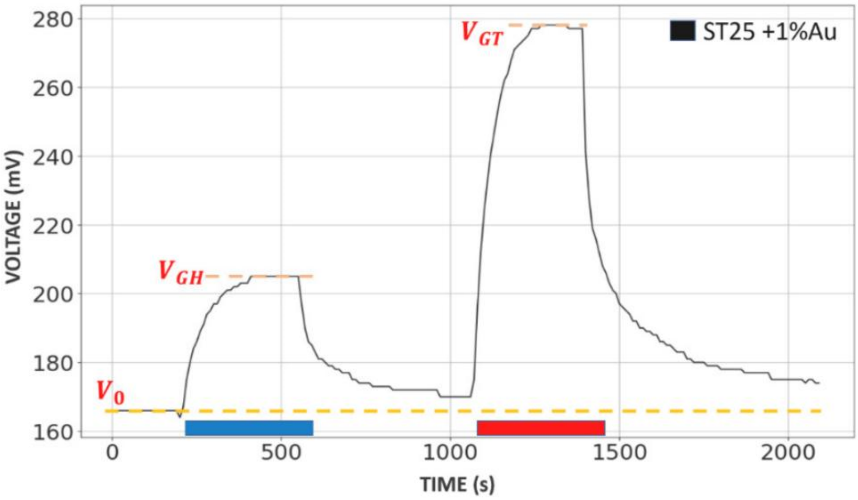

Figure 1. Example of an output voltage sensor signal. A ST25 + 1%Au sensor was exposed to a stream of clean and dry air (giving a steady voltage response of amplitude V_0; orange dotted line) in between a stream of air polluted with the blood headspace volatile organic compounds (VOCs) of a healthy subject (HB; which timing is shown by the thick blue line; response attained a steady state amplitude V_{GH}, orange dotted line) and of a tumor affected one (TB; thick red line; steady state amplitude V_{GT}, orange dotted line). The steady state was considered to be achieved when voltage did not change more than 2/3 mV in 30 s.

Sensor response $R(t)$ (Figure 2) was computed by dividing its voltage response $V_G(t)$ when it was exposed to a blood sample by the baseline $V_0(t)$, exploiting the relation:

$$\mathrm{R}(t) = \frac{V_G(t)}{V_0(t)} \tag{1}$$

The time-dependence of the baseline indicate that it could slightly drift during the experiment.

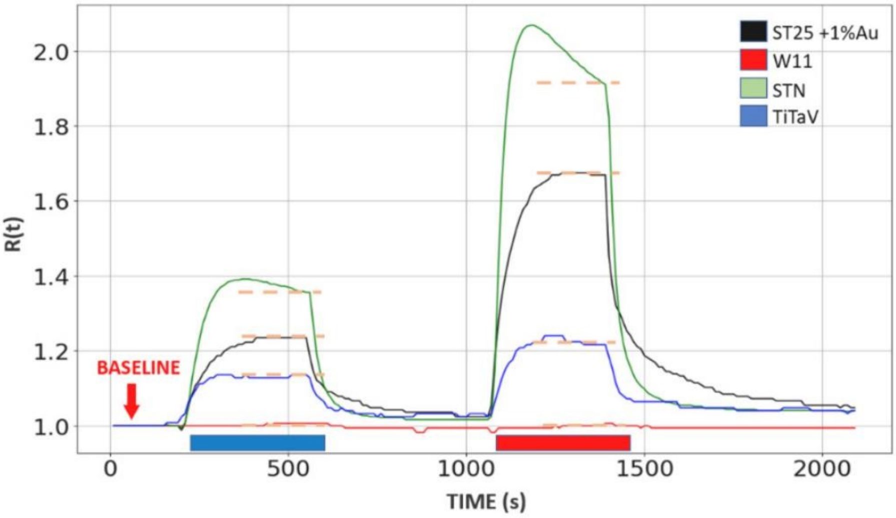

Figure 2. Computed response amplitude of the four sensors. The ST25, W11, STN and TiTaV sensor responses (represented by black, red, green and blue curves, respectively) to the HB exhalation (thick blue line) and of a TB one (thick red line); average steady state amplitudes are shown by the orange dotted lines.

The average *R(t)* amplitude plot at the steady state and its standard error were estimated for each sensor, when exposed to the TB headspace VOCs (*n* = 25; AVE. T, Table 1; Figure 3 red bars) and HB ones (*n* = 23; AVE. H, Table 1; Figure 3 blue bars). The "discriminating power" (i.e., how much the TB average responses are different than the HB ones in percentage; D.P., Table 1) of each sensor can be calculated from their average responses (Figure 3) by the Equation (2):

$$\text{D.P.} = 100 \times \left(\frac{R_T}{R_H} - 1 \right) \tag{2}$$

where R_T and R_H are the average sensor responses to TB and HB respectively. The confidence intervals given by the Student's t-test, were calculated for the TB and HB responses (C.I. T, C.I. H respectively, Table 1), with 90% of confidence level (α = 0.1).

Table 1. Average sensor responses statistical analysis.

SENSOR	AVE. T	AVE. H	D.P. (%)	C.I. T	C.I. H
ST25	1.43 ± 0.05	1.24 ± 0.02	16.09 ± 4.79	1.35–1.52	1.21–1.26
W11	1.11 ± 0.02	1.09 ± 0.02	2.31 ± 3.98	1.07–1.15	1.05–1.12
STN	1.95 ± 0.06	1.62 ± 0.06	20.51 ± 6.69	1.84–2.06	1.52–1.72
TiTaV	1.22 ± 0.02	1.15 ± 0.02	6.13 ± 2.88	1.18–1.25	1.12–1.17

Through the one sensor approach (Figure 4), i.e., plotting all the responses (*n* = 48) per sensor in ascending order, it is easy to conclude at first sight that each sensor, excluded W11, gave the largest responses when exposed to TB headspace VOCs.

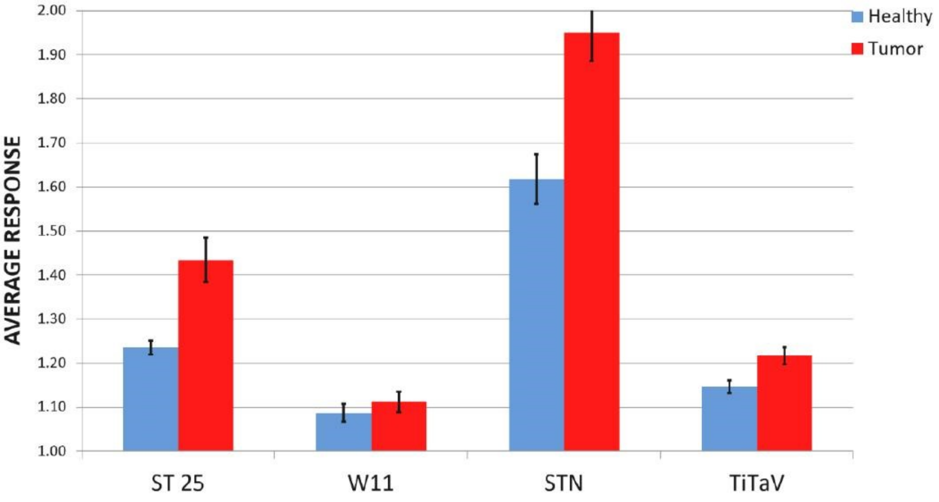

Figure 3. Basic statistical analysis of sensor responses. Average response and standard error of the response of the four sensors to HB (blue bars, n = 23) and to the exhalations of TB (red bars, n = 25).

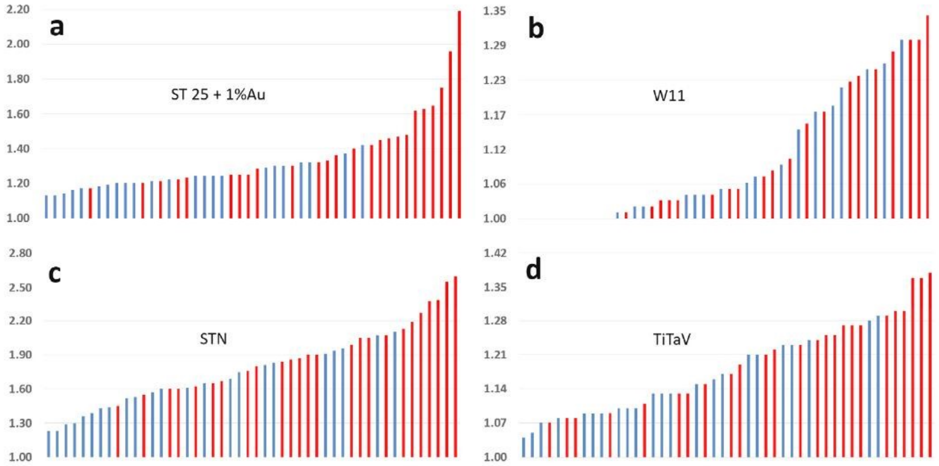

Figure 4. One sensor approach. Responses of the four sensors, sorted by their amplitude and plotted in ascending order. Blue and red bars are the sensor responses to healthy subject blood samples and tumor ones, respectively. (**a**), ST25 sensor; (**b**), W11; (**c**), STN; (**d**), TiTaV.

In order to estimate the sensor "diagnostic" capability, i.e., the accuracy in discriminating TB and HB, sensitivity (i.e., the ability to recognize true positives; Equation (3a) and specificity (i.e., the ability to recognize true negatives; Equation (3b) parameters, computed through the relations Equations (3a) and (3b), were used to perform the ROC (receiver operating characteristic) analysis.

$$\text{Sensitivity} = \frac{TP}{(TP + FN)} \tag{3a}$$

$$\text{Specificity} = \frac{TN}{(TN + FP)} \tag{3b}$$

where *TP* and *TN* are the number of true positives and true negatives, respectively (i.e., the number of the actual sick and healthy subjects, correctly recognized by a screening device); *FP* and *FN* are the number of false positive and of false negative, respectively (i.e., the number of the healthy and sick subjects, but recognized as positives and negatives by a screening device respectively).

The ROC analysis consists in the plot of sensitivity vs. 1−specificity; (Figure 5) the area under the resulting curve (AUC) ranges between 0.5 and 1.0, representing no and perfect diagnostic ability, respectively (i.e., closer is the AUC to one, higher is the test accuracy). The calculated AUC for each sensor employed here were (in decreasing order): 0.82 (ST25), 0.78 (STN), 0.73 (TiTaV), and 0.60 (W11; (Figure 5). The cut-off (or threshold) amplitude for each sensor that discriminates between HB and TB with the best sensitivity and specificity compromise can be calculated on the basis of the maximum Youden's index. The latter is defined as the maximum vertical distance between the equity line (i.e., the points where sensitivity = 1−specificity) and the ROC curve [26].

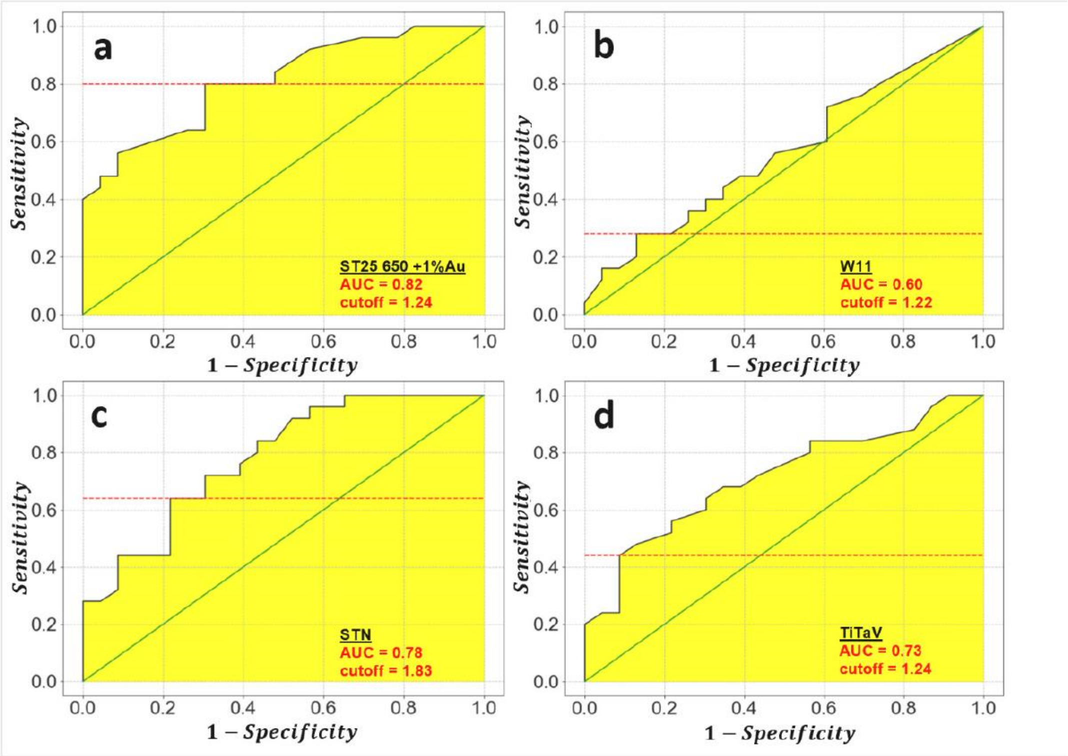

Figure 5. Evaluation of the threshold response amplitude discriminating between tumor affected and healthy affected subjects (TB and HB). Plots of the ROC (receiver operating characteristic) curves of the four sensors (black lines), the equity line (green), and the threshold amplitude computed by the maximum Youden's index (red dashed lines). The AUC (area under curve) is highlighted in yellow. (**a**), ST25 sensor; (**b**), W11; (**c**), STN; (**d**), TiTaV.

3. Discussion

All sensors gave a larger voltage change in the presence of TB with respect to HB, although with diverse amplitudes. A qualitative analysis of the four sensor responses plotted in ascending order (Figure 4), indicates instead that ST25 + 1% Au is the best sensor to discriminate between TB and HB, followed by STN and TiTaV; in any case, both analyses indicate that all sensors, but W11, clearly discriminated between TB and HB. Furthermore, the confidence intervals C.I. T and C.I. H (Table 1), computed through the Student's t-test, were clearly separated for ST25 and STN sensors, making them the best choice among the sensors used here. A more thoughtful scrutiny of the sensor responses, to assess their "diagnostic" accuracy, is provided by the ROC analysis (Figure 5). The larger is the AUC (Figure 5 and Table 2), the more accurate is the discrimination ability of a sensor: on this basis, ST25 and STN sensors exhibit the best compromise between sensitivity and specificity (Table 2, last two columns). From the ROC curves it is possible to calculate, on the basis of the maximum Youden's index, the cut-off response amplitude for each sensor (Table 2), necessary to discriminate between HB and TB with the best compromise between specificity and sensitivity.

Table 2. Sensor performances on the basis of the ROC analysis.

SENSOR	AUC	CUT-OFF	SENS.%	SPEC.%
ST25	0.82	1.24	80.0	69.6
STN	0.78	1.83	64.0	78.3
TiTaV	0.73	1.24	44.0	91.3
W11	0.60	1.22	28.0	87.0

ST25 and STN sensors, both based on tin-oxide and titanium-oxide semiconducting nanoparticles, have demonstrated to be the best sensors (among the tested ones) to reveal blood samples headspace cancer VOCs. However, the less performing sensor in this study (W11) was instead very suitable in detecting VOCs exhaled from tumor biopsies surgically removed from colon [24]. In general, therefore, a sensor could be suitable or not to detect a particular tumor, depending upon the sample kind (i.e., blood, biopsy, saliva, breath, urine, etc.) or, for the same sample kind, to what tumor it is targeted (i.e., colon, brain, kidney, etc.).

Considering the unsuitability of W11 sensor, and the positive but poor results of TiTaV one to detect blood VOCs, a new prototype is under development where these two sensors will be replaced with more suitable ones.

4. Materials and Methods

4.1. Used Nanostructured MOX Sensors

The sensors used here are based on semiconductor materials able to detect gases with extremely low detection limit (up to tens of parts per billion), but still having a reliable and quick response. Their sensitive material is made of metal-oxide nanoparticles (MOX) capable of varying their conductivity if ionized gas particles are reversibly adsorbed on their surface [27–29].

MOX sensors are typically made by three components (Figure 6):

- A substrate, a stiff and insulating layer (here made of sintered alumina), hosting two interdigitated gold contacts, necessary to connect the sensor to the transduction circuit;
- A sensitive material (or active material), a porous thick film (~20 μm of thickness) of semiconducting MOX nanoparticles (spherical nanograins with size ranging between 50 and 200 nm).
- A heater, a platinum coil necessary to activate the sensor at the proper working temperature which is controlled by means of the current flowing in the coil.

All the sensors used here are entirely designed, produced, and assembled in the "Laboratorio Sensori" of the University of Ferrara, Italy, using techniques commonly employed to produce thick film MOX sensors. The MOX nano powder, composing the sensing material, is synthesized through sol gel technique [30], then transformed in a printable viscous paste adding a small amount of organic vehicles and glass frit (a mixture of glassy silicon oxides). This final metal-oxide nanostructured paste is distributed on the alumina substrate between the two gold interdigitated contacts by means of a screen-printing machine (Aurel C920). The printed substrate is subjected to drying and firing thermal processes: the former takes place at low temperatures (about 100 °C) and the latter at higher ones (up to 850 °C). Finally, it is welded by a thermo-compression bonding technique on a four pin TO-39 socket, suitable to connect the sensor into the transduction circuit and to make it easily replaceable [31].

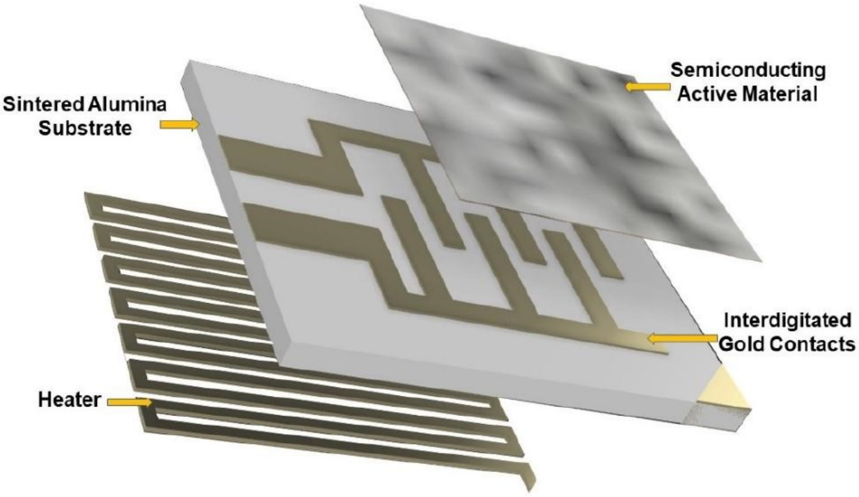

Figure 6. Three-dimensional (3D) representation of components constituting a metal oxide (MOX) sensor.

4.2. SCENT B1 Prototype Working Principle

SCENT B1 [21] (Figure 7) is made by a pneumatic air system and an electronic circuit. The pneumatic system (Figure 8) draws air from the environment and blows with a constant pressure into a carbon filter (to stabilize as much as possible the air humidity and temperature) and a 0.2-micron filter (to remove pollutants like particulate matter or aerosols) by means of an electronic pump.

Figure 7. SCENT B1 device.

This clean air flux can be guided directly to the sensors (whose response in this condition is considered the "baseline", detailed below), or into the sample chamber (where it carries the sample headspace chemical compounds) before reaching the sensors by means of a three-way valve. The electronic circuit converts the resistance change of each sensor active film in a potential difference by means of an inverting operational amplifier. The acquired voltage vs. time is plotted by using a software developed ad hoc by SCENT S.r.l. research team, then transformed in a response $R(t)$ vs. time plot exploiting the relation (1), to obtain a plot independent by the measured physical quantity and the baseline amplitude, generally diverse for each sensor [24].

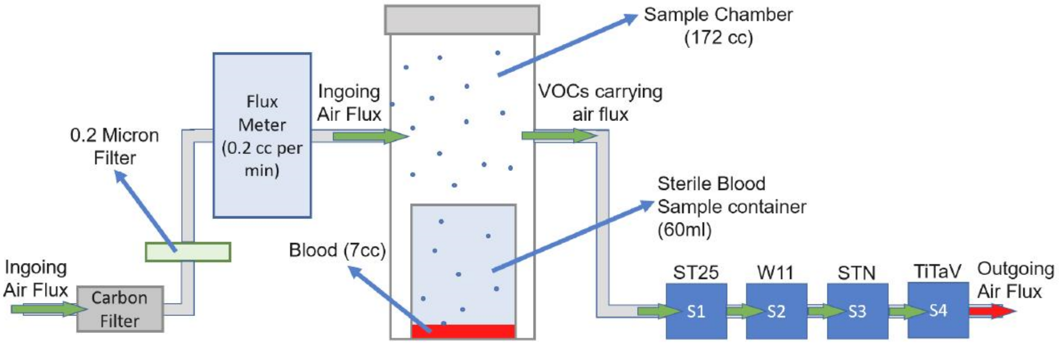

Figure 8. Block scheme of SCENT B1 pneumatic system.

4.3. SCENT B1 Hosted Sensors

The VOCs composing the headspace of TB and HB have been measured here by using the patented prototype SCENT B1 [21]. The MOX sensors equipping this prototype, carefully selected after many laboratory tests (carried out for many years on pure gases, feces, and human cancer biopsies at the "Laboratorio Sensori, LS" of University of Ferrara, Italy [see 14, 17-24]), are:

- ST 25 + 1%Au, based on tin and titanium (25%) oxides and enriched with gold nanoparticles (1%);
- W11, based on pure tungsten oxide;
- STN, based on the same percentage of tin, titanium, and niobium oxides;
- TiTaV, based on titanium, tantalum and vanadium oxides.

All the sensors used here worked at the temperature of 450 °C to fully activate the sensing layer and maximize the sensor detection capabilities [32].

4.4. Patient Recruitment and Sample Analysis

Blood samples were collected in K3 EDTA sample tubes of 7 cc of volume, from CRC affected and healthy subjects (used as controls) by the medical staff of the Hospital of Cona, Ferrara, Italy. The samples were kept at room temperature, transferred in a sterile container (60 mL), placed in the sample chamber (172 cc; Figure 8), and measured after 20/30 s to generate the headspace. Each blood sample was measured only once because testing different samples collected from the same patient gave the same results; moreover, we tried to minimize the amount of blood drawn from a patient. We did not measure the same blood sample many times to avoid possible sample alteration.

These subjects were selected with the following constraints:

- Age over eighteen years old;
- Both sexes;
- No any neoadjuvant therapy;
- No pregnant women.

Other factors, as sex, age, tumor stage and grade, were not correlated with the sensor responses because it would need a very large number of subjects to have statistical significance. CRC and healthy subjects (used as controls) were about 50% male and 50% female; the average age of CRC patients was higher than the one of the healthy subjects, because this pathology, as widely described in the Introduction, affects mainly people older than 50 years. Moreover, the young age of the healthy subjects ensures the minimization of the number of the risk factors. Nevertheless, considering the encouraging results obtained here, a new research study has been started employing a much larger number of subjects, aimed to follow the patients pre- and post-surgery, and the results will be correlated with the above-mentioned factors.

The blood samples and the patient's related clinical data were gathered upon written consent from patients, before undergoing to open or laparoscopic surgery as primary CRC treatment. The trial protocol and the informed consent form were presented, accepted, and retrospectively registered by the Ethical Committee of the District of Ferrara, with trial number 170484, on 13 July 2017.

The blood sample (collected about one hour before) was carefully poured into a stool specimen container avoiding any contamination; the container was then placed inside the sample chamber of SCENT B1 device to be measured at room temperature.

5. Conclusions

The work consists in a feasibility study to select the most suitable sensors and statistical approach to discriminate between TB and HB headspace VOCs. Each sensor here employed, but W11, proved to be capable of discriminating between HB and TB, with different accuracy. The sensors used here for the first time on blood samples, whose responses were analyzed with receiver operating characteristic method, led to identify the ST25 and STN as the best sensors (AUC: 0.82 and 0.78, respectively), whose sensitivity resulted of 80.0, 69.6 and specificity of 64.0, 78.3, respectively, exhibiting well separated confidence intervals. Considering the costs, easiness and non-invasiveness, our test is comparable with only fecal immunochemical test, although its sensitivity in CRC detection is not clearly known, because the blood presence in the stools is not always correlated to this pathology. These encouraging results led us to undertake a further study, replacing W11 sensor with a more suitable one, and involving many more cases and a follow up protocol aimed to monitor the patients after surgery, to reveal possible tumor relapses. The final goal consists in building a pre- and post-screening device that, combined to existing screening methods (such as FIT analysis and conventional colonoscopy in the case of CRC) could improve tumor detection efficacy and accuracy, also extending its application to other types of tumor.

6. Patents

The Scent B1 device is patented in Italy with patent number: 102015000057717 [21].

Author Contributions: Conceptualization, M.A.; methodology, M.A. and G.R.; software, M.A.; validation, M.A.; formal analysis, M.A. and E.A.; investigation, M.A. and E.A.; resources, G.A., E.A. and V.N.; data curation, M.A.; writing—original draft preparation, M.A.; writing—review and editing, M.A., G.R., and G.A,; visualization, G.Z.; supervision, C.M.; project administration, C.M.; funding acquisition, C.M. and G.R. All authors have read and agreed to the published version of the manuscript.

Funding: Financial support was provided by SCENT s.r.l., grants from the Project FAR (Fondo di Ateneo per la Ricerca, University of Ferrara) 2016-2020 to G. R. and C. M., and Project FIR 2016 to G. R. (Fondi per l'Incentivazione della Ricerca, University of Ferrara).

Institutional Review Board Statement: The study was conducted according to the guidelines of the Declaration of Helsinki, and approved by the Ethics Committee of the District of Ferrara, with protocol code 170484, on 13 July 2017.

Informed Consent Statement: Informed consent was obtained from all subjects involved in the study.

Data Availability Statement: The data presented in this study are available on request from the corresponding author. The data are not publicly available due to privacy and ethical restrictions (GDPR, (UE) n. 2016/679).

Acknowledgments: Many thanks to Casa di Cura Quisisana S.r.l. to have partially funded this research and many thanks to Andrea Margutti and Sandro Gherardi for technical support.

Conflicts of Interest: The authors declare no conflict of interest.

Sample Availability: Samples of the compounds are available from the authors.

References

1. Bray, F.; Ferlay, J.; Soerjomataram, I.; Siegel, R.L.; Torre, L.A.; Jemal, A. Global cancer statistics 2018: GLOBOCAN estimates of incidence and mortality worldwide for 36 cancers in 185 countries. *CA: A Cancer J. Clin.* **2018**, *68*, 394–424. [CrossRef]
2. Brenner, H.; Stock, C.; Hoffmeister, M. Effect of screening sigmoidoscopy and screening colonoscopy on colorectal cancer incidence and mortality: systematic review and meta-analysis of randomised controlled trials and observational studies. *BMJ* **2014**, *348*, g2467. [CrossRef] [PubMed]
3. Rawla, P.; Sunkara, T.; Barsouk, A. Epidemiology of colorectal cancer: incidence, mortality, survival, and risk factors. *Prz. Gastroenterol.* **2019**, *14*, 89–103. [CrossRef] [PubMed]
4. National Cancer Institute Cancer Statistics. Available online: https://www.cancer.gov/about-cancer/understanding/statistics (accessed on 22 December 2019).
5. Amaro, A.; Chiara, S.; Pfeffer, U. Molecular evolution of colorectal cancer: from multistep carcinogenesis to the big bang. *Cancer Metastasis Rev.* **2016**, *35*, 63–74. [CrossRef] [PubMed]
6. Linee Guida AIOM 2018 Tumore al colon. Available online: https://www.aiom.it/linee-guida-aiom-2018-tumori-del-colon/ (accessed on 24 November 2020).
7. Colorectal Cancer Screening Tests. Available online: https://www.cancer.org/cancer/colon-rectal-cancer/detection-diagnosis-staging/screening-tests-used.html (accessed on 23 December 2020).
8. Hewitson, P.; Glasziou, P.; Irwig, L.; Towler, B.; Watson, E. Screening for colorectal cancer using the faecal occult blood test, Hemoccult. *Cochrane Database Syst. Rev.* **2007**, *2007*, CD001216. [CrossRef] [PubMed]
9. Li, F.; A Leighton, J.; Sharma, V.K. Capsule endoscopy: a comprehensive review. *Minerva Gastroenterol. Dietol.* **2007**, *53*, 257–272. [PubMed]
10. Scalise, P.; Mantarro, A.; Pancrazi, F.; Neri, E. Computed tomography colonography for the practicing radiologist: A review of current recommendations on methodology and clinical indications. *World J. Radiol.* **2016**, *8*, 472–483. [CrossRef]
11. A Issa, I.; Noureddine, M. Colorectal cancer screening: An updated review of the available options. *World J. Gastroenterol.* **2017**, *23*, 5086–5096. [CrossRef]
12. Chan, W.P.; Ngu, J.H.; Poh, Z.; Soetikno, R. Colorectal cancer screening. *Singap. Med J.* **2017**, *58*, 24–28. [CrossRef]
13. Navarro, M.; Nicolas, A.; Ferrandez, A. Lanas, Ángel Colorectal cancer population screening programs worldwide in 2016: An update. *World J. Gastroenterol.* **2017**, *23*, 3632–3642. [CrossRef]
14. Zonta, G.; Malagù, C.; Gherardi, S.; Giberti, A.; Pezzoli, A.; De Togni, A.; Palmonari, C. Clinical Validation Results of an Innovative Non-Invasive Device for Colorectal Cancer Preventive Screening through Fecal Exhalation Analysis. *Cancers* **2020**, *12*, 1471. [CrossRef] [PubMed]
15. Hines, R.B.; Jiban, J.H.; Choudhury, K.; Loerzel, V.; Specogna, A.V.; Troy, S.P.; Zhang, S. Post-treatment surveillance testing of patients with colorectal cancer and the association with survival: protocol for a retrospective cohort study of the Surveillance, Epidemiology, and End Results (SEER)-Medicare database. *BMJ Open* **2018**, *8*, e022393. [CrossRef] [PubMed]
16. Di Lena, M.; Porcelli, F.; Altomare, D.F. Volatile organic compounds as new biomarkers for colorectal cancer: a review. *Color. Dis.* **2016**, *18*, 654–663. [CrossRef] [PubMed]
17. Zonta, G.; Anania, G.; Feo, C.; Gaiardo, A.; Gherardi, S.; Giberti, A.; Guidi, V.; Landini, N.; Palmonari, C.; Ricci, L.; et al. Use of gas sensors and FOBT for the early detection of colorectal cancer. *Sens. Actuators B: Chem.* **2018**, *262*, 884–891. [CrossRef]
18. Malagù, C.; Fabbri, B.; Gherardi, S.; Giberti, A.; Guidi, V.; Landini, N.; Zonta, G. Chemoresistive Gas Sensors for the Detection of Colorectal Cancer Biomarkers. *Sensors* **2014**, *14*, 18982–18992. [CrossRef]
19. Zonta, G.; Anania, G.; Fabbri, B.; Gaiardo, A.; Gherardi, S.; Giberti, A.; Guidi, V.; Landini, N.; Malagù, C. Detection of colorectal cancer biomarkers in the presence of interfering gases. *Sens. Actuators B: Chem.* **2015**, *218*, 289–295. [CrossRef]
20. Zonta, G.; Anania, G.; Fabbri, B.; Gaiardo, A.; Gherardi, S.; Giberti, A.; Landini, N.; Malagù, C.; Scagliarini, L.; Guidi, V. Preventive screening of colorectal cancer with a device based on chemoresistive sensors. *Sens. Actuators B: Chem.* **2017**, *238*, 1098–1101. [CrossRef]
21. Malagù, C.; Gherardi, S.; Zonta, G.; Landini, N.; Giberti, A.; Giberti, A.; Fabbri, B.; Anania, G.; Rispoli, G.; Scagliarini, L. SCENT B1. Italian Patent No. 102015000057717, 2 October 2015.
22. Astolfi, M.; Zonta, G.; Landini, N.; Gherardi, S.; Rispoli, G.; Anania, G.; Benedusi, M.; Guidi, V.; Palmonari, C.; Secchiero, P.; et al. Chemoresistive Nanostructured Sensors for Tumor Pre-Screening. *Proceedings* **2019**, *14*, 29. [CrossRef]
23. Landini, N.; Anania, G.; Fabbri, B.; Gaiardo, A.; Gherardi, S.; Guidi, V.; Rispoli, G.; Scagliarini, L.; Zonta, G.; Malagu, C. Neoplasms and metastasis detection in human blood exhalations with a device composed by nanostructured sensors. *Sensors Actuators B: Chem.* **2018**, *271*, 203–214. [CrossRef]
24. Astolfi, M.; Rispoli, G.; Anania, G.; Nevoso, V.; Artioli, E.; Landini, N.; Benedusi, M.; Melloni, E.; Secchiero, P.; Tisato, V.; et al. Colorectal Cancer Study with Nanostructured Sensors: Tumor Marker Screening of Patient Biopsies. *Nanomaterials* **2020**, *10*, 606. [CrossRef]
25. Wang, C.; Li, P.; Lian, A.; Sun, B.; Wang, X.; Guo, L.; Chi, C.; Liu, S.; Zhao, W.; Luo, S.; et al. Blood volatile compounds as biomarkers for colorectal cancer. *Cancer Biol. Ther.* **2013**, *15*, 200–206. [CrossRef] [PubMed]
26. Hajian-Tilaki, K. Receiver Operating Characteristic (ROC) Curve Analysis for Medical Diagnostic Test Evaluation. *Casp. J. Intern. Med.* **2013**, *4*, 627–635.

27. Ponzoni, A.; Comini, E.; Concina, I.; Ferroni, M.; Falasconi, M.; Gobbi, E.; Sberveglieri, V.; Sberveglieri, G. Nanostructured Metal Oxide Gas Sensors, a Survey of Applications Carried out at SENSOR Lab, Brescia (Italy) in the Security and Food Quality Fields. *Sensors* **2012**, *12*, 17023–17045. [CrossRef] [PubMed]
28. Malagù, C.; Benetti, M.; Carotta, M.C.; Giberti, A.; Guidi, V.; Milano, L.; Martinelli, G. Investigation of the humidity effects on SNO2-based sensors in CO detection. *Mater. Res. Soc. Symp. Proc.* **2006**, *915*. [CrossRef]
29. Wang, C.; Yin, L.; Zhang, L.; Xiang, D.; Gao, R. Metal Oxide Gas Sensors: Sensitivity and Influencing Factors. *Sensors* **2010**, *10*, 2088–2106. [CrossRef]
30. Brinker, C.J.; Scherer, G.W.B. *Sol-gel science: the physics and chemistry of sol-gel processing*; Academic Press: San Diego, CA, USA, 1990.
31. Gaiardo, A.; Fabbri, B.; Giberti, A.; Guidi, V.; Bellutti, P.; Malagù, C.; Valt, M.; Pepponi, G.; Gherardi, S.; Zonta, G.; et al. ZnO and Au/ZnO thin films: Room-temperature chemoresistive properties for gas sensing applications. *Sens. Actuators B: Chem.* **2016**, *237*, 1085–1094. [CrossRef]
32. Giberti, A.; Benetti, M.; Carotta, M.; Guidi, V.; Malagù, C.; Martinelli, G. Heat exchange and temperature calculation in thick-film semiconductor gas sensor systems. *Sens. Actuators B: Chem.* **2008**, *130*, 277–280. [CrossRef]

4.4 Blood and Cell Cultures Applications

sensors

MDPI

Article

Nanostructured Chemoresistive Sensors for Oncological Screening and Tumor Markers Tracking: Single Sensor Approach Applications on Human Blood and Cell Samples

Nicolò Landini [1,*], Gabriele Anania [2], Michele Astolfi [1,3], Barbara Fabbri [1], Vincenzo Guidi [1], Giorgio Rispoli [4], Matteo Valt [1], Giulia Zonta [1] and Cesare Malagù [1]

[1] Department of Physics and Earth Sciences, University of Ferrara, Via Saragat 1/C, 44122 Ferrara, Italy; stlmhl@unife.it (M.A.); fbbbbr@unife.it (B.F.); gduvcn@unife.it (V.G.); vltmtt1@unife.it (M.V.); zntgli@unife.it (G.Z.); mlgcsr@unife.it (C.M.)

[2] Department of Morphology, Surgery and Experimental Medicine, University of Ferrara, Via Luigi Borsari 46, 44121 Ferrara, Italy; ang@unife.it

[3] SCENT S.r.l, Via Quadrifoglio 11, 44124 Ferrara, Italy

[4] Department of Life Sciences and Biotechnology, University of Ferrara, Via Luigi Borsari 46, 44121 Ferrara, Italy; rsg@unife.it

* Correspondence: nicolo.landini@unife.it

Received: 29 January 2020; Accepted: 27 February 2020; Published: 4 March 2020

Abstract: Preventive screening does not only allow to preemptively intervene on pathologies before they can harm the host; but also to reduce the costs of the intervention itself; boosting the efficiency of the NHS (National Health System) by saving resources for other purposes. To improve technology advancements in this field; user-friendly yet low-cost devices are required; and various applications for gas sensors have been tested and proved reliable in past studies. In this work; cell cultures and blood samples have been studied; using nanostructured chemoresistive sensors; to both verify if this technology can reliably detect tumor markers; and if correlations between responses from tumor line metabolites and the screening outcomes on human specimens could be observed. The results showed how sensors responded differently to the emanations from healthy and mutant (for cells) or tumor affected (for blood) samples, and how those results were consistent between them, since the tumoral specimens had higher responses compared to the ones of their healthy counterparts. Even though the patterns in the responses require a bigger population to be defined properly; it appeared that the different macro-groups between the same kind of samples are distinguishable from some of the sensors chosen in the study; giving promising outcomes for further research.

Keywords: chemoresistive sensors; blood; cells; tumor; screening; metabolites; oncology

1. Introduction

The demand for reliable devices to detect tumor biomarkers in the human body is constantly increasing. The reasons behind this lay on the advantages of early intervention on pathologies, allowing for a greater chance of healing and survival for the patients compared to taking action in the malignant state of a neoplasia not diagnosed in time. Consequently, the expenses for the National Health Systems would drop consistently while the efficiency of intervention from physicians and surgeons would increase, causing a reduction in the amount of malignant and terminal cases.

Chemoresistive semiconductor sensors, fast responding devices commonly used for pollution and alimentary screening, could be the brand-new choice of sensing units for medical devices aimed at

Sensors **2020**, *20*, 1411; doi:10.3390/s20051411

this kind of approach, as multiple studies have proved their usefulness for screening applications on different biological samples [1–7].

These works rely on previous studies on Volatile Organic Compounds (VOCs) [8–20], a wide field that has opened the door to research on the application of electronic noses, biosensors, and chemoresistive sensors for medical purposes [21–27]. The chemical markers targeted in this research have different origins, due to the various changes that tumor cell lines and masses undergo compared to their healthy counterpart:

(1) Metabolites normally emanated from cellular breath [8–10] and lipid membrane peroxidation VOCs (in both cell and blood tests) [11–13].

(2) Vascular endothelial growth factors given from neoplasm metastatization [14–17] and wastes from destroyed circulating tumor cells (blood tests only) [18–20].

In this study, we compared measures from human biological samples (blood specimens to be precise, with new tests following a published method to verify consistency with the existing literature, and thus using them as a benchmark to which we could correlate the new field of application) and responses to other forms of tumor and cellular metabolites, obtained from cell cultures, in order to verify further possible applications of these devices on different targets, and their reliability on homogenous immortalized and tumor cell cultures. Various different sensors were tested on a collection of blood samples, both from healthy and tumor affected individuals (colorectal and gastric cancer) ranging between 21 and 87 years of age, and on cell cultures (fibroblasts, human embryonic kidney cells (HEK-293) and Chinese hamster ovary cells (CHO)). The reason behind the diversification of the tumors tested was the will to verify a possible coherence between sensor responses and different neoplasms. Their responses were compared to recognize recurrent patterns from which the two populations could be distinguished, and to see if common trends could appear between the different applications, with both goals verified at the end of the work.

2. Materials and Methods

2.1. Blood Sampling

Blood specimens were harvested in the Hospital of Cona, Ferrara, Italy. The protocol and the informed consent form required for the research trial were presented, accepted, and retrospectively registered from the Ethical Committee of the District of Ferrara, with trial number 170, 484 (13 July 2017). Blood was collected with the standard medical sampling technique: drawing it from the arm veins of the individuals. The blood was classified between two different donor groups:

(1) Tumor affected individuals, more specifically, patients with colorectal cancer and stomach cancer.

(2) Healthy individuals (control group).

Blood specimens were poured in collection tubes (7 mL), leaving 1 cm of headspace in every collection tube. The test tubes were in a vacuum, thus there was no headspace air contaminating the samples before their opening. The saturated vapors, composing most of the VOCs measured from the devices, were in equilibrium with blood in the liquid phase. To perform a test, the blood tubes were quickly opened and the sample was rapidly poured in a single-use, sterile container and placed inside the specimen chamber. All test tubes contained an anticoagulant agent in order to prevent coagulation in the samples, called K3-EDTA (tripotassium ethylenediaminetetraacetic acid). This standard anticoagulant (2004, European Standard EN 14820; and German Standard DIN ISO 6710 [28,29]) was already added to the test tubes from the manufacturers, in order to inhibit the natural coagulation of blood samples by steadily and irreversibly chelating (binding) calcium ions, thus preventing blood from clotting. Its effects on blood samples have been widely studied for the concentrations standardly added to the test tubes, showing no substantial biological or chemical variations in the samples, nor of the volatile chemicals exhaled from them [30–32]. There was not any further dilution nor alteration of the collected samples.

The data set formed during this part of the work, and analyzed with the aid of the sensors array below mentioned, is composed as follows:

- Total: 15 samples collected:
    - ☐ Healthy: 8
    - ☐ Tumor affected: 7

  with the following anagraphical distribution.
- Females: 4
    - ☐ Healthy: 1
    - ☐ Tumor affected: 3
- Males: 11
    - ☐ Healthy: 7
    - ☐ Tumor affected: 4

  between the ages of 21 and 87 years old.

2.2. Cell Cultures Preparation

The following immortalized cell lines were studied in this work:

(1) Fibroblasts, derived from a primary, healthy human specimen culture, playing the role of control group.
(2) HEK 293 cells, derived from human kidney fetal cells, and immortalized with an adenovirus.
(3) CHO, immortalized Chinese hamster ovary cells.

The reason behind the use of multiple cell kinds was to test if sensors could distinguish different types between them, and not just the distinction between healthy and immortalized/tumor cells.

Immortalized cells are mutant strains of the original biologically normal ones from which they are originated, and share the following properties:

(1) Loss of the former biological function previously carried in the organism that hosted them.
(2) Continuous reproduction until nutrients and free space to reproduce are no longer available (usually 2D expansion, but for some strains closer to real tumors they also expand in 3D masses), making them closely related to neoplasms in living beings, sharing the same behavior, genesis, and metabolic mutation.

To follow the cell cultures' evolution over time, a visible ruse was taken as an advantage. In fact, how the breeding ground color changed depended on the incubation time thanks to pH indicators melted in the Dulbecco's Modified Eagle's Medium (DMEM, a standard fluid used as biological breeding ground) for this purpose (the longer the incubation time, the more it turns from pinkish to yellow because of the acidification of the breeding ground itself), proving the growth of the population (visible also through the optical microscope) due to the consumption of nutrients and the increasing concentration of wastes (diluted cellular metabolites).

Each test was realized with three Petri dishes, in order to increase the emanation surface, hosted in a sterile tripod structure. The samples' preparation has been carried out as follows:

(1) Each Petri dish (diameter = 3.5 cm) was filled with 1.5 mL DMEM (high glucose) without fetal bovine serum, with various antibiotics added (penicillin, streptomycin, and glutamine) to prevent contaminations from microorganisms that could harm the cells.
(2) Fetal bovine serum was added in such a quantity to reach 10% of the total volume of the finished breeding ground.

Cells were plated in the Petri dishes with the same starting concentrations (which was estimated using a gridded glass and the optical microscope): ~250,000 units. From these, the cells were left in groups of three Petri dishes each, in the incubator (kept at 5% CO_2 as standard preventive measure to avoid contamination from bacteria, at a temperature of 37 °C) at the same time, and then tested at different set hours and days, so that the incubation time for each group was from 4 to 48 h. For all cell samples, these two parameters were critical to define both their changes and state of proliferation during the test, and thus the increase of the plated cells' population.

2.3. Sensors Technology

Chemoresistive sensors are devices capable of converting chemical or physical quantities (like gas concentration or light wavelength) into an electric signal, occurring due to the reactions happening in the material due to the measured phenomenon (oxidation and reduction due to the gaseous analytes which react with the semiconductor surface), and thus changing the electrical properties (resistance/conductance) of the sensing material. The most important solids that display semiconductor properties are silicon, germanium, and compounds of gallium, followed by metal oxides (like tin oxide, titanium oxide, zinc oxide and their doped versions, used in this work) and non-metal oxide materials (like tin sulfide), widely used in electronic devices, nanostructures, integrated circuits, lasers, and so on. All the sensors used in this work are nanostructured, which means that the geometry of the grains composing them spans tens of nanometers. The reason for this choice of manufacture lays behind the fact that this property increases the sensitivity of the sensors, since when the average diameter of the grains is close to the dimension of the depletion region, nanometric phenomena occur, like unpinning of the Fermi level and flattening of the band bending, resulting in an intrinsic increase in the sensing material performances [33]. Each sensor is composed by a sensing film of semiconductor material (metal oxides or non-metal oxides), printed on a substrate crafted from sintered alumina. This substrate hosts a platinum heater connected to two of the electrodes present on one face of the unit, while on the other face interdigitated gold contacts are inserted. These gold contacts are the same on which the semiconductor paste is printed to close the circuit, acting as variable resistors to the presence of the gas analytes. The dimensions of this sensitive layer (substrate and semiconductor film) are 2 mm in length and 2 mm in width, while their thickness spans around 330 μm. The voltage drop is read by an inverting operational amplifier, integrated to dedicated electronics to which each sensor is connected by a custom 4 pins gold support. The connection between the gold electrodes on the substrate and these supports is performed by bonding gold wires. The resulting sensing units, bonded as described above, are 18 mm in height and 7 mm in diameter each. Since every sensor is prepared, pasted, and bonded with the exact same procedure, and the custom electronics printed on each dedicated PCB (Printed Circuit Board) is exactly the same for all of them, the design factor is normalized for all the sensing units, and does not affect their performances differently.

Table 1 shows the sensors (labeled with their given laboratory inventory name, which does not always strictly refer to their chemical composition) that were used for the detection of the tumor markers emanated from human blood samples, while these last mentioned were kept at room temperature:

Table 1. Sensors used for the blood tests, their working temperature, a brief description of their composition, and references to other works in which they are described in depth and their characterizations are published.

Sensors for Blood Tests			
Sensor	**Working Temperature (°C)**	**Composition**	**References**
W11	350	Pure tungsten oxide	[34]
TiTaV	450	Titanium, tantalum and vanadium oxides	[35]
STN	450	Tin, titanium and niobium oxides	[36–39]
ST25 650+Au	450	Tin and titanium (25%) oxides, decorated with gold (1%)	[6,36,38]

while Table 2 shows the ones used to test the immortalized cell lines:

Table 2. Sensors used for cell tests, their working temperature, a brief description of their composition, and references to other works in which they are described in depth and their characterizations are published.

Sensors for Cell Tests			
Sensor	**Working Temperature (°C)**	**Composition**	**References**
W11	350	Pure tungsten oxide	[34]
WS30 650	350	Tungsten and tin (30%) oxides	[2,40]
ZnO 850 A	450	Pure zinc oxide	[6,41]
ST25 650+Au	450	Tin and titanium (25%) oxides, decorated with gold (1%)	[6,36,38]
ST20 650	450	Tin and titanium (20%) oxides	[36,38]
SnO2	450	Pure tin oxide	[6,36,38]
SnS2	300	Tin sulfide	[42]
ZnO 850 B	350	Pure zinc oxide	[6,41]

Each sensor was put to its best working temperature, defined by laboratory tests (carried out in the laboratory of sensors of the Department of Physics and Earth Sciences, University of Ferrara) on the tumor markers previously studied, chosen from the literature [1–3,6]. The variety of sensors chosen lays upon the will to verify if chemoresistive sensors can detect variations as a whole technology, or if only some particular semiconductors can be used for screening/detection purposes, and to visualize possible correlations between their response behaviors. Further details in the sensors' functioning, the differences between the various semiconductor materials, and their characterizations can be found in literature [1–7,33–45]. The responses are standardly defined as the average value between three output voltages measured by the sensor from the same sample, as shown in the following formula [6]:

$$R = \frac{\frac{V_{sensA}}{V_{0A}} + \frac{V_{sensB}}{V_{0B}} + \frac{V_{sensC}}{V_{0C}}}{3} \tag{1}$$

having:

$V_{sensA,B,C}$ potential measured from the sensor at the exposure to the chemical markers of interest,

$V_{0A,B,C}$ potential measured from the sensor in a resting state, having only environmentally filtered air flowing into the sensor chambers.

The volatile compounds exhaled were carried by the flow of filtered environmental air (to avoid contaminations and moist alteration) through the sensor chambers, where they reacted with the semiconductor film and generated the potential difference measured and used to obtain our response R.

2.4. Sensing Device

The sensors were hosted into a patented device [national patent number: 102015000057717], SCENT B1, already presented in literature [6], during previous research on tumor markers from blood samples. The prototype consists of a hydraulic system, powered by an internal pump inflating filtered air (using carbon and anti-bacterial 0.2 μm filters on the teflon of aspiration), that leads the emanations of the specimens analyzed from the dedicated chamber where it is hosted to the gas sensors chambers, where standard SHT11 sensors are also hosted to verify the stability of temperature and humidity conditions (29 °C and 38%, respectively). Tests were carried out in a thermostatic chamber. As already proven in the previous publication, the resulting air flux is stable and laminar [6]. Once the exhalations reach the sensors chambers, they react with them, thus giving the responses that the software written in the Labview® language visualize and register for the final data analysis.

3. Results

Figures 1 and 2, Tables 3 and 4 show the results of cell tests, complete with sensors' response values. While most of the sensors proved to be able to distinguish between breeding grounds, healthy cells (which were not only tested multiple times, but also on multiple platings as shown in Figure 1, to ensure repeatability on the background emanations given from the DMEM), and immortalized cells, not all showed appreciable variations in their responses to discriminate between cells with different incubation times (that result in different cell population numerosities, as shown in Figure 3). Still, the results are really encouraging, with high responses from some sensors and wide differences between different cell types and incubation times.

Table 3. Data, average values, and standard deviations from cell cultures tests shown in Figure 1.

	ST25 650+Au	**ST20 650**	**SnO2**	**ZnO 850 A**	**SnS2**
DMEM1	2.82	2.32	1.66	1.59	1.33
	2.83	2.35	1.64	1.62	1.37
	2.86	2.29	1.65	1.56	1.38
AVERAGE VALUE	2.84	2.32	1.65	1.59	1.36
STANDARD DEVIATION	0.02	0.02	0.01	0.02	0.02
DMEM2	2.78	2.20	1.65	1.69	1.55
	2.74	2.23	1.63	1.70	1.56
	2.81	2.30	1.66	1.72	1.60
AVERAGE VALUE	2.78	2.24	1.65	1.70	1.57
STANDARD DEVIATION	0.03	0.04	0.01	0.01	0.02
FIBROBLASTS (48 h)	5.51	4.33	2.50	2.11	2.04
	5.56	4.29	2.51	2.09	2.00
	5.54	4.27	2.47	2.12	1.91
AVERAGE VALUE	5.54	4.30	2.49	2.11	1.98
STANDARD DEVIATION	0.02	0.02	0.02	0.01	0.05
FIBROBLASTS (48 h)	5.42	4.17	2.45	2.12	1.97
	5.41	4.14	2.42	2.15	1.89
	5.39	4.20	2.48	2.13	1.87
AVERAGE VALUE	5.41	4.17	2.45	2.13	1.91
STANDARD DEVIATION	0.01	0.02	0.02	0.01	0.04
HEK-293 (48 h)	9.67	7.67	3.78	3.13	2.75
	9.70	7.60	3.75	3.11	2.89
	9.68	7.63	3.82	3.09	2.86
AVERAGE VALUE	9.68	7.63	3.78	3.11	2.83
STANDARD DEVIATION	0.01	0.03	0.03	0.02	0.06
DMEM3 (48 h)	2.81	2.24	1.73	1.77	1.41
	2.79	2.30	1.70	1.75	1.43
	2.82	2.26	1.74	1.73	1.38
AVERAGE VALUE	2.81	2.27	1.72	1.75	1.41
STANDARD DEVIATION	0.01	0.02	0.02	0.02	0.02

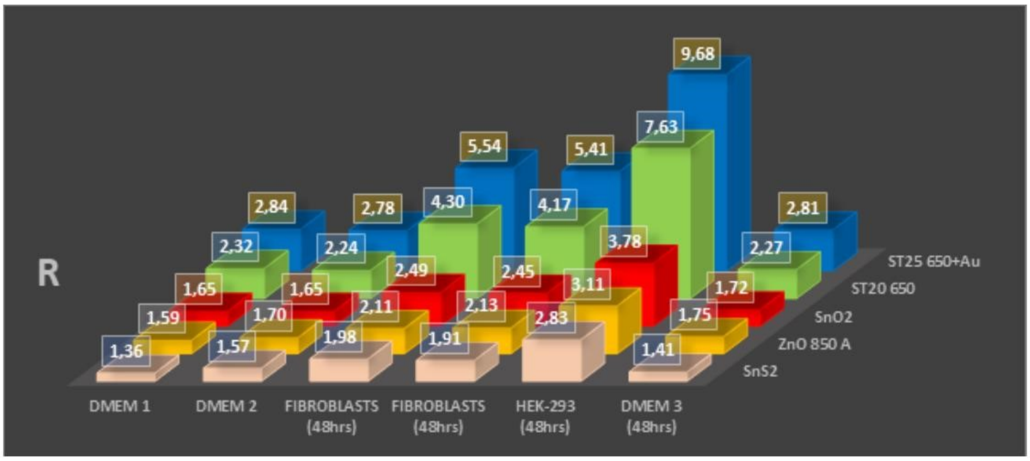

Figure 1. Test results from ST25 650+Au, ST20 650, SnO2, ZnO 850, and SnS2 sensors on the Dulbecco's modified Eagle's medium (DMEM) breeding ground, fibroblasts, and human embryo kidney cell (HEK-293) samples, incubated for the same time (48 h).

Table 4. Data, average values, and standard deviations from cell cultures tests shown in Figure 2A,B.

	ST25 650+Au	ZnO 850 A	WS30 650	ZnO 850 A	W11
CHO (4 h)	11.52	3.03	3.00	2.35	1.70
	11.55	2.98	3.02	2.41	1.88
	11.58	3.02	2.98	2.34	1.53
AVERAGE VALUE	11.55	3.01	3.00	2.37	1.70
STANDARD DEVIATION	0.02	0.02	0.02	0.03	0.14
CHO (7 h)	13.30	3.36	3.15	2.55	1.59
	13.34	3.35	3.11	2.52	1.77
	13.32	3.37	3.13	2.53	1.94
AVERAGE VALUE	13.32	3.36	3.13	2.53	1.77
STANDARD DEVIATION	0.02	0.01	0.02	0.01	0.14
CHO (9 h 30 min)	14.73	3.62	3.28	2.66	1.80
	14.76	3.65	3.33	2.64	1.88
	14.75	3.67	3.25	2.67	1.79
AVERAGE VALUE	14.75	3.65	3.29	2.66	1.82
STANDARD DEVIATION	0.01	0.02	0.03	0.01	0.04
CHO (24 h)	18.56	4.12	3.35	2.73	1.93
	18.58	4.05	3.36	2.71	1.87
	18.53	4.09	3.45	2.80	2.00
AVERAGE VALUE	18.56	4.09	3.39	2.75	1.93
STANDARD DEVIATION	0.02	0.03	0.04	0.04	0.05
CHO (48 h)	20.49	4.27	3.51	3.09	1.95
	20.50	4.24	3.60	3.08	2.04
	20.51	4.30	3.56	3.16	1.97
AVERAGE VALUE	20.50	4.27	3.56	3.11	1.99
STANDARD DEVIATION	0.01	0.02	0.04	0.04	0.04

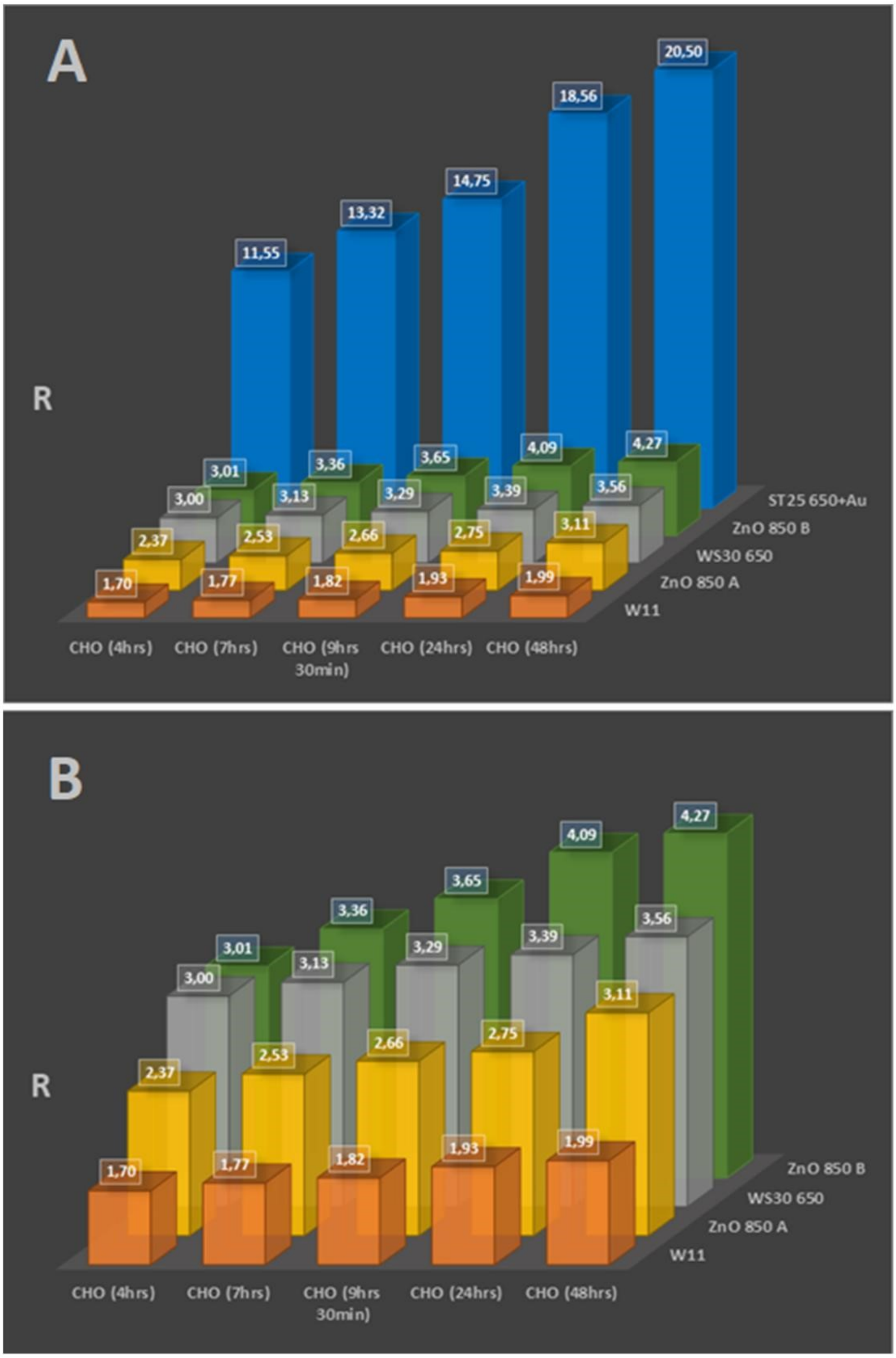

Figure 2. (**A**) Test results from ST25 650+Au, two ZnO 850, WS30 650, and W11 sensors on Chinese hamster ovary (CHO) cell samples incubated at different times. (**B**) A zoom on the previous tests, to better appreciate which sensor responses show trends following the different concentration in the cell cultures, due to their different incubation time.

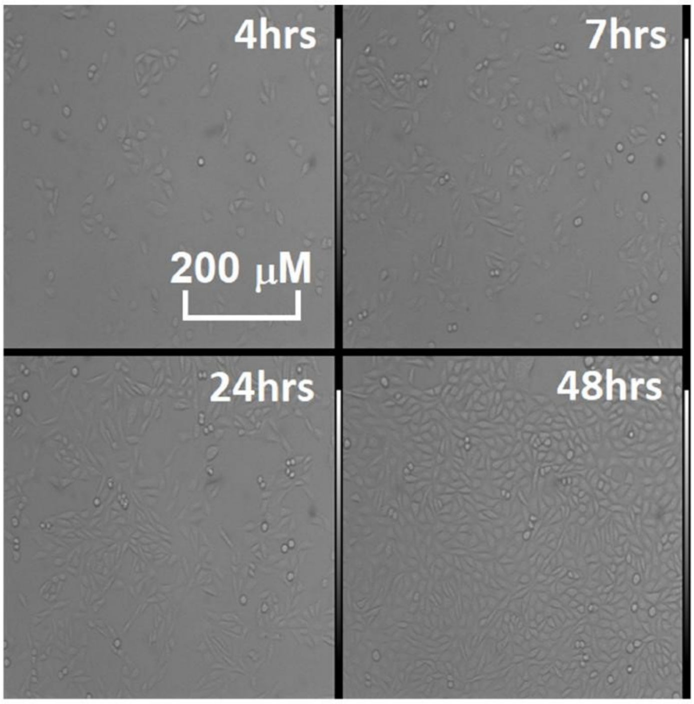

Figure 3. Time lapse of the proliferation in the various CHO cell cultures tested in Figure 2, observed through the optical microscope (model: TE 300, Nikon magnification 10X). The living, plated cells are the elongated semitransparent corpuscles, while the dead ones are the round shapes, floating in the breeding ground.

As in Figure 4, three out of four sensors showed a recognizable trend (highlighted by the labelling—H for healthy samples, T for tumor affected—and the different colors), correlating the amplitude of the response with the markers of oncological interest, even if the responses were quantitatively smaller compared to the cell tests.

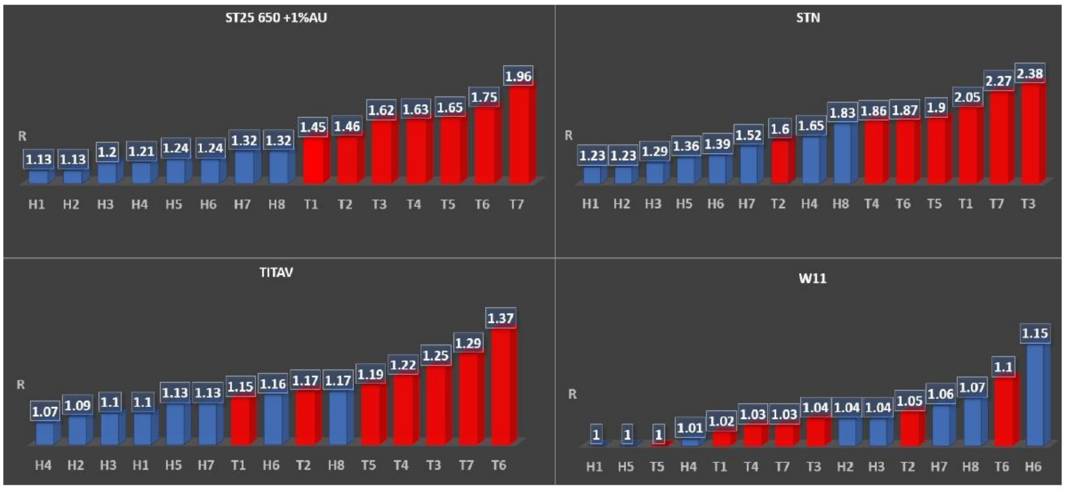

Figure 4. Test results from ST25 650+Au, STN, TiTaV, and W11 on multiple blood samples.

4. Discussion

Overall, the following points have been verified during the cell tests:

(1) (Even if a cell culture biologically does not have a fast metabolism, like fibroblasts, nanostructured sensors can distinguish its activity from the hosting breeding ground.

(2) Immortalized cells have higher responses than normal cells, linked to their faster and erratic metabolism, which ends up generating greater amounts of reactive volatile metabolites, as verified multiple times in the literature [8–22]. This was both observed once all cell cultures were at confluence (filling the hosting Petri dish bottom completely, as shown from the responses in Figure 1 after 48 h of incubation) and during the growth of the culture populations (by comparison of the responses amplitude between Figures 1 and 2, Tables 3 and 4).

(3) The temporal evolution of metabolite production is evident, with contact inhibition (the phenomenon in which cells slow their metabolites once nutrients and space for mitosis in their surroundings starts to run out) starting at around 24 and 48 h passed without cleaning the Petri dishes by changing the breeding ground. This means that it is possible to monitor the evolution of a mass of cells (such as tumors) by studying how many metabolites they have produced over time, and monitor their vitality as well, as highlighted from results on Figure 2A,B when linked to the optical microscope pictures from Figure 3.

Concerning the blood tests, three sensors (TiTaV, STN, and ST25 650+Au) showed good capability to distinguish between healthy and tumor affected donors just from the amplitude of their responses (Figure 4, Tables 5 and 6), even with the incapacity shown in sensors STN and TiTaV to fully distinguish patients T1 and T2 from healthy specimens. This depends on the fact that smaller and less aggressive tumors emanate smaller quantities of different metabolites and VOCs when compared to more aggressive or bigger neoplasms, as was proven in both the histological exam (which confirmed the different size and aggressiveness of the tumoral formations) and by comparison with ST25 650+Au, which instead could distinguish them as the less polluting cancers for the circulatory system by their mere observed responses. This is a huge confirmation of the work carried out on these particular sensors, since those materials were explicitly chosen from the assessments that the team could finalize from previous works [1–7], sealing the reliability of some semiconductors for neoplasms screening in vitro applications.

Table 5. Data, average values, and standard deviations from blood tests on healthy samples shown in Figure 4.

	ST25 650+Au	STN	TiTaV	W11
H1	1.12	1.25	1.10	1.00
	1.15	1.20	1.10	0.99
	1.12	1.24	1.09	1.00
AVERAGE VALUE	1.13	1.23	1.10	1.00
STANDARD DEVIATION	0.01	0.02	0.00	0.00
H2	1.14	1.23	1.11	0.99
	1.15	1.22	1.09	1.05
	1.11	1.24	1.08	1.07
AVERAGE VALUE	1.13	1.23	1.09	1.04
STANDARD DEVIATION	0.02	0.01	0.01	0.03
H3	1.22	1.30	1.12	1.02
	1.19	1.31	1.11	1.02
	1.19	1.27	1.08	1.08
AVERAGE VALUE	1.20	1.29	1.10	1.04
STANDARD DEVIATION	0.01	0.02	0.02	0.03
H4	1.21	1.64	1.09	1.03
	1.23	1.67	1.04	1.01
	1.18	1.65	1.07	1.00
AVERAGE VALUE	1.21	1.65	1.07	1.01
STANDARD DEVIATION	0.02	0.01	0.02	0.01

Table 5. *Cont.*

	ST25 650+Au	**STN**	**TiTaV**	**W11**
H5	1.26	1.38	1.14	0.99
	1.23	1.34	1.13	1.01
	1.22	1.36	1.12	1.01
AVERAGE VALUE	1.24	1.36	1.13	1.00
STANDARD DEVIATION	0.02	0.02	0.01	0.01
H6	1.25	1.40	1.19	1.15
	1.23	1.37	1.14	1.11
	1.23	1.41	1.15	1.20
AVERAGE VALUE	1.24	1.39	1.16	1.15
STANDARD DEVIATION	0.01	0.02	0.02	0.04
H7	1.33	1.52	1.12	1.04
	1.32	1.51	1.15	1.06
	1.30	1.52	1.12	1.07
AVERAGE VALUE	1.32	1.52	1.13	1.06
STANDARD DEVIATION	0.01	0.00	0.01	0.01
H8	1.32	1.85	1.19	1.11
	1.30	1.82	1.15	1.05
	1.34	1.81	1.17	1.05
AVERAGE VALUE	1.32	1.83	1.17	1.07
STANDARD DEVIATION	0.02	0.02	0.02	0.03

Table 6. Data, average values and, standard deviations from blood tests on tumor affected samples shown in Figure 4.

	ST25 650+Au	**STN**	**TiTaV**	**W11**
T1	1.47	2.03	1.13	1.03
	1.43	2.04	1.18	1.04
	1.44	2.07	1.15	0.98
AVERAGE VALUE	1.45	2.05	1.15	1.02
STANDARD DEVIATION	0.02	0.02	0.02	0.03
T2	1.46	1.62	1.18	1.08
	1.46	1.61	1.13	1.02
	1.47	1.58	1.19	1.04
AVERAGE VALUE	1.46	1.60	1.17	1.05
STANDARD DEVIATION	0.00	0.02	0.03	0.02
T3	1.64	2.35	1.26	1.04
	1.62	2.41	1.22	1.06
	1.59	2.38	1.27	1.03
AVERAGE VALUE	1.62	2.38	1.25	1.04
STANDARD DEVIATION	0.02	0.02	0.02	0.01
T4	1.66	1.89	1.20	1.05
	1.60	1.85	1.23	1.03
	1.62	1.84	1.22	1.01
AVERAGE VALUE	1.63	1.86	1.22	1.03
STANDARD DEVIATION	0.02	0.02	0.01	0.02
T5	1.65	1.92	1.20	1.01
	1.66	1.89	1.19	1.03
	1.64	1.90	1.18	0.97
AVERAGE VALUE	1.65	1.90	1.19	1.00
STANDARD DEVIATION	0.01	0.01	0.01	0.02

Table 6. *Cont.*

	ST25 650+Au	STN	TiTaV	W11
	1.76	1.88	1.37	1.09
T6	1.75	1.88	1.38	1.08
	1.73	1.85	1.37	1.13
AVERAGE VALUE	1.75	1.87	1.37	1.10
STANDARD DEVIATION	0.01	0.01	0.00	0.02
	1.96	2.27	1.30	1.02
T7	1.99	2.28	1.27	1.04
	1.94	2.27	1.31	1.02
AVERAGE VALUE	1.96	2.27	1.29	1.03
STANDARD DEVIATION	0.02	0.00	0.02	0.01

5. Conclusions

The study verified the correlation between tumor emanations (due to their internal changes when compared to healthy cells) and chemoresistive sensor responses; their response amplitude followed the grade of degeneration of the neoplasia, both in human blood samples and in the cell culture comparison. In particular:

(1) The ST25 650+Au, ST20 650, ZnO 850, SnO2, and SnS2 sensors showed the capability to differentiate healthy and immortalized cell lines. In particular, the ST25 650+Au and ZnO 850 sensors also proved to be able to discriminate cell culture growth in population over time just from their response amplitude.

(2) The TiTaV, STN, and ST25 650+Au sensors successfully detected the contamination of the blood stream by tumor markers, confirming their reliability after the studies already carried out in the past, showing higher responses with the worsening of the cancer degeneration.

Given these two results, we can conclude that tin and titan oxide semiconductors (and their combinations) have the properties to react successfully to be markers of oncological interest on both biological samples and direct expositions to cell lines, validating their application as fast responding materials for oncological screening purposes.

Our team is now gathering further data, from different cell types and tumor affected patients also, to increase the statistic pool and try PCA and machine learning approaches (as already carried out in previous studies [6,7]) on these new kinds of neoplasm, in order to visualize better defined patterns and program recognition algorithms from the resulting analysis. This comes with the following goals:

(1) To develop a more complete "odor fingerprint database" for tumoral cell lines, and to observe in real time the exhalations of cell metabolites. This will aim to follow cell line vitality while adding drugs for oncological treatment on their breeding ground, thus verifying their effectiveness for pharmacology studies in real time.

(2) To use these arrays as active cores for post-screening devices, aimed at giving fast responses from simple blood sampling for the follow-up of patients that need surgeries to heal from malignant neoplasms, giving physicians new reliable systems with which the existing medical protocols could be integrated.

Further tests will also be carried out on different sensing materials, testing more noble metal decorations in place of gold (like palladium or platinum), as well as different metal and non-metal oxide semiconductors, to verify if more exotic substances could distinguish tumor markers better than tin and titanium oxides.

Author Contributions: Conceptualization, N.L.; methodology, N.L., B.F., G.R., M.V., G.Z. and C.M.; validation, G.A.; formal analysis, N.L. and M.A.; investigation, N.L., G.A., M.A., G.R. and C.M.; resources, G.A.; data curation, N.L.; writing—original draft preparation, N.L.; writing—review and editing, N.L. and C.M.; visualization, N.L.,

G.R., M.V. and G.Z.; supervision, V.G.; project administration, C.M.; funding acquisition, C.M. All authors have read and agreed to the published version of the manuscript.

Funding: This research received no external funding.

Conflicts of Interest: The authors declare no conflict of interest.

References

1. Zonta, G.; Fabbri, B.; Giberti, A.; Guidi, V.; Landini, N.; Malagù, C. Detection of Colorectal Cancer Biomarkers in the Presence of Interfering Gases. *Sens. Actuators B Chem.* **2014**, *87*, 596–599. [CrossRef]
2. Malagù, C.; Fabbri, B.; Gherardi, S.; Giberti, A.; Guidi, V.; Landini, N.; Zonta, G. Chemoresistive Gas Sensors for the Detection of Colorectal Cancer Biomarkers. *Sensors* **2014**, *14*, 18982–18992. [CrossRef] [PubMed]
3. Malagù, C.; Landini, N. Simulation of Intestinal Gaseous Environment in Order to Verify the Capability of Nanostructured Chemoresistive Sensors to Detect Colorectal Tumor Markers (Benzene, 1-Iodo-Nonane, Decanal). *J. Mol. Biomark. Diagn.* **2015**, *2*, 12.
4. Zonta, G.; Anania, G.; Fabbri, B.; Gaiardo, A.; Gherardi, S.; Giberti, A.; Landini, N.; Malagù, C.; Scagliarini, L.; Guidi, V. Preventive screening of colorectal cancer with a device based on chemoresistive sensors. *Sens. Actuators B Chem.* **2017**, *238*, 1098–1101. [CrossRef]
5. Zonta, G.; Anania, G.; Feo, C.; Gaiardo, A.; Gherardi, S.; Giberti, A.; Guidi, V.; Landini, N.; Palmonari, C.; Ricci, L.; et al. Use of gas sensors and FOBT for the early detection of colorectal cancer. *Sens. Actuators B Chem.* **2018**, *262*, 884–891. [CrossRef]
6. Landini, N.; Anania, G.; Fabbri, B.; Gaiardo, A.; Gherardi, S.; Guidi, V.; Rispoli, G.; Scagliarini, L.; Zonta, G.; Malagù, C. Neoplasms and metastasis detection in human blood exhalations with a device composed by nanostructured sensors. *Sens. Actuators B Chem.* **2018**, *271*, 203–214. [CrossRef]
7. Zonta, G.; Anania, G.; Astolfi, M.; Feo, C.; Gaiardo, A.; Gherardi, S.; Giberti, A.; Guidi, V.; Landini, N.; Palmonari, C.; et al. Chemoresistive sensors for colorectal cancer preventive screening through fecal odor: Double-blind approach. *Sens. Actuators B Chem.* **2019**, *301*, 127062. [CrossRef]
8. Cairns, R.A.; Harris, I.S.; Mak, T.W. Regulation of cancer cell metabolism. *Nat. Rev. Cancer* **2011**, *11*, 85–95. [CrossRef]
9. Qiu, Y.; Cai, G.; Su, M.; Chen, T.; Zheng, X.; Xu, Y.; Ni, Y.; Zhao, A.; Xu, L.; Cai, S. Serum Metabolite Profiling of Human Colorectal Cancer Using GC−TOFMS and UPLC−QTOFMS. *J. Proteome Res.* **2009**, *8*, 4844–4850. [CrossRef]
10. Chan, E.C.Y.; Koh, P.K.; Mal, M.; Cheah, P.Y.; Eu, K.W.; Backshall, A.; Cavill, R.; Nicholson, J.K.; Keun, H.C. Metabolic Profiling of Human Colorectal Cancer Using High-Resolution Magic Angle Spinning Nuclear Magnetic Resonance (HR-MAS NMR) Spectroscopy and Gas Chromatography Mass Spectrometry (GC/MS). *J. Proteome Res.* **2009**, *8*, 352–361. [CrossRef]
11. Phillips, M.; Gleeson, K.; Hughes, J.M.B.; Greenberg, J.; Cataneo, R.N.; Baker, L.; McVay, P. Volatile organic compounds in breath as markers of lung cancer: A cross-sectional study. *Lancet* **1999**, *353*, 1930–1933. [CrossRef]
12. Probert, C.S.J.; Ahmed, I.; Khalid, T.; Johnson, E.; Smith, S.; Ratcliffe, N. Volatile Organic Compounds as Diagnostic Biomarkers in Gastrointestinal and Liver Diseases. *J. Gastrointestin. Liver Dis.* **2009**, *18*, 337–343. [PubMed]
13. Altomare, D.F.; Di Lena, M.; Porcelli, F.; Trizio, L.; Travaglio, E.; Tutino, M.; Dragonieri, S.; Memeo, V.; de Gennaro, G. Exhaled volatile organic compounds identify patients with colorectal cancer. *Br. J. Surg.* **2013**, *100*, 144–150. [CrossRef] [PubMed]
14. Takano, S.; Yoshii, Y.; Kondo, S.; Suzuki, H.; Maruno, T.; Shirai, S.; Nose, T. Concentration of Vascular Endothelial Growth Factor in the Serum and Tumor Tissue of Brain Tumor Patients. *Cancer Res.* **1996**, *56*, 2185–2190.
15. Tamura, M.; Ohta, Y.; Kajita, T.; Kimura, K.; Go, T.; Oda, M.; Nakamura, H.; Watanabe, G. Plasma VEGF concentration can predict the tumor angiogenic capacity in non-small cell lung cancer. *Oncol. Rep.* **2001**, *8*, 1097–1102. [CrossRef]
16. Werther, K.; Christensen, I.J.; Brünner, N.; Nielsen, H.J. Soluble vascular endothelial growth factor levels in patients with primary colorectal carcinoma. The Danish RANX05 Colorectal Cancer Study Group. *Eur. J. Surg. Oncol.* **2000**, *26*, 657–662. [CrossRef]

17. Ellis, L.M.; Takahashi, Y.; Liu, W.; Shaheen, R.M. Vascular endothelial growth factor in human colon cancer: Biology and therapeutic implications. *Oncologist* **2000**, *5*, 11–15. [CrossRef]
18. Cohen, S.J.; Punt, C.J.; Iannotti, N.; Saidman, B.H.; Sabbath, K.D.; Gabrail, N.Y.; Picus, J.; Morse, M.; Mitchell, E.; Miller, M.C.; et al. Relationship of Circulating Tumor Cells to Tumor Response, Progression-Free Survival, and Overall Survival in Patients with Metastatic Colorectal Cancer. *J. Clin. Oncol.* **2008**, *26*, 3213–3221. [CrossRef]
19. Riethdorf, S.; Fritsche, H.; Müller, V.; Rau, T.; Schindlbeck, C.; Rack, B.; Janni, W.; Coith, C.; Beck, K.; Jänicke, F.; et al. Detection of Circulating Tumor Cells in Peripheral Blood of Patients with Metastatic Breast Cancer: A Validation Study of the CellSearch System. *Clin. Cancer Res.* **2007**, *13*, 920–928. [CrossRef]
20. Allard, W.J.; Matera, J.; Miller, M.C.; Repollet, M.; Connelly, M.C.; Rao, C.; Tibbe, A.; Uhr, J.; Terstappen, L. Tumor Cells Circulate in the Peripheral Blood of All Major Carcinomas but not in Healthy Subjects or Patients with Nonmalignant Diseases. *Clin. Cancer Res.* **2004**, *10*, 6897–6904. [CrossRef]
21. Tothill, I.E. Biosensors for cancer markers diagnosis. *Semin. Cell Dev. Biol.* **2009**, *20*, 55–62. [CrossRef] [PubMed]
22. Zheng, G.; Patolsky, F.; Cui, Y.; Wang, W.U.; Lieber, C.M. Multiplexed electrical detection of cancer markers with nanowire sensor arrays. *Nat. Biotechnol.* **2005**, *23*, 1294–1301. [CrossRef] [PubMed]
23. Wilson, M.S. Electrochemical Immunosensors for the Simultaneous Detection of Two Tumor Markers. *Anal. Chem.* **2005**, *77*, 1496–1502. [CrossRef] [PubMed]
24. Wang, J. Electrochemical biosensors: Towards point-of-care cancer diagnostics. *Biosens. Bioelectron.* **2006**, *21*, 1887–1892. [CrossRef] [PubMed]
25. Choi, Y.-E.; Kwak, J.-W.; Park, J.W. Nanotechnology for Early Cancer Detection. *Sensors* **2010**, *10*, 428–455. [CrossRef]
26. Penner, R.M. Chemical Sensing with Nanowires. *Annu. Rev. Anal. Chem.* **2012**, *5*, 461–485. [CrossRef]
27. Krishnamoorthy, S. Nanostructured sensors for biomedical applications—A current perspective. *Curr. Opin. Biotechnol.* **2015**, *34*, 118–124. [CrossRef]
28. DIN EN ISO 14820-2 Fertilizers and Liming Materials—Sampling and Sample Preparation—Part 2: Sample Preparation (ISO 14820-2:2016). German and English Version prEN ISO 14820-2:2018. Available online: https://www.en-standard.eu/csn-en-14820-single-use-containers-for-human-venous-blood-specimen-collection/?gclid=EAIaIQobChMIsr2dx5HS1wIVbSjTCh0kAQuPEAAYASAAEgKL4fD_BwE (accessed on 26 January 2020).
29. DIN EN ISO 6710:2016-11—Entwurf. Available online: https://www.beuth.de/de/norm-entwurf/din-en-iso-6710/261188601 (accessed on 26 January 2020).
30. Goossens, W.; Van Duppen, V.; Verwilghen, R.L. K2-or K3-EDTA: The anticoagulant of choice in routine haematology? *Clin. Lab. Haematol.* **1991**, *13*, 291–295. [CrossRef]
31. Van Cott, E.M.; Lewandrowski, K.B.; Patel, S.D.; Grzybek, Y.; Patel, H.S.; Fletcher, S.R.; Kratz, A. Comparison of glass K3EDTA versus plastic K2EDTA blood-drawing tubes for complete blood counts, reticulocyte counts, and white blood cell differentials. *Lab. Hematol.* **2003**, *9*, 10–14.
32. Patel, N. Why Is EDTA the Anticoagulant of Choice for Hematology Use? Available online: https://www.researchgate.net/file.PostFileLoader.html?id=55d494855cd9e392178b45dd&assetKey=AS%3A273835104899073%401442298784205 (accessed on 26 January 2020).
33. Malagù, C. Model for Schottky barrier and surface states in nanostructured n-type semiconductors. *J. Appl. Phys.* **2002**, *91*, 808. [CrossRef]
34. Guidi, V.; Blo, M.; Butturi, M.A.; Carotta, M.C.; Galliera, S.; Giberti, A.; Malagù, C.; Martinelli, G.; Piga, M.; Sacerdoti, M.; et al. Aqueous and alcoholic syntheses of tungsten trioxide powders for NO_2 detection. *Sens. Actuators B Chem.* **2004**, *100*, 277–282. [CrossRef]
35. Carotta, M.C.; Guidi, V.; Malagù, C.; Vendemiati, B.; Zanni, A.; Martinelli, G.; Sacerdoti, M.; Licoccia, S.; DiVona, M.; Traversa, E. Vanadium and tantalum-doped titanium oxide (TiTaV): A novel material for gas sensing. *Sens. Actuators B Chem.* **2005**, *108*, 89–96. [CrossRef]
36. Carotta, M.C.; Gherardi, S.; Guidi, V.; Malagù, C.; Martinelli, G.; Vendemiati, B.; Sacerdoti, M.; Ghiotti, G.; Morandi, S.; Bismuto, A.; et al. (Ti, Sn)O2 binary solid solutions for gas sensing: Spectroscopic, optical and transport properties. *Sens. Actuators B Chem.* **2008**, *130*, 38–45. [CrossRef]
37. Carotta, M.C.; Cervi, A.; Giberti, A.; Guidi, V.; Malagù, C.; Martinelli, G.; Puzzovio, D. Metal–oxide solid solutions for light alkane sensing. *Sens. Actuators B Chem.* **2008**, *133*, 516–520. [CrossRef]

38. Carotta, M.C.; Cervi, A.; Gherardi, S.; Guidi, V.; Malagù, C.; Martinelli, G.; Vendemiati, B.; Sacerdoti, M.; Ghiotti, G.; Morandi, S.; et al. (Ti, Sn)O2 solid solutions for gas sensing: A systematic approach by different techniques for different calcination temperature and molar composition. *Sens Actuators B Chem.* **2009**, *139*, 329–339. [CrossRef]
39. Carotta, M.C.; Benetti, M.; Guidi, V.; Gherardi, S.; Malagu', C.; Vendemiati, B.; Martinelli, G. Nanostructured (Sn, Ti, Nb)O2 Solid Solution for Hydrogen Sensing. *MRS Online Proc. Libr. Arch.* **2006**, *915*. [CrossRef]
40. Guidi, V.; Carotta, M.C.; Fabbri, B.; Gherardi, S.; Giberti, A.; Malagù, C. Array of sensors for detection of gaseous malodors in organic decomposition products. *Sens. Actuators B Chem.* **2012**, *174*, 349–354. [CrossRef]
41. Carotta, M.C.; Cervi, A.; di Natale, V.; Gherardi, S.; Giberti, A.; Guidi, V.; Puzzovio, D.; Vendemiati, B.; Martinelli, G.; Sacerdoti, M.; et al. ZnO gas sensors: A comparison between nanoparticles and nanotetrapods-based thick films. *Sens. Actuators B Chem.* **2009**, *137*, 164–169. [CrossRef]
42. Gaiardo, A.; Fabbri, B.; Guidi, V.; Bellutti, P.; Giberti, A.; Gherardi, S.; Vanzetti, L.; Malagù, C.; Zonta, G. Metal Sulfides as Sensing Materials for Chemoresistive Gas Sensors. *Sensors* **2016**, *16*, 296. [CrossRef]
43. Guidi, V.; Malagù, C.; Carotta, M.C.; Vendemiati, B. Printed Films: Materials Science and Applications in Sensors, Electronics and Photonics. In *Woodhead Publishing Series in Electronic and Optical Materials*, 1st ed.; Prudenziati, M., Hormadaly, J., Eds.; Woodhead Publishing: Cambridge, UK, 2012; pp. 278–334.
44. Carotta, M.C.; Gherardi, S.; Malagù, C.; Nagliati, M.; Vendemiati, B.; Martinelli, G.; Sacerdoti, M.; Lesci, I.G. Comparison between titania thick films obtained through sol–gel and hydrothermal synthetic processes. *Sens Actuators B Chem.* **2007**, *515*, 8339–8344. [CrossRef]
45. Giberti, A.; Benetti, M.; Carotta, M.C.; Guidi, V.; Malagù, C.; Martinelli, G. Heat exchange and temperature calculation in thick-film semiconductor gas sensor systems. *Sens. Actuators B Chem.* **2008**, *130*, 277–280. [CrossRef]

4.5 Humidity tests on Tin and Tin-Titanium and Niobium Oxide based sensors

Materials Science and Engineering B 265 (2021) 115013

Contents lists available at ScienceDirect

Materials Science & Engineering B

journal homepage: www.elsevier.com/locate/mseb

Humidity effects on SnO_2 and $(SnTiNb)O_2$ sensors response to CO and two-dimensional calibration treatment

S. Gherardi [b,*], G. Zonta [a], M. Astolfi [a], C. Malagù [a]

[a] Department of Physics and Earth Sciences, University of Ferrara, Via Saragat 1, 44122 Ferrara, Italy
[b] SCENT S.r.l., Via Quadrifoglio 11, 44124 Ferrara, Italy

ARTICLE INFO

Keywords:
MOX sensors
Chemoresistive sensors
Nanomaterials
SnO2
STN
Humidity

ABSTRACT

Humidity is always present in real applications of semiconductor gas sensors, e.g. in the environmental monitoring or medical applications, therefore it is important to study the effects that water vapor has on sensors conduction. This work is a study of the humidity role in the conduction mechanisms of two sensor materials: tin oxide (SnO_2) and a mixture of tin, titanium and niobium oxide (STN), showing the property of the second of being less affected by humidity, therefore useful in medical and environmental applications. Laboratory and on-field tests have been performed with water vapor and CO, at different concentration, initial conditions and partial pressures, both singularly and in combination. A novel concept of sensitivity is introduced in this work, called two-dimensional sensitivity, which not only quantifies the dependence of sensors response on the concentration of the analyte, but also on the variation of humidity and their non-linear combination. By taking the partial derivative of the fitting function with respect to CO concentration, it is possible to gather not only information about the dependence of the signal variation on the gas concentration, but also how it is influenced by water vapour, even when the water vapor partial pressure is kept constant, and vice versa.

1. Introduction

It is well known that humidity is a universal interfering gas for most of the metal-oxide (MOX) sensors. The adsorption and hydration of water from air onto an oxide is an unavoidable fact, unless the oxide is heated to a high temperature [1]. Moreover, water can have strong effects if the oxide is employed as a gas sensor. A hydroxylated surface is formed when OH^- ions are attracted by the oxide cations and viceversa for H^+ ions that are attracted by anions. The effect of chemisorbed air is to neutralize those sites with a strong electrostatic attraction for ions. On the other hand, water can also be physisorbed and it requires lower temperatures to be removed due to the weak attraction. When water is present, it acts as a donor, giving electrons to the metal-oxide semiconductor, therefore the adsorption of oxygen (as O_2^- or O^- species) becomes weaker. Both these phenomena contribute to an enhanced conductivity of the material in air, besides, the sensitivity to hydrocarbons is often (even not always) suppressed [2]. In a lot of gas sensors applications water vapor plays a fundamental role, e.g. environmental monitoring [3], agricultural applications [4] and medical field [5–11], and it is impossible to avoid its presence, therefore it is also important to understand the phenomena and the role of water in sensing mechanisms. A lot of works in the sensor field relies on humidity detection [12–14] and the research of a material not affected by humidity is already a primary challenge. In this work, the effects of adsorbed water on conductivity and on carbon monoxide detection have been investigated for two different MOX materials: tin oxide (SnO_2) and a mixture of tin, titanium and niobium oxide (STN). It is well known that the most important interfering gas for MOX sensors is the water vapour and finding a material not affected by humidity could be crucial to perform especially environmental [15] or medical applications [6]. STN studied here showed to be a good candidate for this purpose. We also introduce here a novel concept of sensitivity: which will be called bidimensional sensitivity, which not only quantifies the dependence of sensors response on the concentration of analyte, but also on the variation of humidity and their non-linear combination. Experimental begins with the analysis of non-dehydrated surface conductance in dry air versus CO response correlation in laboratory-controlled conditions. After that, other tests have been performed in a real environmental situation (field), passing through a whole range of working temperatures (from 100 to 700 °C), showing how a short high temperature heating can remove the adsorbed humidity.

---

[*] Corresponding author.
E-mail address: ghrsdr@unife.it (S. Gherardi).

https://doi.org/10.1016/j.mseb.2020.115013
Received 2 September 2020; Received in revised form 19 November 2020; Accepted 14 December 2020
0921-5107/

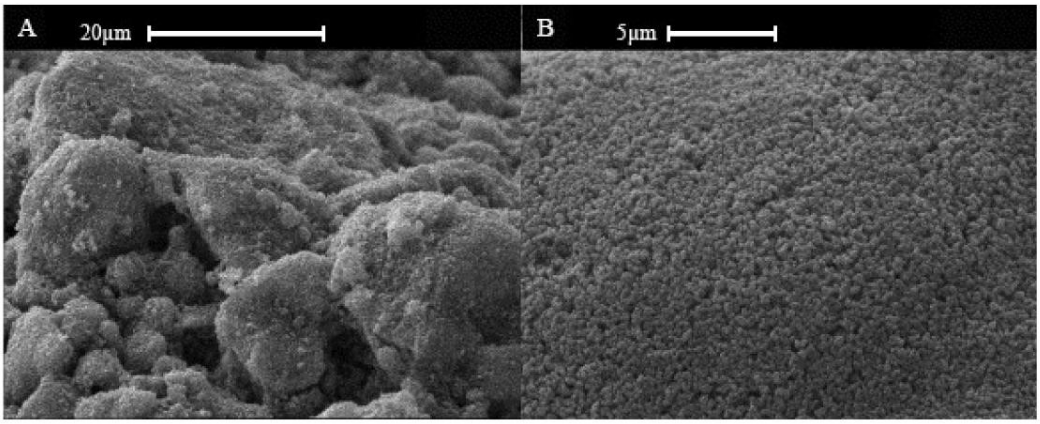

Fig. 1. A) STN 850x1 structure at × 2 K; B) SnO 2 850x1 structure at × 5 K.

2. Material and methods

2.1. Sensors synthesis and film deposition

In this work, two types of semiconductor materials have been studied: SnO_2 and STN. Both of the sensor films have been deposited by screen-printing technique, that is largely employed because of its low cost and fast preparation time [16]. Preparation of STN has been performed by inserting Nb(V) in $(Sn_{0.7}T_{0.3})O_2$ solution via sol-gel technique [17] by dropping $NbBr_5$, previously dissolved in a methanol solution: stoichiometric solutions of their metal-alkoxides precursors (Sn(II)-ethylhexanoate 95% Aldrich, Ti-butoxide 97% Aldrich used without further purification) were employed and then the entire process was carried out by maintaining the solution under gentle stirring.

Diluted HNO_3 assisted the hydrolysis of all the starting materials, resulting in a pale yellow colloidal precursor that, after filtration and subsequent calcination (at 550 °C in a muffle oven for 2 h in dry air), the result of the whole process was 84.5% of pure white (Sn0.7Ti0.3)O_2, hereinafter labelled ST30. Insertion of foreign Nb(V) in ST30 was possible also via sol–gel, dropping NbBr5 (98% Aldrich, Sn:Nb = 20:1), previously dissolved in minimal amount of methanol, to the Sn(II)-Ti (IV) stoichiometric solution. At the end of this process, the pure (Sn, Ti, Nb)O_2, also named STN [18] was obtained.

SnO_2 has been synthesized through a sol–gel route involving Sn(II)-alkoxide dissolved in n-butanol and hydrolyzed by an acidic solution, whose pH is 0.8. By means of calcination, carried out at 550 °C for 2 h, the hydroxyl-precursor has been decomposed into pure and partially crystalline cassiterite (rutile-like structure), as confirmed by XRD analysis [15].

Fig. 1 shows respectively STN (A) and SnO_2 (B) nanostructures SEM images. The two materials show nanograins with an average dimension of about 80 nm and 40 nm respectively.

2.2. Experimental set-up

Sensors behaviour has been studied under controlled conditions of temperature, air-flow and gas concentration, by housing them in a hermetically sealed chamber (Fig. S1 in supplementary materials) made of aluminium that hosts a temperature and humidity sensor. The technical gases from the bottles are uniformly diffused from the chamber base. Different humidity conditions have been supplied to the chamber thanks to a glass bubbler in which different flows were insuffled. The temperature in the sensors housing was maintained constant (at 36 °C) by inserting the whole apparatus in a climatic chamber. Gas concentrations are calibrated thanks to mass-flow controllers and a specific software and conveyed to the chamber by means of Teflon pipelines.

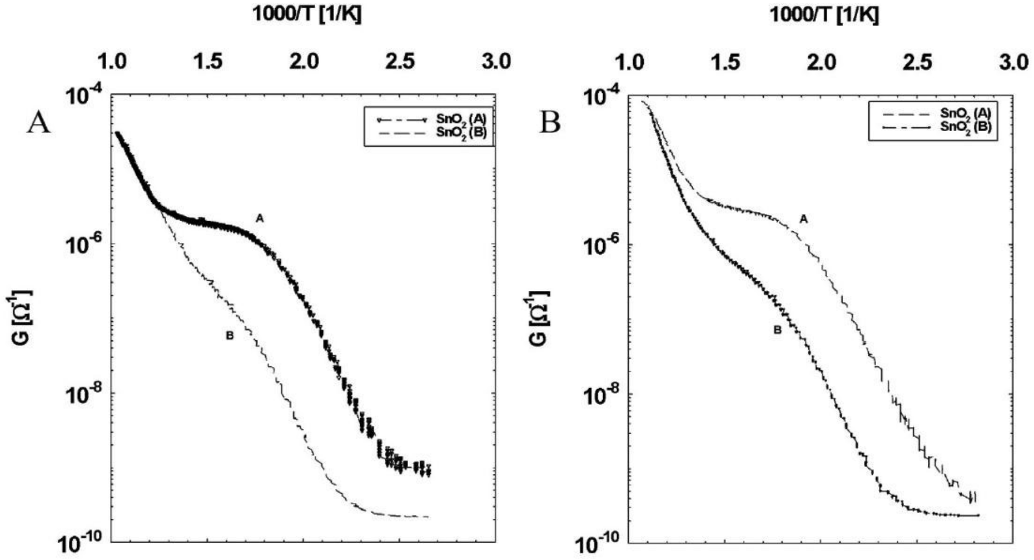

Fig. 2. Arrhenius plot A) taken after 12 h at 450 °C in static environmental air with two SnO_2.

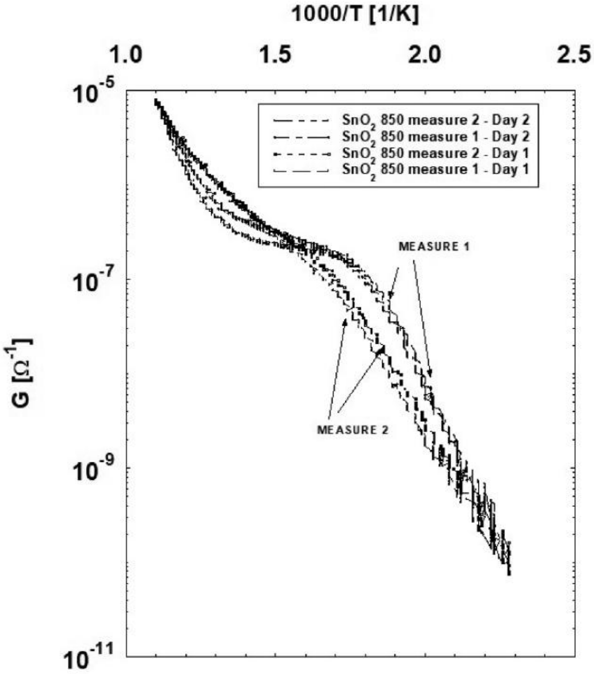

Fig. 3. Repetition of the previous measurements (Fig. 3) in two different days.

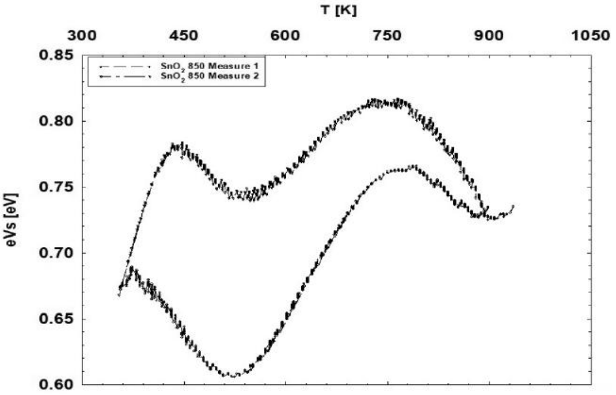

Fig. 4. Potential barriers calculated using the "temperature-stimulated conductance.

3. Experimental

Chemisorbed species on semiconductor layers are responsible for the mechanisms of trapping and/or transferring electronic carriers to the underlying oxide, modifying its electrical properties. In particular, chemisorbed oxygen in the form of anions (O^- and O_2^-) plays an essential role in the sensing mechanism, by modulating the interactions with target gases [19]. These gases are generally reducing, like hydrocarbons or, specifically for our purposes, CO. Arrhenius plot [20] is one of the most important methods to investigate the behaviour of semiconductor oxide sensors in air, therefore, it has been employed in this study to understand the interactions occurring by adsorbed/chemisorbed oxygen and water species. In particular, repeated Arrhenius plots have been performed sequentially or after different preliminary heating of sensors in dry air, aiming to desorb humidity and to compare them among each other.

In Fig. 2 some comparisons of various SnO_2 Arrhenius plots performed in synthetic dry air flow, starting from two different initial conditions: Arrhenius A) after 12 h at 450 °C in static environmental air; Arrhenius B) after the previous measurement and after 2 h at 450 °C in continuous dry air flow.

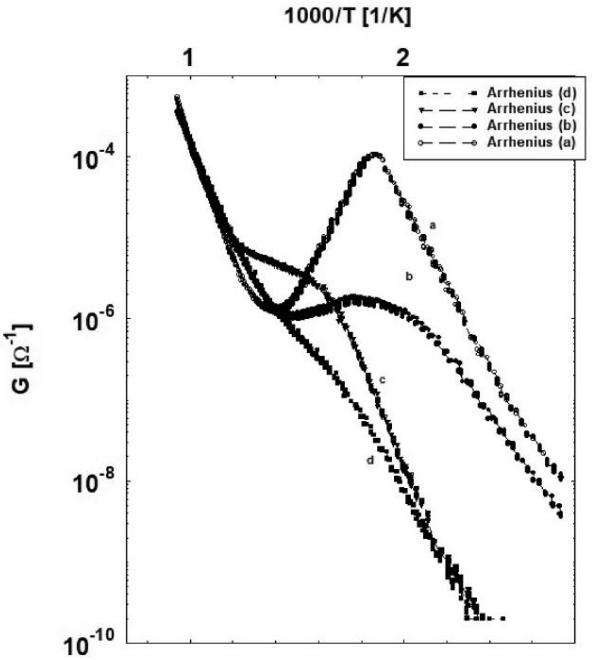

Fig. 5. Arrhenius plots in different sensor initial conditions: (a) heated at 100 °C and in dry air for ten minutes before the measurement at the same conditions as point (b) after being at room temperature for 24 h; (c) heated at 450 °C and in dry air for 10 min before the measurement; (d) heated at 700 °C and in dry air for 10 min before the measurement.

As shown in Fig. 2, the first Arrhenius curve (SnO_2 A for both figures) starts with a higher conductance value for the total temperature range except for the last part of the curve (at higher T), in which it assumes the same values of the second one (SnO_2 Arrhenius B). This behaviour can be due to the presence of water species, that act as donors, chemisorbed on the sensor surface during the environmental air period, in the condition A. In order to show the repeatability of this phenomenon, both the previous measurements have been repeated in two different days (after sensors being stored in the chamber at 300 °C and in dry air for 15 h) as the Fig. 3 displays. Potential barriers (shown in Fig. 4) have been calculated using the "temperature-stimulated conductance measurements" method [20] and derived from Arrhenius plot of Fig. 2.

From the previous charts we have seen that, at temperatures of about 800 K, the conductance curves overlap, for this reason different new Arrhenius plots have been serially performed, starting from different initial conditions as shown in Fig. 5, where all the curves are referred to the same SnO_2 sensor:

(a) heated at 100 °C and in dry air for ten minutes before the measurement;
(b) at the same conditions as point (a) after being at room temperature for 24 h;
(c) heated at 450 °C and in dry air for 10 min before the measurement;
(d) heated at 700 °C and in dry air for 10 min before the measurement.

Starting from (a) to (d), a progressive flattening of the curve shapes is noticeable, and also a conductance decrease at low to medium temperatures range. This can be due to the progressive desorption of the hydroxylated species, along with increasing initial sensor temperatures. Taking this in count, Arrhenius plots were performed and compared with each other, after having performed another Arrhenius before them

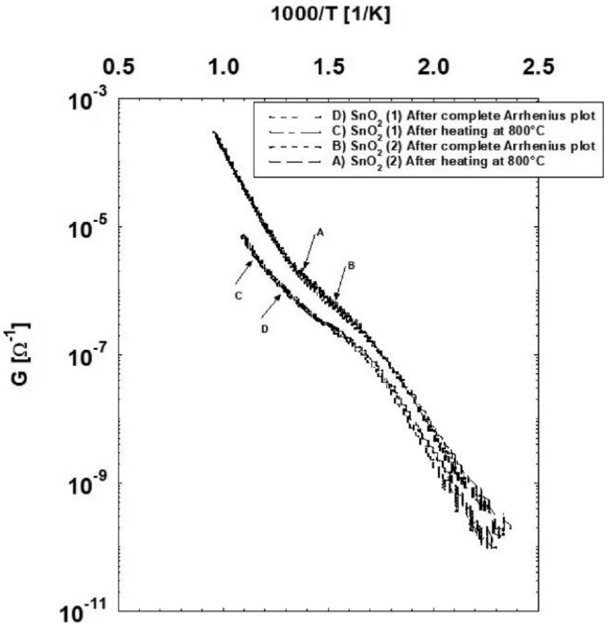

Fig. 6. Comparison among Arrhenius plots for the two sensors: A) B) first Arrhenius and C) D) after a heat at 700 °C. Both measurements were taken in synthetic dry air for 10 min and both starting after 12 h in environmental air and at room temperature.

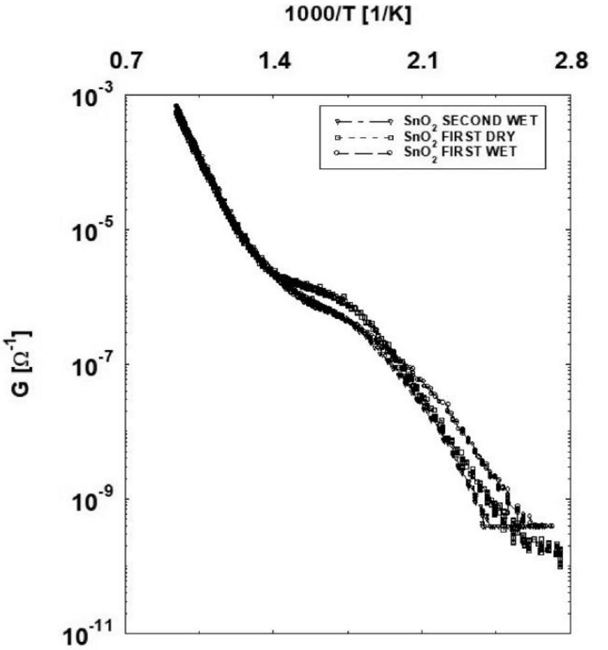

Fig. 7. Arrhenius plots in wet (20%) air compared with dry air ones, performed without conditioning not to enhance water species desorption.

and after having heated sensors at 700 °C, both in synthetic dry air-flow for 10 min and both starting after 12 h in environmental air and room temperature. Comparison between those is shown in Fig. 6.

Finally, in Fig. 7, Arrhenius plots in wet (20%RH at 38 °C) air conditions have been carried out and compared with dry air ones, performed without conditioning to not enhance water species desorption. It is clear by observing the figures that sequential Arrhenius plots do not significantly differ from each other like dry air ones and they also are similar to the one without any preliminary conditioning.

This confirms that the surface barrier and, consequently, the conductance in stimulated temperature is strongly affected by adsorbed/chemisorbed water species on the sensor surface.

Different is the case of STN material, that shows a very reduced discrepancy between Arrhenius plot shapes performed one after the other or after preliminary conditioning in dry or wet conditions.

Fig. 8 shows both dry and wet Arrhenius plots starting at different initial conditions depending on the voltage given to the heater: A) 1 V (373 K), B) 5 V (723 K) and C) 7 V (923 K) respectively for 10 min before the measurement. What emerges is that this material experiments a very little interaction with humidity, showing good overlap between dry and wet plots. In Fig. 9 dry and wet Arrhenius plots are shown for two different STN sensors of the same type and this case is representative of a good reproducibility of the material.

Since Arrhenius plots of different percentage of titania-tin based sensors and STN (solid solution of tin and titanium oxides with addition of niobium) sensors exhibit a similar shape, it is possible to assert that even if niobium is introduced in the crystal lattice of a binary solid solution of tin and titanium, the shape of the conductance vs temperature curve is still typical of the TiO_2 films rather than that of the SnO_2 ones. The extra valence of Ni with respect to Ti is greatly effective only in increasing electrical conductance [15].

Other studies highlight a lower conductivity of TiO_2 (and Sn-Ti) based sensors that also have a higher thermodynamic stability and less cross-sensitivity to humidity than SnO_2 [21], this due to a series of different mechanisms in H_2O adsorption between the two materials [22].

Field measurements in a traffic busy area (city of Ferrara, Italy) have been performed using a portable monitoring unit (Fig. S2 in supplementary materials) equipped with SnO_2 and STN MOX sensors and air flux in the monitoring unit was gently recycled by a fan.

Results have been compared with carbon monoxide environmental emissions measured with a certified FTIR analyzer. Response is calculated as $R = \frac{\Delta G}{G_{air}}$, while $\Delta G = G - G_{air}$, where G_{air} is the conductance of the sensor in air and G the conductance with the presence of the analyte. It can clearly be noticed the lower interference of water vapour on the response to CO that characterizes the STN sensor with respect to SnO_2 one. Figs. 10 and 11 show SnO_2 correlation with water vapour (absolute humidity, AH) [KPa]and with CO [mg/m^3] respectively: water adsorption strongly competes with CO detection and its correlation with the sensor response is greater than that of the target gas ($r^2 = 0.29$ for response-CO correlation, $r^2 = 0.76$ for response-water correlation). On the other hand (Figs. 12 and 13), STN exhibits a stronger correlation ($r^2 = 0.89$) with CO and a weak correlation ($r^2 = 0.25$) with water vapour. SnO_2 and STN sensors were at their best working temperature for CO detection, 350 °C and 450 °C respectively. These values were chosen after controlled temperature tests at fixed CO concentration, resulting the once enhancing CO response. In Figs. 14 and 15 the temperature dependence of the response to fixed CO concentration was shown for the two materials employed, in order to evaluate the best sensitivity of both the sensors to the target gas and to identify Tbest, temperature at which the sensor gives its best response.

Figs. 16–18 represent the time trend of the carbon monoxide concentration measured with FTIR (Fourier Transform Infrared) analyzer compared with the trend of the SnO_2 response and STN response respectively. In particular, SnO_2 shape correlates better with CO, especially when the gas is present at higher concentrations, other higher peaks of the SnO_2 are strongly affected by the humidity amount as Fig. 17 confirms.

To confirm previous evidence, two identical systems (one in forced air flux passing through an active carbon filter, the other without) were paired for field measurements. The filter was employed in order to strongly reduce humidity. In each system, a pair of identical SnO_2 and STN sensors was placed to state their behaviour in different humidity conditions. As shown in Fig. 19, both responses of the two STN sensor

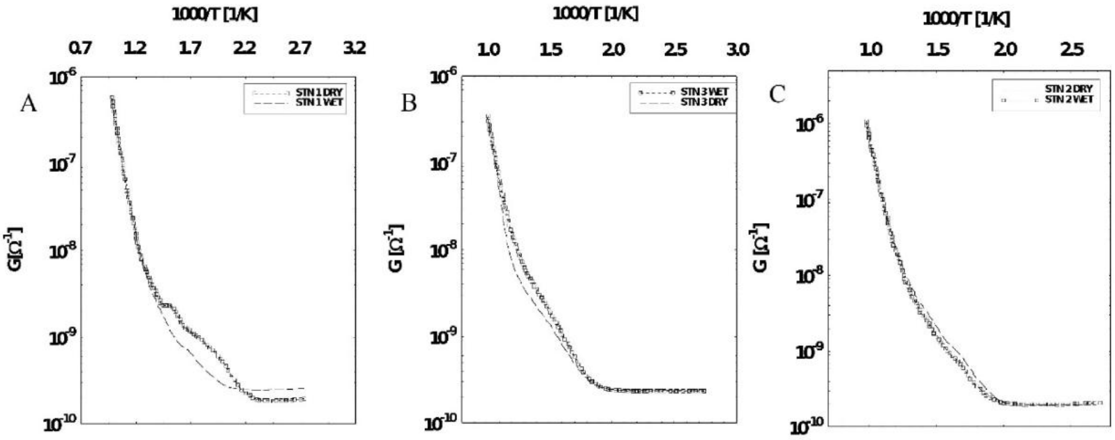

Fig. 8. A: DRY/WET Arrhenius plot comparison between same STN sensor with no preliminary heating (starting at 1 V). B: DRY/WET Arrhenius plot comparison between same STN sensor conditioned at 5 V. C: DRY/WET Arrhenius plot comparison between same STN sensor conditioned at 7 V.

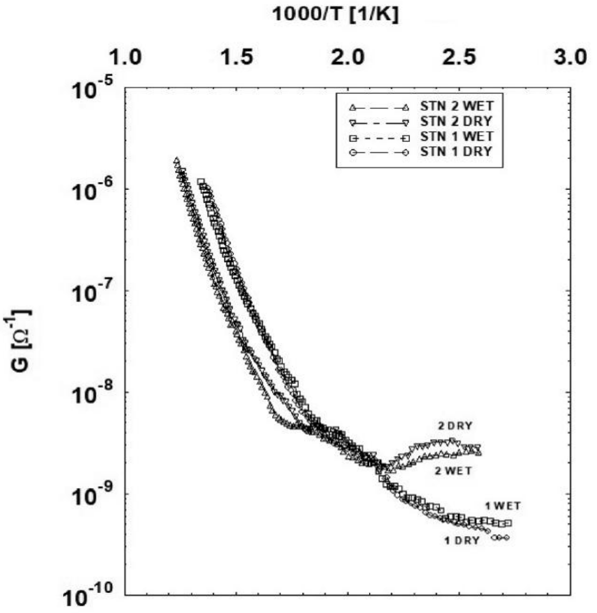

Fig. 9. Comparison among DRY/WET Arrhenius plot for two different STN sensors of the same type.

are very similar to each other, showing the property of this material of being not so much affected by humidity and in good agreement with CO curve shape. Instead, in Fig. 20 it is evident that SnO_2 response is strongly modified by the presence of filter with respect to the other one.

We assume that, if separately injected, different concentrations of humidity and CO affect the sensors conductance following these equations: $G_{H2O} = a + bp^{\alpha}_{H2O}$ and $G_{CO} = c + d[CO]^{\gamma}$ [23], where the coefficients a, b, c, d, α, γ are constants, following the models proposed in [24]. Therefore, the combined analysis of both humidity and analyte gas, naturally leads to a two-dimensional mathematical approach to the data, from which it is possible to derive more information than from the usual calibration curves. Taking into account that if CO is injected at different water vapour pressures, c and d become dependent on the quantity p_{H2O}. Otherwise, experimental laboratory measurements show that α and γ remain nearly constant (less than 3% of fluctuation) at all the p_{H2O} values treated. By combining previous hypothesis and considering the non-trivial additivity of the two causes, it is possible to derive the following function ($\mathbb{R}^2 \rightarrow \mathbb{R}$) for the conductance dependence on the two gas concentrations:

$$G_{pH2O,[CO]} = G_0 + A\cdot p^{\alpha}_{H2O} + B\cdot[CO]^{\gamma} + C\cdot p^{\alpha}_{H2O}\cdot[CO]^{\gamma} \tag{1}$$

In this formula, G_0 represents the sensor conductance in absence of both CO and humidity and the constant terms A, B, C, α, γ can be derived from a fit of the experimental values [15]. In order realize this surface, various concentrations of CO have been injected in the sensors chamber at different humidity values, calculating the response *R* as already defined in this section. The analytical expression (1) leads to a surface obtained by fitting experimental values of R with the generic expression $z = a + bx^c + dy^e + fx^c y^e$, the results are shown in Fig. 21.

Fig. 21A brings back to the strong mutual interaction between humidity and CO, showing a decrease in the SnO_2 response to CO in presence of higher water vapor pressures. We denoted that for the STN sensor, humidity affects the response to CO significantly only up to 15% and so, for this reason the humidity ranges for SnO_2 and STN are different. It can be noticed that for SnO_2, the response to CO is strongly different for low (0 – 5%) and high (30–45%) humidity levels and the shape of the curves R vs CO show a non-monotonic trend (with a slope inversion at 10 – 15% of RH). In the case of STN the variation of R to CO with humidity is strongly lower and it becomes less evident after 10 – 15% of RH. Same calculations have been performed for experimental field measurements, as summarized in Fig. 22.

Differences on the constants a, b, c, d, e, f between laboratory and field measurements can be due to the large gap in concentration both of p_{H2O} and CO in the two cases. In fact, in laboratory it is possible to send a higher concentration of CO, decided by the operator, while in the field measurement the CO concentration depends on environmental conditions during the day. To deal with this phenomenon, it is possible to introduce a new concept of sensitivity, i.e., the two-dimensional sensitivity, in order to describe the dependence of the response in two directions in the chosen space of phases. As an example, by taking the partial derivative of the fitting function with respect to CO concentration, it is possible to gather not only information about the dependence of the signal variation on the gas concentration, but also how it is influenced by water vapour, even when the p_{H2O} is kept constant, due to the "overlapping" term in Eq. (1). The same can be done for p_{H2O} at a fixed CO concentration, as shown in the following equations:

$$\frac{\partial G_{pH2O,CO}}{\partial p_{H2O}} = \alpha p^{\alpha-1}_{H2O}\left(A + C[CO]^{\gamma}\right) \tag{2}$$

$$\frac{\partial G_{pH2O,CO}}{\partial [CO]} = \gamma [CO]^{\gamma-1}\left(B + Cp^{\alpha}_{H2O}\right) \tag{3}$$

A similar approach can also be obtained by parameterizing the ambient temperature instead of the absolute humidity, which will serve

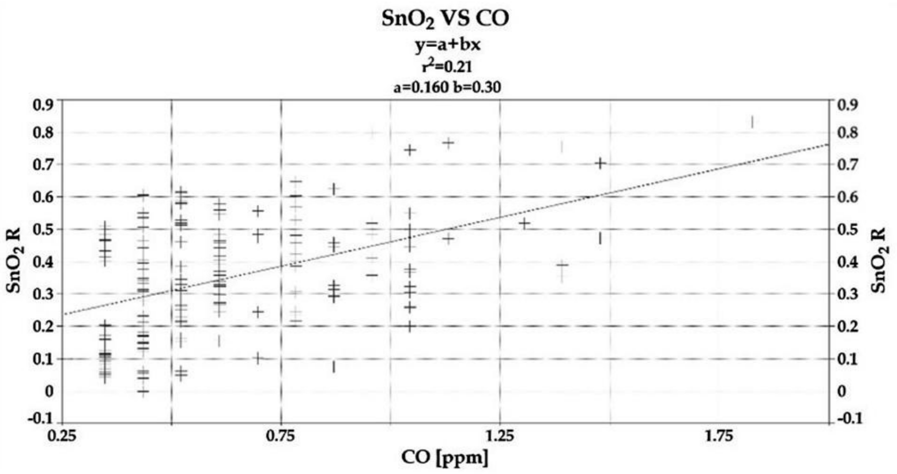

Fig. 10. CO concentration measured with SnO2 sensor.

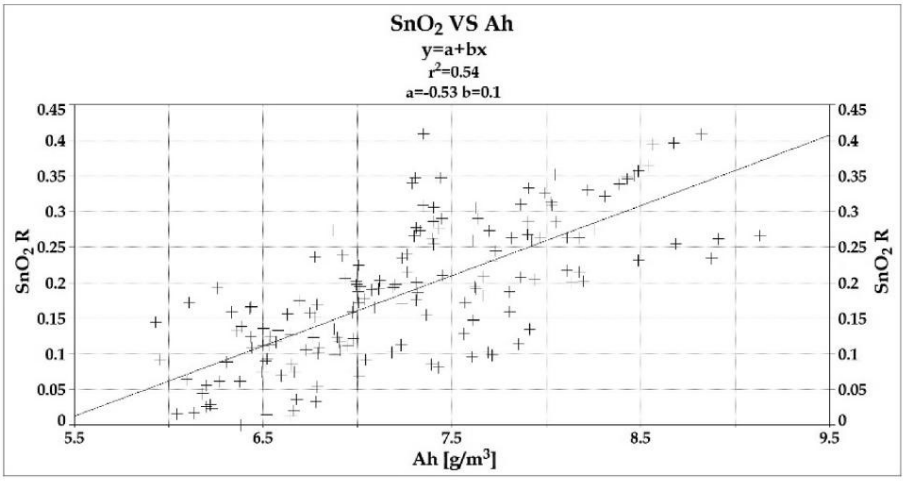

Fig. 11. Water vapor measured with SnO2 sensor – (RH range 18–44%).

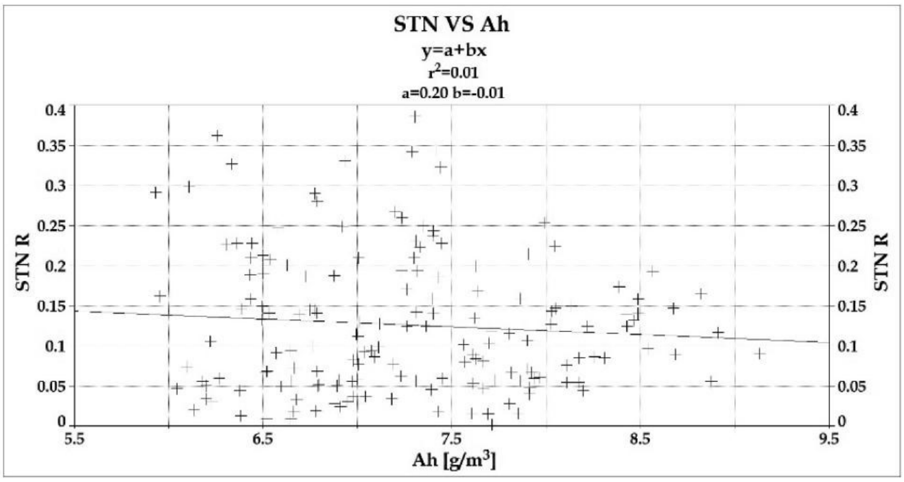

Fig. 12. Water vapor measured with STN sensor – (RH range 18–44%).

for future development of the concept of two-dimensional sensitivity. On the contrary, using simultaneously the three variables [CO], p_{H2O} and T, to realize a response function (from $\mathbb{R}^3$ to $\mathbb{R}$) would be less meaningful due to the lack of visualization possibility.

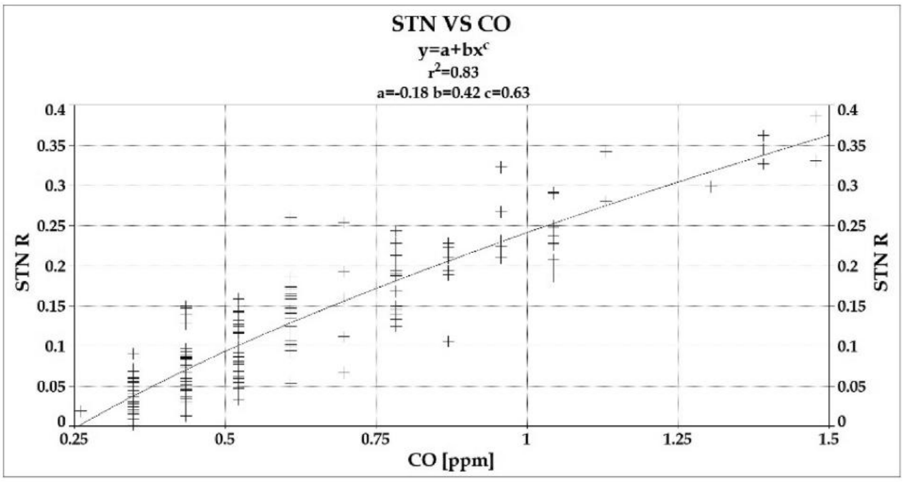

Fig. 13. CO concentration measured with STN sensor.

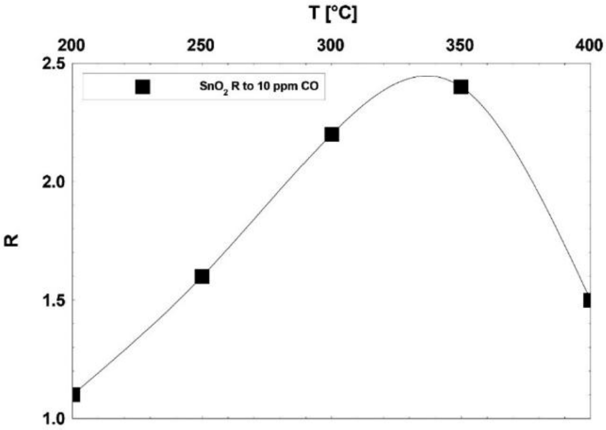

Fig. 14. Temperature dependence of the response to fixed CO concentration for SnO2.

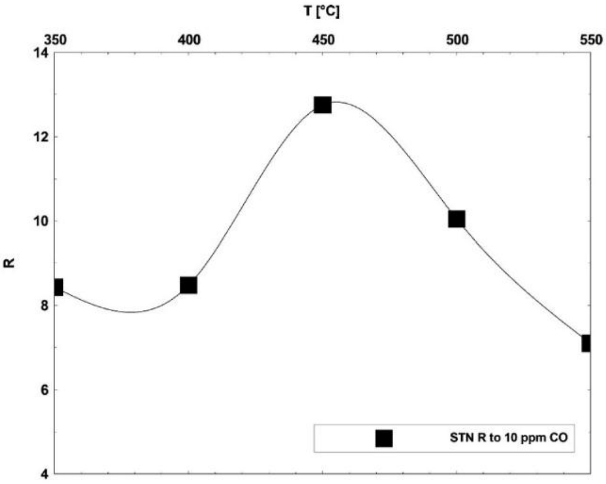

Fig. 15. Temperature dependence of the response to fixed CO concentration for STN.

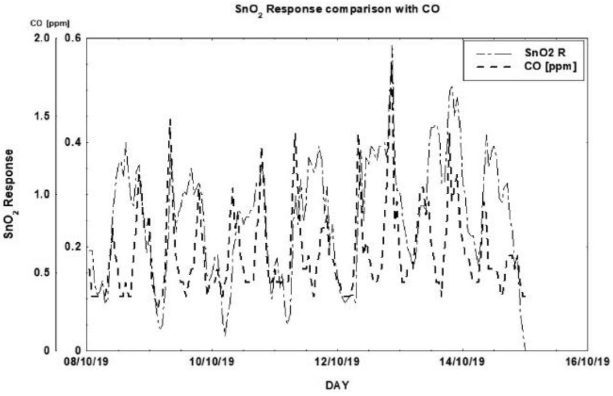

Fig. 16. Time trend of the CO concentration measured with FTIR analyzer compared with the trend of the SnO2 response.

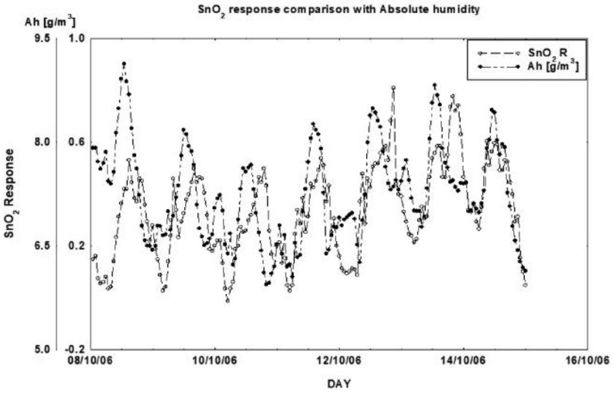

Fig. 17. Time trend of the absolute humidity concentration measured with FTIR analyzer compared with the trend of the SnO2 response.

4. Conclusions

In this work the response of two sensor materials (SnO_2 and STN) has been tested with humidity and CO both singularly and in combination. In Table 1, a summary of specifics of the two sensors is shown.

Material porosity has not been taken into account in this work, as it was already measured for different compositions of SnO_2 and TiO_2 solid

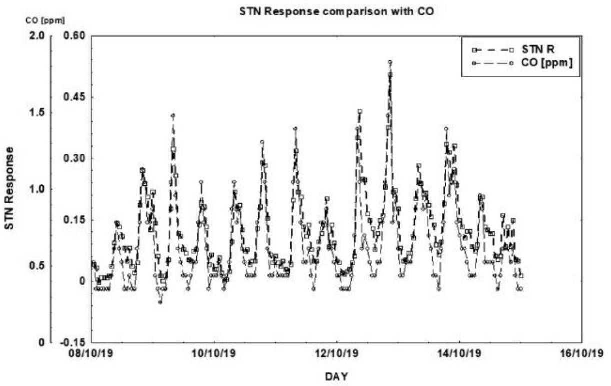

Fig. 18. Time trend of the CO concentration measured with FTIR analyzer compared with the trend of the STN response.

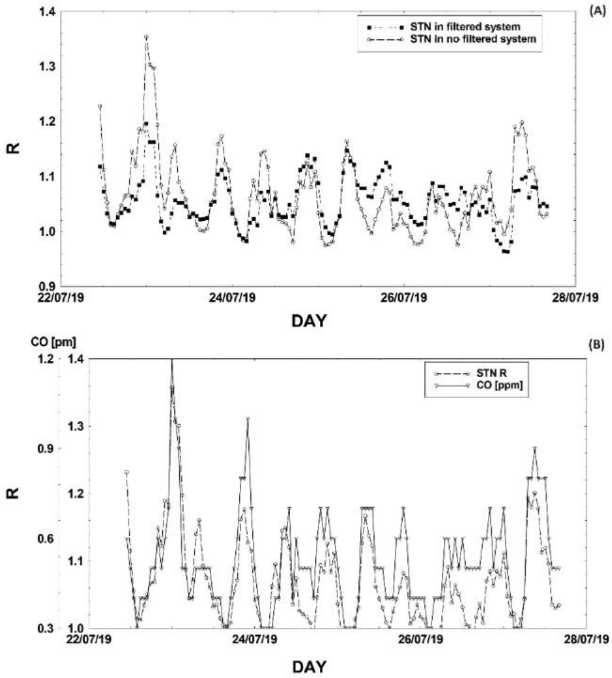

Fig. 19. STN response in a humidity filtered and in a humidity non-filtered system (A); non-filtered STN response to CO (B).

solutions in a previous paper of our research group [25]. However, once measured on the powders, porosity changes in the printed paste and thermally treated as a sensor and it seems that it is not the dominant effect in humidity sensing. By observing two sequential Arrhenius plots for SnO_2 it is evident that they assume different trends, overlapping only at high temperatures. What emerged is that, after having conditioned sensors with a short time heating at a high temperature (700 °C), SnO_2 conductance tends to reach the same values in the whole range, throughout repeated measures. By observing that the conductance trend of a "pre-heated" sensor comes back to a non-overlapping shape between different Arrhenius plots if left at low temperature and in non-dried air overnight, it comes natural to assume that humidity plays a fundamental role in all the conduction and sensing mechanisms of SnO_2. Otherwise, the second material studied (STN), shows a very different behaviour and it that seems to be much less affected by hydroxylated species on the surface. This hypothesis is confirmed by other measurements performed in the presence of both a target gas (CO) and humidity in combination, at different concentrations and partial pressures. This

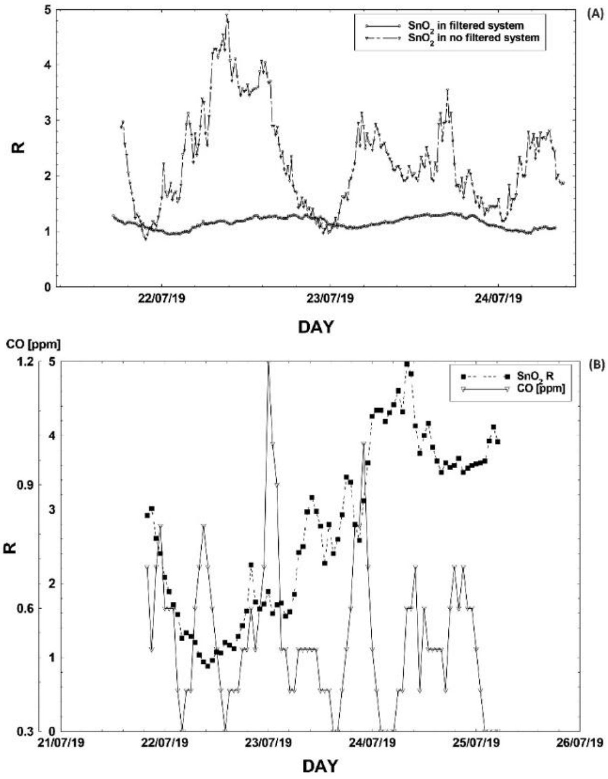

Fig. 20. SnO_2 response in a humidity filtered and in a humidity non-filtered system (A); non-filtered SnO_2 response to CO (B).

investigation led to a mathematical treatment of the two perturbations together with a surface plot instead of the usual response versus gas concentration power law and to introduce a new concept of two-dimensional sensitivity that reflects the greater or lower interference of the humidity on the sensing properties of different materials.

Author's contributions: all authors contributed equally to this work.

Data sharing not applicable – no new data generated: Data sharing is not applicable to this article as no new data were created or analyzed in this study.

Declaration of Competing Interest

The authors declare that they have no known competing financial interests or personal relationships that could have appeared to influence the work reported in this paper.

Appendix A. Supplementary data

Supplementary data to this article can be found online at https://doi.org/10.1016/j.mseb.2020.115013.

References

[1] C. Wang, L. Yin, L. Zhang, D. Xiang, R. Gao, Metal Oxide Gas Sensors: Sensitivity and Influencing Factors, Sensors (Basel), 10(3): 2088–2106, 2010.
[2] Marc J. Madou, S. Roy Morrison, Chemical Sensing with Solid State Devices, ISBN 978-0-12-464965-1, 1989.
[3] A. C. Romain, N. Molitor, G. Adam, E. Bieltot, C. Collard, MOx sensors versus Analysers for the environmental monitoring of landfill air, Conference: International Symposium on Olfaction and Electronic Nose 2015 (ISOEN 2015), At Dijon, France.
[4] G. Adam, S. Lemaigre, X. Goux, P. Delfosse, A.-C. Romain, Upscaling of an electronic nose for completely stirred tank reactor stability monitoring from pilot-scale to real-scale agricultural co-digestion biogas plant, Bioresour. Technol. 178 (2015) 285–296, https://doi.org/10.1016/j.biortech.2014.09.106.

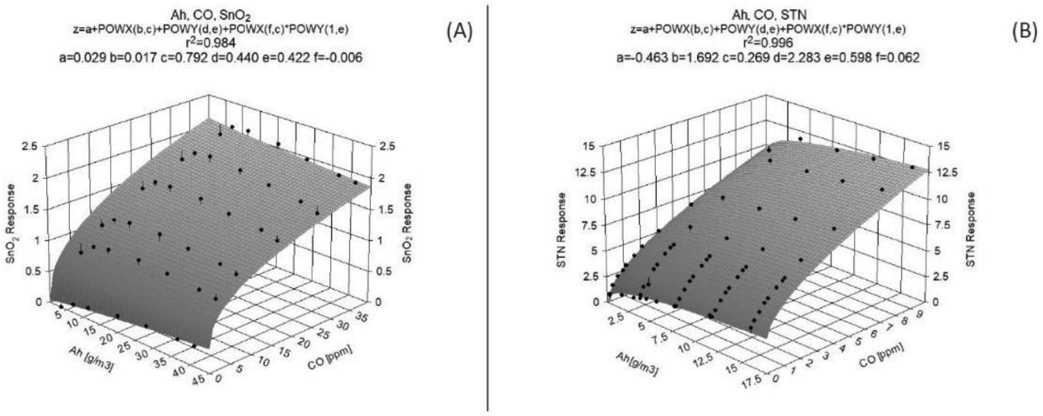

Fig. 21. Analytical surfaces of the response to CO and absolute humidity in combination for SnO2 (A) and STN (B) sensors (laboratory tests).

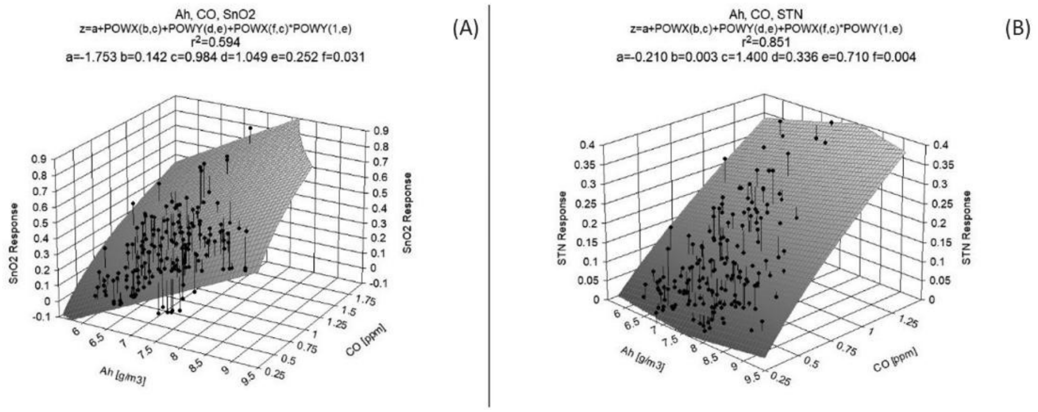

Fig. 22. Analytical surfaces of the response to CO and absolute humidity in combination for SnO2 (A) and STN (B) sensors (field tests).

Table 1
comparison of main characteristics of SnO_2 and STN.

MATERIAL	STN	SnO_2
Nanostructure shape	nanograins	nanograins
Average nanostructure diameter [nm]	80	40
Firing temperature [°C]	650	650
Synthesis process	Sol-Gel	Sol-Gel
r^2 (CO)	0.89	0.29
r^2 (H_2O)	0.25	0.76

[5] C. Jaeschke, O. Gonzalez, M. Padilla, K. Richardson, J. Glöckler, J. Mitrovics, B. Mizaikoff, A Novel Modular System for Breath Analysis Using Temperature Modulated MOX Sensors, DOI: 10.3390/proceedings2019014049, 2019.

[6] C. Malagù, B. Fabbri, S. Gherardi, et al., Chemoresistive gas sensors for detection of colorectal cancer biomarkers, Sensors 14 (2014) 18982–18992.

[7] G. Zonta, G. Anania, B. Fabbri, A. Gaiardo, S. Gherardi, A. Giberti, V. Guidi, N. Landini, C. Malagù, Detection of colorectal cancer biomarkers in the presence of interfering gases, Sens. Actuators, B 218 (2015) 289–295, https://doi.org/10.1016/j.snb.2015.04.080.

[8] N. Landini, G. Zonta, C. Malagù, Detection of tumor markers on feces with nanostructured sensors, Scholars' Press ISBN-13 (2015).

[9] G. Zonta, G. Anania, B. Fabbri, A. Gaiardo, S. Gherardi, A. Giberti, N. Landini, C. Malagù, L. Scagliarini, V. Guidi, Preventive screening of colorectal cancer with a device based on chemoresistive sensors, Sens. Actuators, B 238 (2017) 1098–1101, https://doi.org/10.1016/j.snb.2016.07.079.

[10] G. Zonta, G. Anania, C. Feo, A. Gaiardo, S. Gherardi, A. Giberti, V. Guidi, N. Landini, C. Palmonari, L. Ricci, A. de Togni, C. Malagù, Use of gas sensors and FOBT for the early detection of colorectal cancer, Sens. Actuators, B 262 (2018) 884–891, https://doi.org/10.1016/j.snb.2018.01.225.

[11] G. Zonta, G. Anania, M. Astolfi, C. Feo, A. Gaiardo, S. Gherardi, A. Giberti, V. Guidi, N. Landini, C. Palmonari, A. de Togni, C. Malagù, Chemoresistive sensors for colorectal cancer preventive screening through fecal odor: Double-blind approach, Sens. Actuators, B 301 (2019) 127062, https://doi.org/10.1016/j.snb.2019.127062.

[12] R. Malik, V.K. Tomer, V. Chaudhary, M.S. Dahiya, A. Sharma, S.P. Nehra, S. Duhan, K. Kailasam, An excellent humidity sensor based on In–SnO2 loaded mesoporous graphitic carbon nitride, J. Mater. Chem. A 5 (27) (2017) 14134–14143, https://doi.org/10.1039/C7TA02860A.

[13] V.K. Tomer, S. Devi, R. Malik, S.P. Nehra, S. Duhan, Fast response with high performance humidity sensing of Ag–SnO2/SBA-15 nanohybrid sensors, Microporous Mesoporous Mater. 219 (2016) 240–248, https://doi.org/10.1016/j.micromeso.2015.08.016.

[14] V.K. Tomer, R. Malik, S. Jangra, S.P. Nehrab, S. Duhan, One pot direct synthesis of mesoporous SnO2/SBA-15 nanocomposite by the hydrothermal method, Mater. Lett. 132 (2014) 228–230m, https://doi.org/10.1016/j.matlet.2014.06.088.

[15] Semiconductor gas sensors for environmental monitoring - M.C. Carotta*, E. Ferrari, A. Giberti, C. Malagù, M. Nagliati, S. Gherardi, B. Vendemiati, and G. Martinelli - Advances in Science and Technology Vol. 45, pp. 1818-1827, 2006.

[16] Raivo Jaaniso and Ooi Kiang Tan, Semiconductor gas sensors – Woodhead Publishing Series in Electronic and optical Materials, 38, ISBN: 9780857092366.

[17] E. Traversa, M.L. di Vona, S. Licoccia, M. Sacerdoti, M.C. Carotta, L. Crema, G. Martinelli, Sol-gel processed TiO2-based nano-sized powders for use in thick-film gas sensors for atmospheric pollutant monitoring, J. Sol-Gel Sci. Technol. 22 (2001) 167–179.

[18] M.C. Carotta, M. Benetti, V. Guidi, S. Gherardi, C. Malagu', B. Vendemiati, G. Martinelli, Nanostructured (Sn,Ti, Nb)$_{O}$2 solid solution for hydrogen sensing, MRS Proc. 915 (2006), https://doi.org/10.1557/PROC-0915-R07-10.

[19] I.-D. Kim, A. Rothschild, H.L. Tuller, Advances and new directions in gas-sensing devices, Acta Mater. 61 (3) (2013) 974–1000, https://doi.org/10.1016/j.actamat.2012.10.041.

[20] V. Lantto, P. Rompplainen, S. Leppävuori, A study of the temperature dependence of the barrier energy in porous tin dioxide, Sens. Actuat. 14 (2) (1988) 149–163, https://doi.org/10.1016/0250-6874(88)80062-3.

[21] K. R. Hahn, A. Tricoli, G. Santarossa, A. Vargas, A. Baiker, First Principles Analysis of H2O Adsorption on the (110) Surfaces of SnO2, TiO2 and Their Solid Solutions, Langmuir 2012, 28, 2, 1646-1656 Publication Date:December 7, 2011.

[22] A.V. Bandura, J.D. Kubicki, J.O. Sofo, Comparisons of multilayer H_2O adsorption onto the (110) surfaces of α-TiO_2 and SnO_2 as calculated with density functional theory, J. Phys. Chem. B 112 (37) (2008) 11616–11624.

[23] M.C. Carotta, M. Benetti, E. Ferrari, A. Giberti, C. Malagù, M. Nagliati, B. Vendemiati, G. Martinelli, Basic interpretation of thick film gas sensors for atmospheric application, Sens. Actuators, B 126 (2) (2007) 672–677.

[24] C. Malagù, M. C. Carotta, A. Giberti, V. Guidi, L. Milano, G. Martinelli, Investigation on humidity effect to SnO2-based sensors in CO detection - Symposium R, MRS2006 SPRING MEETING, 15-21 April 2006, San Francisco, USA.

[25] M. C., Carotta, S. Gherardi, V. Guidi, C. Malagu, G. Martinelli, B. Vendemiati, M. Sacerdoti, Electrical and spectroscopic properties of Ti0.2Sn0.8 solid solution for gas sensing, Thin Solid Films, 2009, 517:6176-6183.

4.6 Reproducibility Tests With Zinc-Oxide based sensors

Ceramics International 46 (2020) 6847–6855

Contents lists available at ScienceDirect

Ceramics International

journal homepage: www.elsevier.com/locate/ceramint

Reproducibility tests with zinc oxide thick-film sensors

G. Zonta[a,b,*], M. Astolfi[a,b], D. Casotti[a], G. Cruciani[a], B. Fabbri[a], A. Gaiardo[a,c], S. Gherardi[b], V. Guidi[a], N. Landini[a,b], M. Valt[a], C. Malagù[a,b]

[a] University of Ferrara, Department of Physics and Earth Sciences, Via Saragat 1, 44122, Ferrara, Italy
[b] SCENT S.r.l., Via Quadrifoglio 11, 44124, Ferrara, Italy
[c] MNF - Micro Nano Facility, Bruno Kessler Foundation, Via Sommarive 18, 38123, Trento, Italy

ARTICLE INFO

Keywords:
ZnO
Thick-film
Reproducibility
Gas sensors

ABSTRACT

Reproducibility of the sensor response is one of the fundamental themes for obtaining marketable devices with a high degree of reliability. This parameter becomes decisive especially if the sensor signals are used to identify compound mixtures by means of recognition algorithms. In fact, to apply the same algorithm to different devices, sensors must be identical within a minimum error margin. This point became crucial for medical diagnostic tools, e.g., for cancer screening and monitoring.

A set of three thermo-activated thick-film Zinc Oxide (ZnO) sensors, obtained from the same screen-printing deposition, have been tested in laboratory with diverse gases and two biological fecal samples. Fecal samples have been employed in the clinical validation protocol of a device for non-invasive colorectal cancer pre-screening, as emitters of oncologic volatile biomarkers. Sensors showed a good reproducibility degree, with an error lower than 10% of response value for all compounds, reaching 1%–2% for some gases.

1. Introduction

It is well known that the main fundamental properties of metal-oxide chemoresistive gas sensors are sensitivity, selectivity when combined into arrays and long-term repeatability, which rely on the physical and chemical properties of the semiconductor. Moreover, in commercial applications, repeatability of responses between sensors made of the same materials is also of considerable importance, stating their reproducibility. For this specific issue, the fabrication method of the sensitive layer, subsequent thermal treatments, homogeneity of nanostructures and the deposition of the paste are key aspects to obtain reproducible gas sensing devices. Sensors reproducibility becomes a crucial aspect when they are employed as the core of medical tools for diagnostics, combined into specific arrays in order to obtain the desired selectivity. In these applications, sensor responses are elaborated by analysis algorithms, based on methods as principal component analysis (PCA) or support vector machine (SVM) [1–3] techniques. This step is essential to reach a high discriminating capacity towards the target samples. However, these algorithms are strongly connected to the sensors and to the structural characteristics of devices, since the sample data-set on which they are calibrated are measured with a specific device. For this specific reason, in order to correctly apply the same recognition software to different reproductions of the same device, it is necessary to estimate a minimum error margin, which does not undermine the discriminating capacity. For this purpose, in this paper we carried out multiple tests with gaseous mixtures, to verify that the deviation of each sensor response from the average value remains within a minimum error margin (e.g. 10% of response value).

A set of three thermo-activated thick film Zinc Oxide (ZnO) sensors, obtained from the same print, has been tested in a laboratory setup with CO, NO, CH_4 and butanol. ZnO nanopowder has been prepared through sol-gel synthesis, chosen because it is a highly versatile method with great advantages for the preparation of nanostructured Metal OXides (MOX) for the gas sensor production [4]. Sensor chambers are small and in series with the gas-flow, so that each sensor is exposed to the gas one after the other. The choice of so different gases has been made to show how the degree of reproducibility of ZnO responses is good despite the strong diversity of the chosen chemical compounds. After that, also a test performed on two fecal samples has been carried out. In this biologic samples analysis, exhalations have been sent to sensors in order to state if the response of these materials is reproducible, so that they can be employed in devices for colorectal cancer (CRC) screening. In parallel studies, in fact, our team is working on the clinical validation protocol of a device (SCENT A1), capable of identifying CRC from the difference of fecal fumes emitted by samples from CRC-affected patients and healthy subjects. Sensors reproducibility is fundamental for a future

---

[*] Corresponding author. University of Ferrara, Department of Physics and Earth Sciences, Via Saragat 1, 44122, Ferrara, Italy.
E-mail address: giulia.zonta@unife.it (G. Zonta).

https://doi.org/10.1016/j.ceramint.2019.11.178
Received 30 October 2019; Received in revised form 19 November 2019; Accepted 20 November 2019

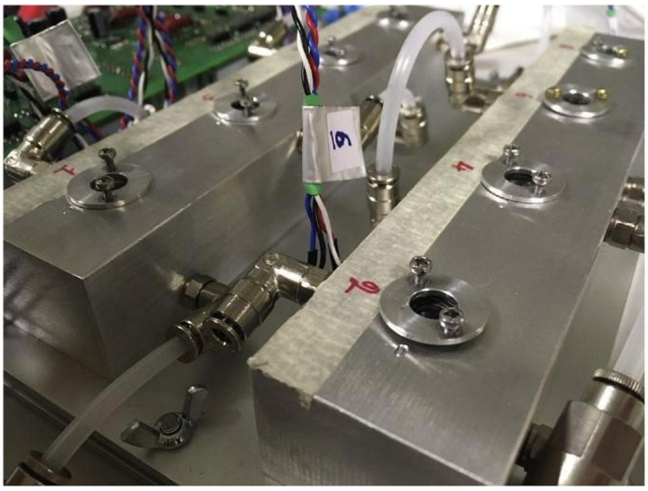

Fig. 1. System 1. Simple-cell chambers in series with the gasflow.

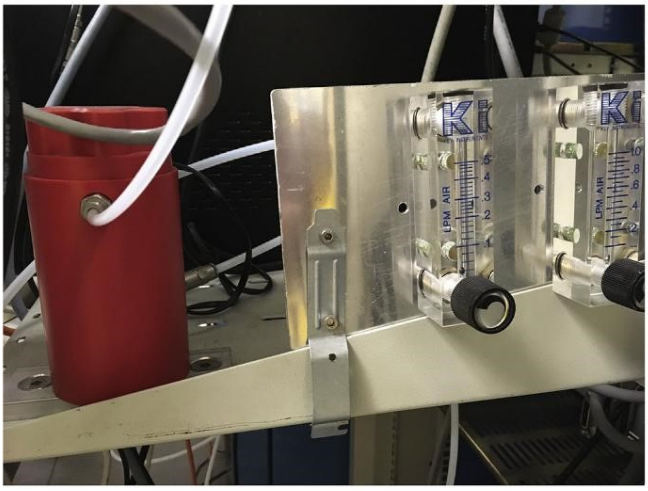

Fig. 2. Biologic sample box (in red) and flow-meters for environmental airflow control. (For interpretation of the references to color in this figure legend, the reader is referred to the Web version of this article.)

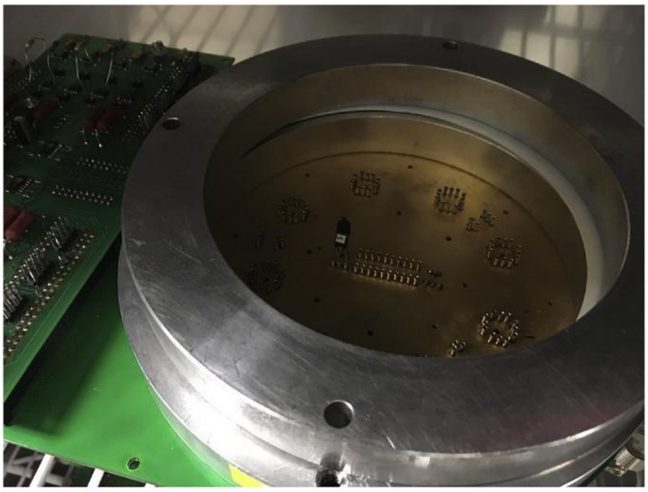

Fig. 3. System 2. Large chamber with gas diffuser in the center.

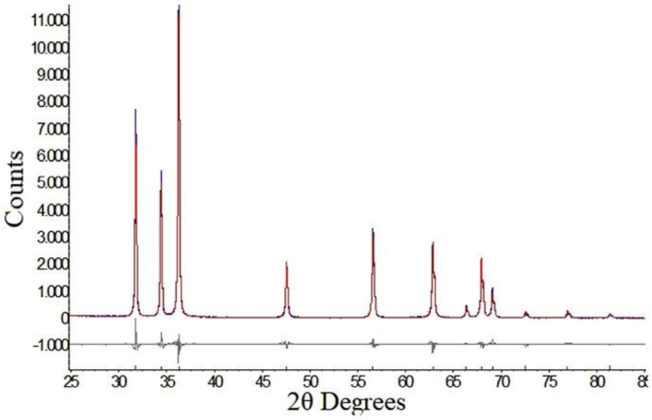

Fig. 4. XRD analysis of the synthesized ZnO powder. The spectra highlights the presence of the Zincite, hexagonal crystal phase (space group P63mc, pdf 036–1415).

Table 1
Lattice parameters of ZnO powder. Spacegroup: P63mc ZnO.

a (Å)	3.250476 (52)
c (Å)	5.207485 (92)
Cell Volume (Å^3)	47.6489 (17)
k: 1 LVol-IB (nm)	63.6 (10) crystal size

application of the specifically built algorithm to other twin devices [1–3,5–8].

In the end, the three sensors have been moved to a system similar to the previous one, which differs only in the measurement chamber configuration. In this second case, the chamber is large and contains all the sensors tested, a humidity sensor and a temperature sensor. The gas flow is diffused from the center, so that sensors are invested parallelly from the gas mixture. Two gases, CO and ethylene, have been tested to state if the reproducibility of sensor responses is affected or not by the geometry of the chamber.

2. Material and methods

2.1. ZnO synthesis and film deposition

ZnO has been synthesized via sol-gel method in a hydroalcoholic solution. 0.1 mol of zinc acetate dihydrate (Sigma Aldrich) was dissolved in 70 mL of 2-propanol by stirring at 40 °C. Then, 30 mL of deionized water has been added and the solution has been stirred for 1 h. The ZnO gel is formed during this step. Afterwards, the solution has been heated at 80 °C for 3 h to evaporate the solvent and the dried gel has been finally thermal treated at 650 °C for 2 h in an oven. The synthesis parameters were chosen by considering results obtained in our previous works [9–11], which allow to prepare ZnO nanograins with optimised sensing properties. The obtained ZnO powder has been then added with organic vehicles, in order to obtain a paste with a proper viscosity and glass frit [9,10]. The sensing paste has been deposited onto an alumina substrate by means of screen-printing technique. The final deposition thickness was about 30 μm [11].

2.2. Sensors characterizations and production

The X-Ray Diffraction (XRD) analysis has been performed by a Bruker D8 Advance diffractometer equipped with a copper X-ray tube operating at 40 kV and 40 mA, and with a LINXEYE XE detector. The identification of the phases has been performed by EVA v.14.0 program by Bruker equipped with the Powder Diffraction File database (PDF) v. 9.0.133. The average crystallite size and the cell parameters have been

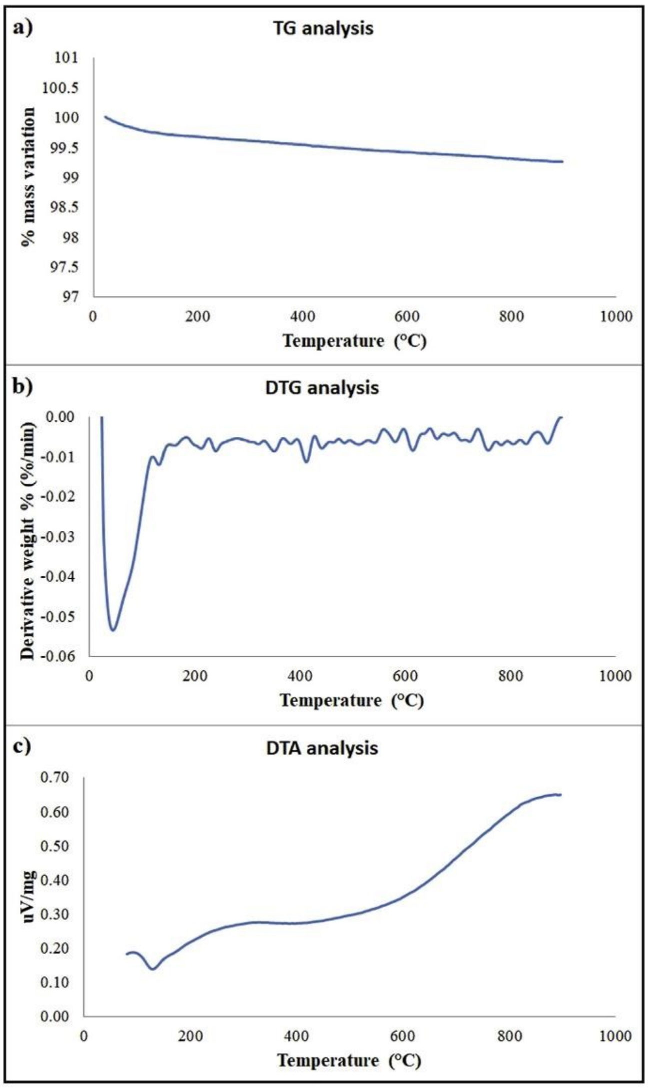

Fig. 5. a) TG/b) DTG/c) DTA analysis of the ZnO powder.

determined by the Rietveld method as implemented in the TOPAS v 4 program by Bruker AXS [12]. The choice of using Rietveld method for average crystallite size calculation is due to the fact that this technique relies on XRD data, obtained by a very large number of crystals (more than hundreds), being more reliable than other techniques. The line-profile fitting has been performed with the fundamental parameters approach [13–16]. The determination of crystallite size by TOPAS has been accomplished by the Double-Voigt approach [17,18]. The volume-weighted for the mean column heights based on integral breadths of peaks has been used to calculate the crystallite size. The thermogravimetric analysis (TG/DTG/DTA) of ZnO has been carried out using a Netzsch 409 PC Luxx TG/DTA thermal analyzer. The powder has been filled in a nickel crucible and analyzed in the range 20–900 °C, with a heating rate of 10 °C·min^{-1} under a constant air flow of 20 mL h^{-1}. Sensors are composed by an alumina substrate (dimensions of 2.53 × 2.53 mm^2), each one provided with a Pt heater element and Au comb-shaped IDT contacts. ZnO paste has been deposited through screen-printing technique onto the substrates, with a deposition area of 1.22 × 1.6 mm^2. A schematic representation of the sensors is shown in previous publications [7]. Three ZnO sensors have been analyzed by Scanning Electron Microscope (SEM) equipped with an Energy Dispersive X-ray Spectrometry (EDS), to state the nanostructure morphology, chemical composition, deposition homogeneity and purity of the material. The instrument utilized was a Zeiss EVO 40 Microscope with an acceleration voltage of 30 kV.

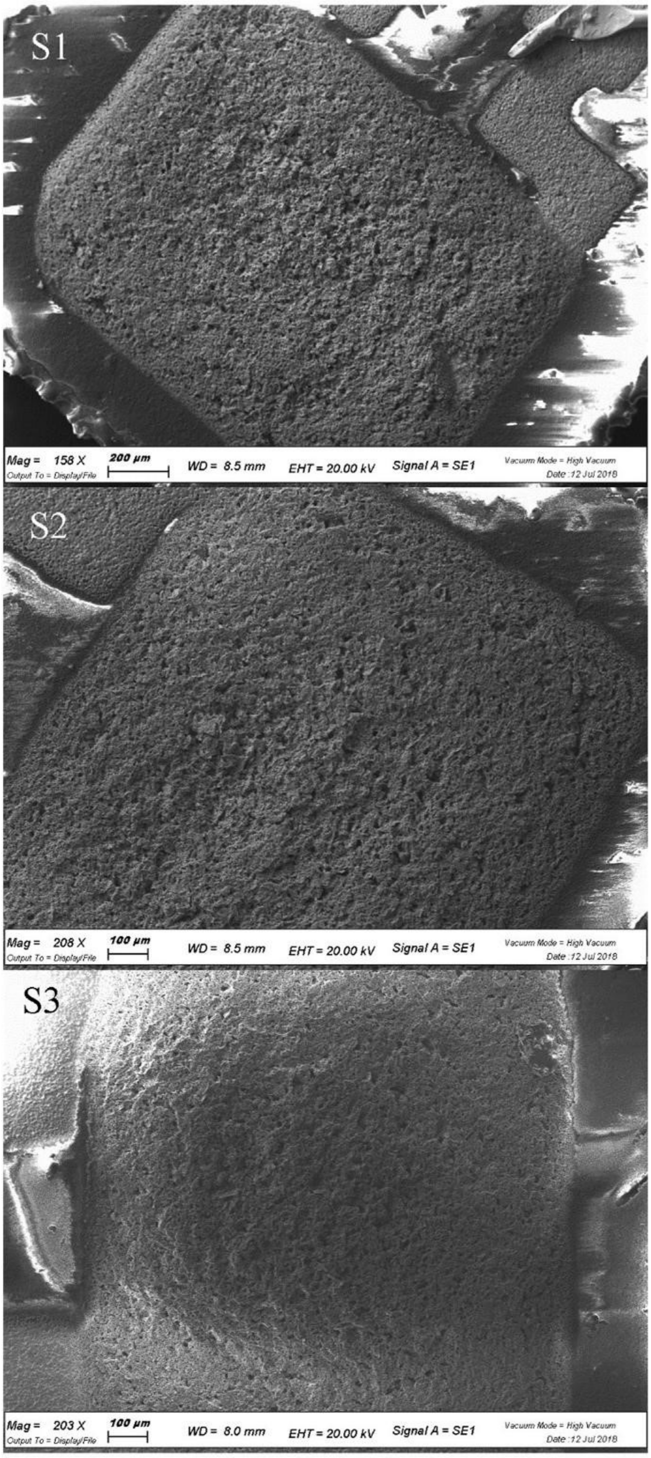

Fig. 6. SEM images of three ZnO sensing films, named S1, S2, S3.

2.3. Experimental set-up

Sensors have been inserted, overturned, in simple-cell chambers with the same diameters of their support (diameter 7.8 mm, height 25 mm). The small size of the chambers ensures a lower response time compared to standard chambers, where the sensors are parallelly hit by

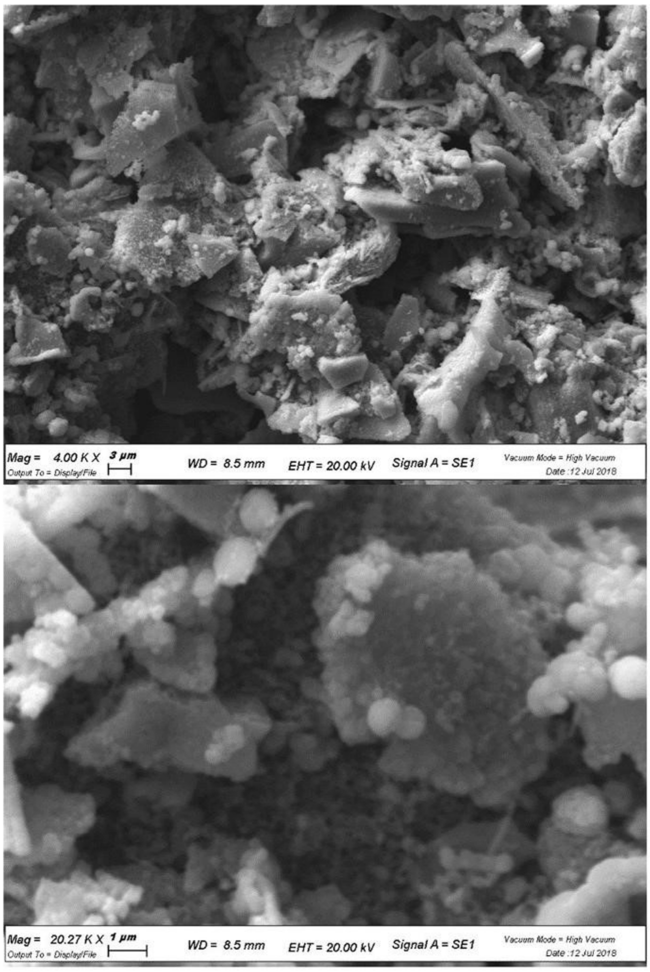

Fig. 7. SEM images of ZnO sensing film (S1) at two different magnifications. The average dimension of nanograins is of 100 nm.

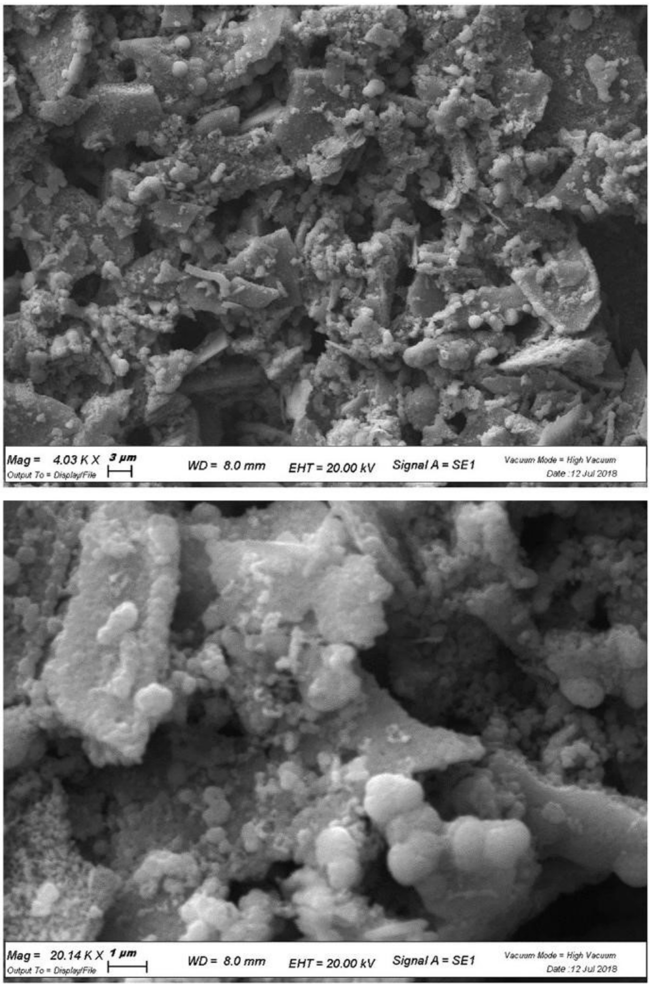

Fig. 8. SEM images of ZnO sensing film (S2) at two different magnifications. The average dimension of nanograins is of 100 nm.

a gas-flow diffused at the center of the chamber. A Teflon tube of 4 mm diameter transports the gas from the bottles to sensors, which are disposed in series with respect to the flow-path (Fig. 1). The gas-flow is modulated thanks to mass-flow controllers (MKS), while a multimeter K2000 (Keitheley) converts all output voltages from analog to digital before being analyzed by a custom-made software in LabVIEW for the response elaboration. For the measurement of biologic samples, the system is the same except for mass-flow controllers. The choice to employ simple-cell chambers for biologic sample tests is due to the fact that this configuration is more similar to the structure of portable devices. The sensor chamber is connected with a 4 mm-diameter Teflon tube to the sample box (Fig. 2) in which the sample is inserted before the analysis. A pump withdraws environmental air which conveys the exhaled gas to the sensors, thanks to a flow deviator. In these measurements it is not necessary to use dry air, as the biological samples internally contain moisture. The only crucial point is to stabilize the environmental airflow thanks to a carbon filter. The temperature is kept almost constant in the laboratory at 24 °C. In the second experimental setup, ZnO samples have been also tested inside a different sensor chamber, to state if this change in geometry can affect the reproducibility of sensor responses. This chamber has a cylindrical shape (diameter: 139 mm, height: 41 mm), it is made of aluminum and hermetically sealed (Fig. 3). At the center of the chamber is placed a gas diffuser, while sensors are positioned circularly around it. Inside the chamber it is possible to place up to eight sensors, together with a humidity sensor and a temperature sensor. Furthermore, it is important to specify that the gas is diffused uniformly inside the chamber, in order to solicit sensors at the same time.To simplify the reading of the work, from now we will indicate the setup with the small, serial measurement chambers as System 1 and the setup with the large chamber as System 2.

3. Experimental

3.1. ZnO characterizations

Fig. 4 shows the XRD characterization of the ZnO nanopowder after the thermal treatment at 650 °C. The phase composition analysis, as described in Section 2, highlighted the high purity of the ZnO produced. The crystal phase of the ZnO sample is 100% Zincite (hexagonal, space group P63mc), and no further crystal phases due to ZnO nanopowder or contaminants have been detected. The crystallite size, estimated through Rietveld method, resulted to be 63.8 ± 0.98 nm. The lattice parameters of ZnO samples are listed in Table 1. The TG analysis shows the high thermal stability of the ZnO sample (Fig. 5). An initial small weight loss has been observed at a temperature of about 100 °C, as it can be noticed from Fig. 5a) and b), probably due to the evaporation of the humidity absorbed in the ZnO nanopowder. The DTA analysis (Fig. 5c) highlighted an endothermic peak at the same temperature, attributable to the energy absorbed by the water molecules to evaporate [19]. The TG (Fig. 5a) and DTG (Fig. 5b) analyses showed a basically stable weight till the temperature of 900 °C. However, the DTA analysis (Fig. 5c) showed an exothermic peak, starting from a temperature

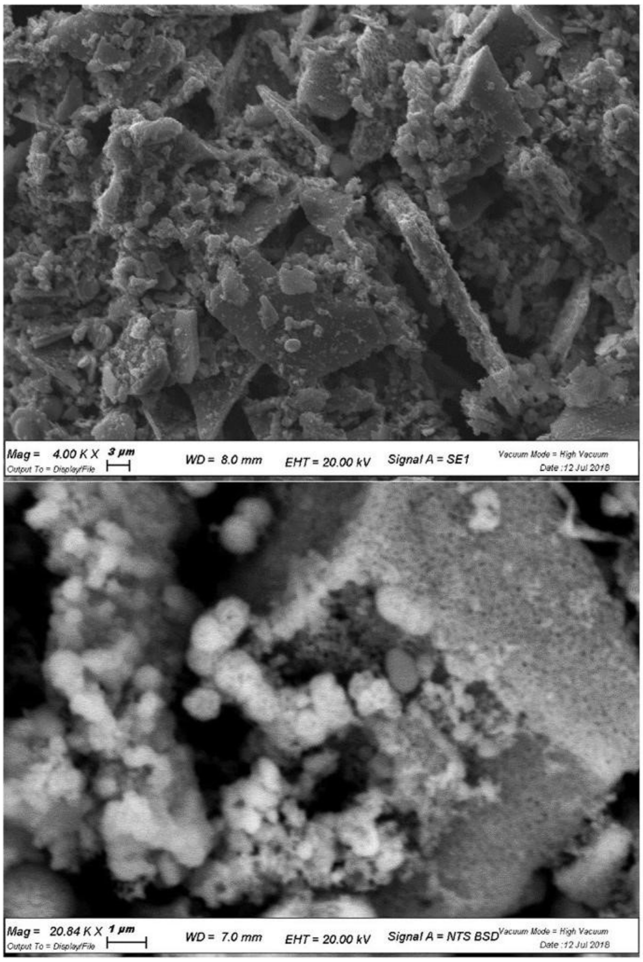

Fig. 9. SEM images of ZnO sensing film (S3) at two different magnifications. The average dimension of nanograins is of 100 nm.

comparable to the one used for the previous ZnO powder firing (650 °C). This peak could be explained through the ZnO grain size increase at temperatures above the firing one, in which the ZnO was stabilized [20].

SEM analysis has been performed on the three chosen samples, here named S1, S2 and S3, to state the reproducibility of their structures. As expected, in Figs. 6–9, the SEM images show a structure of the same type, nanograins of average dimension of 100 nm, for the three sensors without any crack of the film. The same chemical structure is evident from the EDS characterization, reported in Fig. 10. The identified chemical compounds are Zinc, Oxygen and Silicon, where the last is probably a residual from the glass frit, employed to facilitate both the screen-printing and the adhesion of the paste to the substrate, then evaporated with proper thermal treatments.

3.2. Gas measurements in series (system 1)

To test the reproducibility of ZnO sensors, a set of three sensors has been introduced into the measurement chambers of System 1. The gases employed for these tests are: nitric oxide (NO), butanol ($C_4H_{10}O$), methane (CH_4) and carbon monoxide (CO). Responses (R) are calculated as $\frac{\Delta G}{G}$, where ΔG is the difference between conductance with VOCs-contaminated air (G_{gas}) and the conductance in environmental air (G). All the measurements have been performed by setting the ZnO sensors produced at their best working temperature, i.e. 450 °C [21]. The chosen gas concentrations have been decided by considering the sensitivity of ZnO material to the diverse species and the Threshold Limit Value (TLV) or the Lower Explosive Limit (LEL) of those gaseous compounds [22–29].

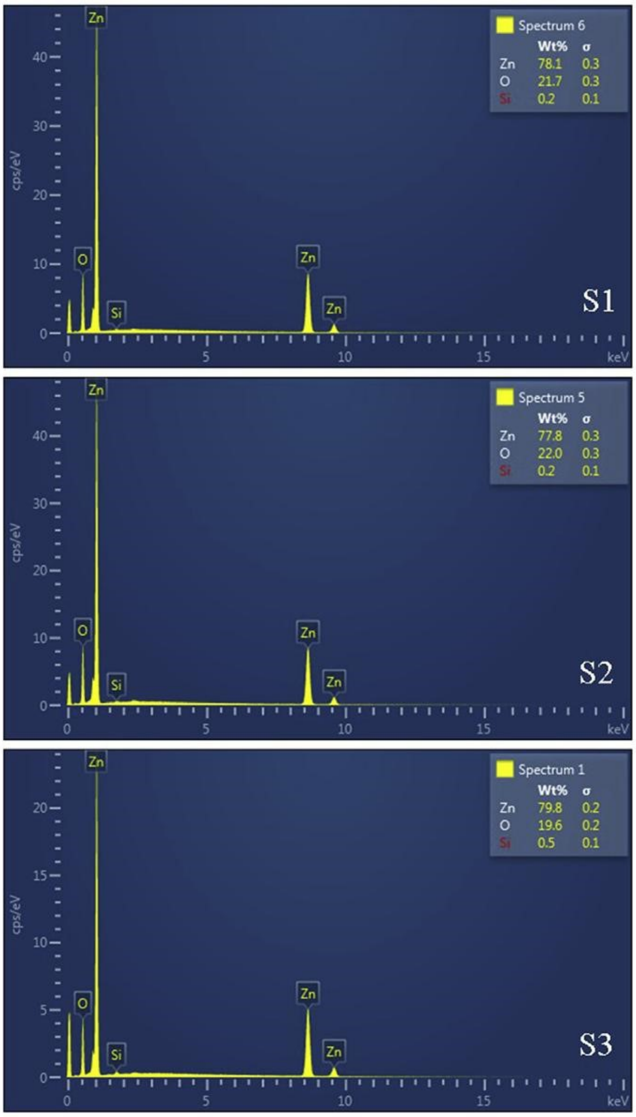

Fig. 10. EDS characterization of S1, S2 and S3 zinc oxide sensor films.

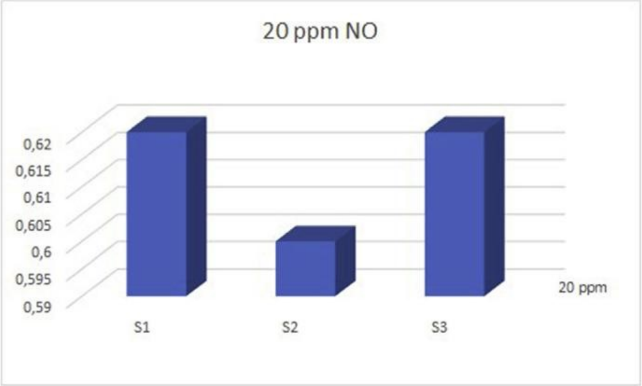

Fig. 11. Histogram of the responses of the three ZnO sensors, S1, S2 and S3 (T = 450 °C) to 20 ppm of NO.

Table 2

Responses (R), absolute distance from mean value (< R ≥ 0,61), 3% of R of the three ZnO sensors tested with 20 ppm NO. All the sensors stands below this value, showing high degree of reproducibility. All the data is approximated at the second decimal place.

SENSORS	S1	S2	S3
R (20 ppm)	0,62	0,60	0,62
|R- < R > |	0,01	0,01	0,01
3% R	0,02	0,02	0,02

Table 3

Responses R to butanol (0,1 ppm, 0,2 ppm and 0,5 ppm), absolute distance from mean value (respectively < R ≥ 0,95; 2,18; 3,43 for the three concentrations). The distance from the mean value of R to butanol stands below 6% for 0,1 ppm and below 2% for 0,2 and 0,5 ppm, showing high degree of reproducibility. All the data is approximated at the second decimal place.

SENSORS	S1	S2	S3
R (0,1 ppm)	1,00	0,90	0,96
|R- < R > |	0,05	0,05	0,01
6% R	0,06	0,05	0,06
R (0,2 ppm)	2,18	2,15	2,21
|R- < R > |	0,00	0,03	0,03
2% R	0,04	0,04	0,04
R (0,5 ppm)	3,42	3,40	3,47
|R- < R > |	0,01	0,03	0,04
2% R	0,07	0,07	0,07

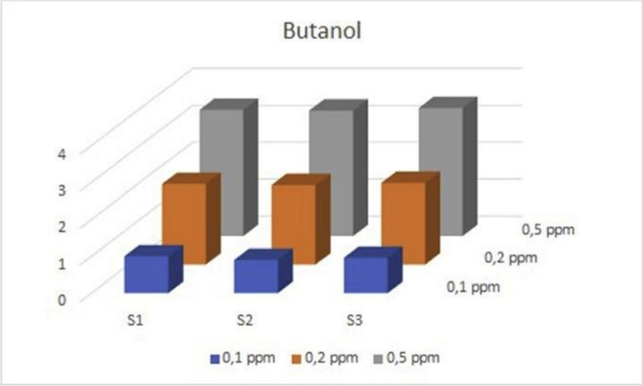

Fig. 12. Histogram of the responses of the three ZnO sensors, S1, S2 and S3 (T = 450 °C) to 0,1 ppm, 0,2 ppm and 0,5 ppm of butanol.

Table 4

Responses R to CO (30 ppm, 50 ppm and 100 ppm), absolute distance from mean value (respectively < R ≥ 0,47; 0,74; 0,95 for the three concentrations). The distance from the mean value of R to CO stands below 4% for 30 ppm, 1% for 50 ppm and below 8% for 100 ppm, showing high degree of reproducibility.

SENSORS	S1	S2	S3
R (30 ppm)	0,45	0,47	0,48
|R- < R > |	0,02	0,00	0,01
4% R	0,02	0,02	0,02
R (50 ppm)	0,76	0,75	0,76
|R- < R > |	0,00	0,01	0,00
1% R	0,01	0,01	0,01
R (100 ppm)	0,97	0,88	0,99
|R- < R > |	0,02	0,07	0,04
8% R	0,08	0,07	0,08

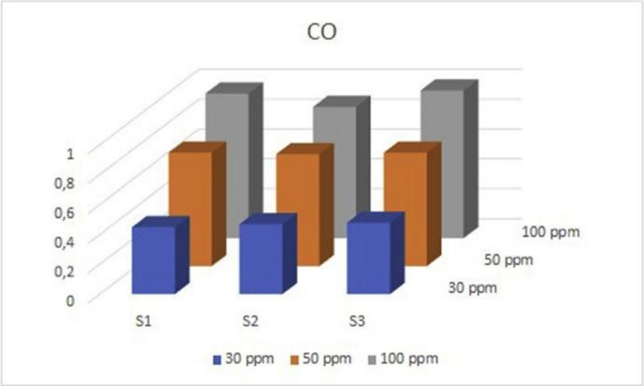

Fig. 13. Histogram of the responses of the three ZnO sensors, S1, S2 and S3 (T = 450 °C) to 30 ppm, 50 ppm and 100 ppm of CO.

Table 5

Responses R to CH_4 (5000 ppm and 1250 ppm), absolute distance from mean value (respectively < R ≥ 0,37 and 0,16 for the two concentrations). The distance from the mean value of R to CH_4 stands below 10% for 5000 ppm and below 9% for 1250 ppm, showing a good degree of reproducibility.

SENSORS	S1	S2	S3
R (5000 ppm)	0,35	0,41	0,35
|R- < R > |	0,02	0,04	0,02
10% R	0,03	0,04	0,04
R (1250 ppm)	0,15	0,17	0,15
|R- < R > |	0,00	0,02	0,01
9% R	0,01	0,02	0,01

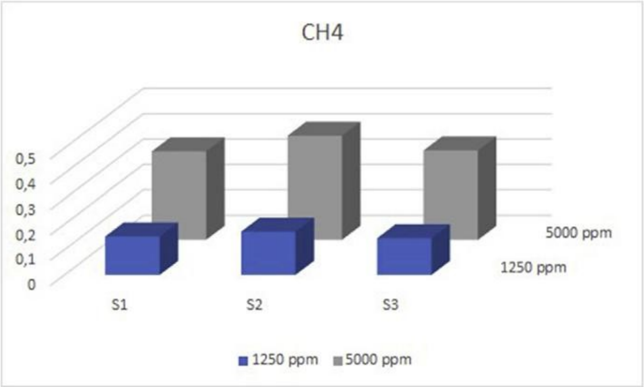

Fig. 14. Histogram of the responses of the three ZnO sensors, S1, S2 and S3 (T = 450 °C) to 1250 ppm and 5000 ppm of CH_4.

NO has been injected at a concentration of 20 ppm and in Fig. 11 a histogram of response values is shown. In Table 2 responses to NO and their difference from the mean response value (< R ≥ 0.61) are reported. What emerges is that, for each sensor, the difference between the response and the mean value is below 3% of R. All the sensors show a high degree of reproducibility when tested with NO.

In Table 3 the same calculation has been performed for butanol at the three concentrations (0,1 ppm, 0,2 ppm and 0,5 ppm) and responses are also shown in the histogram in Fig. 12. The butanol concentrations analyzed were chosen taking into account the high sensitivity of ZnO vs. this gaseous compound, even if far below the butanol TLV [28]. What emerges here is that for 0,1 ppm of butanol, the difference between the response and the mean value is below 6% of R, while for the other two concentrations is even better, i.e., below 2% of R. Higher concentrations of butanol would have brought the sensors to saturation,

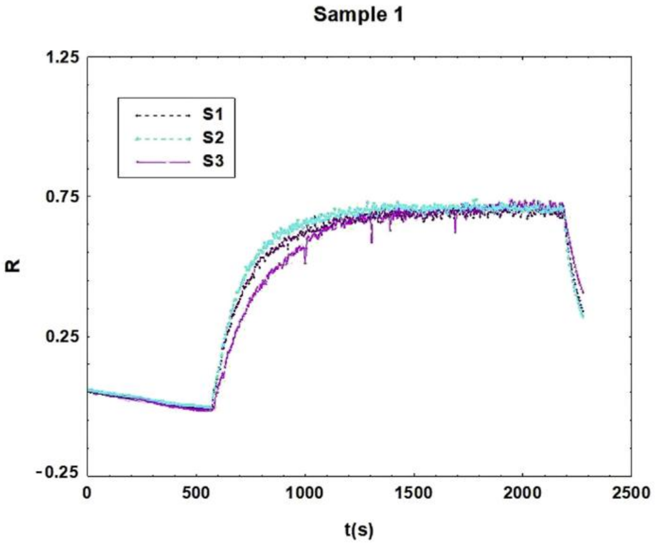

Fig. 15. Dynamic response curve to a fecal sample exhalation (Sample 1) of the three ZnO sensors, S1, S2 and S3 (T = 450 °C).

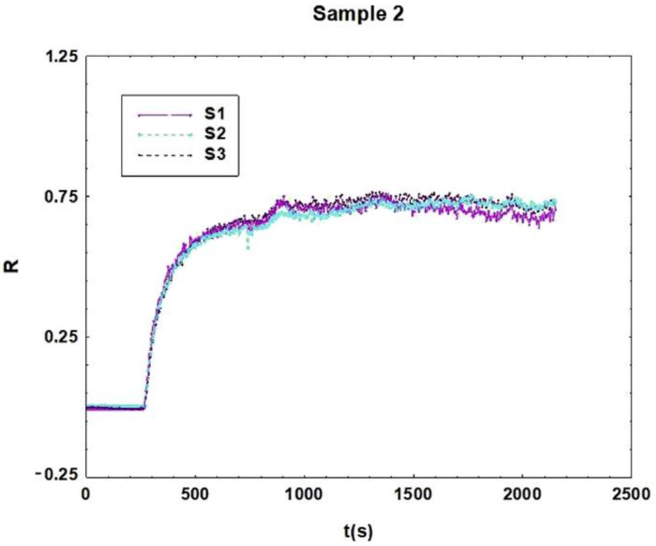

Fig. 16. Dynamic response curve to a fecal sample exhalation (Sample 2) of the three ZnO sensors, S1, S2 and S3 (T = 450 °C).

Table 6
Responses R to two healthy fecal samples (Sample 1 and Sample 2), positive to FOBT. absolute distance from mean value (respectively < R ≥ 0,70 and 0,71). The distance from the mean value of R stands below 2% and 3% for the two samples.

SENSORS	S1	S2	S3
R (Sample 1)	0,69	0,71	0,71
|R- < R > |	0,01	0,01	0,01
2% R	0,01	0,01	0,01
R (Sample 1)	0,72	0,72	0,69
|R- < R > |	0,01	0,01	0,02
3% R	0,02	0,02	0,02

Table 7
Responses R to CO in the large-chamber system (50, 24, 12 and 6 ppm), absolute distance from mean value (respectively < R ≥ 3,71, 2,97, 2,55 and 2,26 for the four concentrations). The distance from the mean value of R to CO stands below 4% of response for 50 ppm, below 5% for 24 ppm, below 6% for 12 and 6 ppm, showing a good degree of reproducibility.

SENSORS	S1	S2	S3
R (50 ppm)	3,73	3,80	3,59
|R- < R > |	0,02	0,09	0,12
4% R	0,15	0,15	0,14
R (24 ppm)	3,00	3,07	2,84
|R- < R > |	0,03	0,10	0,13
5% R	0,15	0,15	0,14
R (12 ppm)	2,59	2,66	2,41
|R- < R > |	0,04	0,10	0,14
6% R	0,16	0,16	0,14
R (6 ppm)	2,30	2,36	2,15
|R- < R > |	0,03	0,09	0,12
6% R	0,14	0,14	0,13

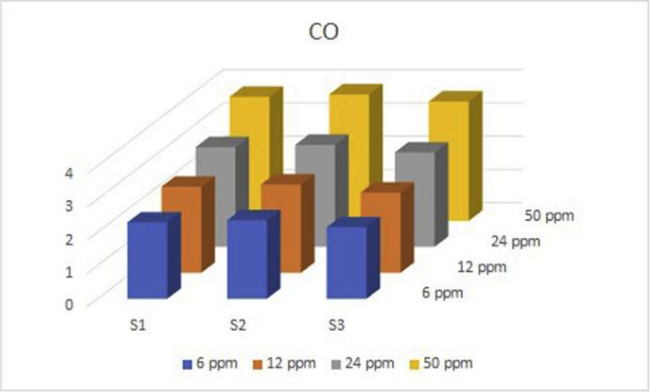

Fig. 17. Histogram of the responses of the three ZnO sensors, S1, S2 and S3 (T = 450 °C) in the large-chamber system to 50, 24, 12 and 6 ppm of CO.

Table 8
Responses R to C_2H_4 in the large-chamber system (44,4, 20, 10 and 5 ppm), absolute distance from mean value (respectively < R ≥ 3,84, 3,13, 2,84 and 2,69 for the four concentrations). The distance from the mean value of R to C_2H_4 stands below 6% of response for 44,4 ppm and below 5% for the remaining concentrations, showing a good degree of repeatability.

SENSORS	S1	S2	S3
R (40,4 ppm)	4,02	3,64	3,87
|R- < R > |	0,17	0,20	0,03
6% R	0,24	0,22	0,23
R (20 ppm)	3,27	2,99	3,15
|R- < R > |	0,14	0,15	0,01
5% R	0,16	0,15	0,16
R (10 ppm)	2,96	2,74	2,83
|R- < R > |	0,12	0,10	0,01
5% R	0,15	0,14	0,14
R (5 ppm)	2,82	2,59	2,66
|R- < R > |	0,13	0,10	0,03
5% R	0,14	0,13	0,13

in fact the ZnO is very sensitive to alcohols. For this specific reason we have selected these low concentration values. In Table 4 the data referred to CO are reported, also graphically shown in the histogram in Fig. 13. For 30 ppm of CO, the difference between the response and the mean value is below 4% of R, while for 50 ppm is only of 1% and for 100 ppm is below 8% of R. Even if the response values to this gas are low, they show a good degree of reproducibility, confirming that ZnO sensors do not lose this characteristic also at small response values. In

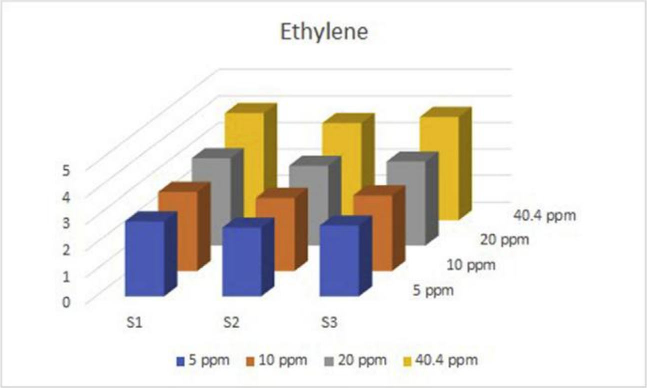

Fig. 18. Histogram of the responses of the three ZnO sensors, S1, S2 and S3 (T = 450 °C) in the large-chamber system to 40.4, 20, 10 and 5 ppm of C_2H_4.

Table 5 data referred to CH_4 (1250 and 5000 ppm, ten times lower the CH_4 LEL [29]) are reported, while sensor response are graphically shown in Fig. 14. The distance from the mean value of R (< R ≥ 0,37 and 0,16 respectively for the two concentrations) for CH_4 stands below 10% for 5000 ppm and below 9% for 1250 ppm, showing a good degree of reproducibility. Methane concentration sent to sensors are two time higher or more than other gases concentration, highlighting how the material is not very reactive towards this gas.

3.3. Fecal samples

By employing the sample box instead of mass flow controllers and gas bottles, System 1 has been adapted to the analysis of biological sample exhalations. Fecal samples exhalation is crucial for CRC-screening as carrier of oncologic biomarkers (peroxidation products and altered metabolites) produced by tumor cells. The clinical validation of a device with a core of MOX sensors is ongoing and reproducibility of sensors is a crucial aspect for a future mass production. Here, two fecal samples (named Sample 1 and Sample 2) from healthy subjects, resulted positive to fecal occult blood test (FOBT) [6], have been tested with three ZnO sensors in System 1. In Figs. 15–16 the dynamic response curves are shown and it is strongly evident that the three sensors outputs are reproducible. In Table 6, response values for the two fecal samples show a high reproducibility degree of ZnO sensors as the distance from the mean value of R stands below 2% and 3% respectively for the two samples. In addition, also the similarity of average sensors response among the two fecal samples confirms the fact that they come from healthy subjects (status confirmed by colonoscopy despite the presence of small amount of blood in feces) and VOCs emitted are the same, due to normal cell metabolism and digestion processes. This point is object of a parallel research on cancer biomarkers in feces and blood, which can be deepened in the references [1–3,5–8].

3.4. Gas measurements in parallel (system 2)

After previous measurements, sensors have been inserted, at the same temperature as before (450 °C), in the System 2, with the large cylindrical chamber. Now sensors are invested at the same time by the gas, diffused uniformly from the center of the chamber. Gas tested are respectively CO and ethylene (C_2H_4), at concentrations chosen by considering the gas TLVs [27,30]. In Table 7 data referred to CO (50, 24, 12 and 6 ppm) are reported, while sensor responses are graphically shown in Fig. 17. The distance from the mean value of R to CO stands below 4% of response for 50 ppm, below 5% for 24 ppm, below 6% for 12 and 6 ppm, showing a high degree of reproducibility. The same has been done for C_2H_4 at the concentrations of 40.4, 20, 10, 5 ppm and the results are tabulated in Table 8 and graphically shown in the histogram in Fig. 18. The distance from the mean value of R to C_2H_4 stands below 6% of response for 40.4 ppm and below 5% for the remaining concentrations, showing a good degree of reproducibility also for ethylene.

By comparing the data referred to CO, tested in both the Systems 1 and 2 (serial small-chambers and large-chamber), it is possible to notice that the reproducibility is good for both systems, what strongly changes are the response values among the two setups. For the common value of 50 ppm of CO, the average response for the three sensors is of 0.76 and 3.71 respectively, almost five times higher for the large-chamber system. The strong difference among these two values should be given by the different dynamics in which the gas-flow reaches the sensor film. In System 1 the flow hits the sensor films tangentially, therefore part of the gas can be carried away by the flow itself during the measurement. For this specific reason, the effective gas concentration on the film surface should be lower than in System 2, where the flow is diffused from the center of the large chamber. Here the atmosphere inside it is more stable, so that the gas can reach the sensors surface without being carried away by the flow during the measurement, resulting in a higher effective gas concentration locally on the sensors [31]. In Fig. 19 a comparison between the dynamic response curves of S1, S2 and S3 to 50 ppm of CO in Systems 1 and 2 is shown. What emerges is also that the time to reach the maximum response value is smaller for System 1 (128 s) than for System 2 (411 s). This should be due to the fact that the

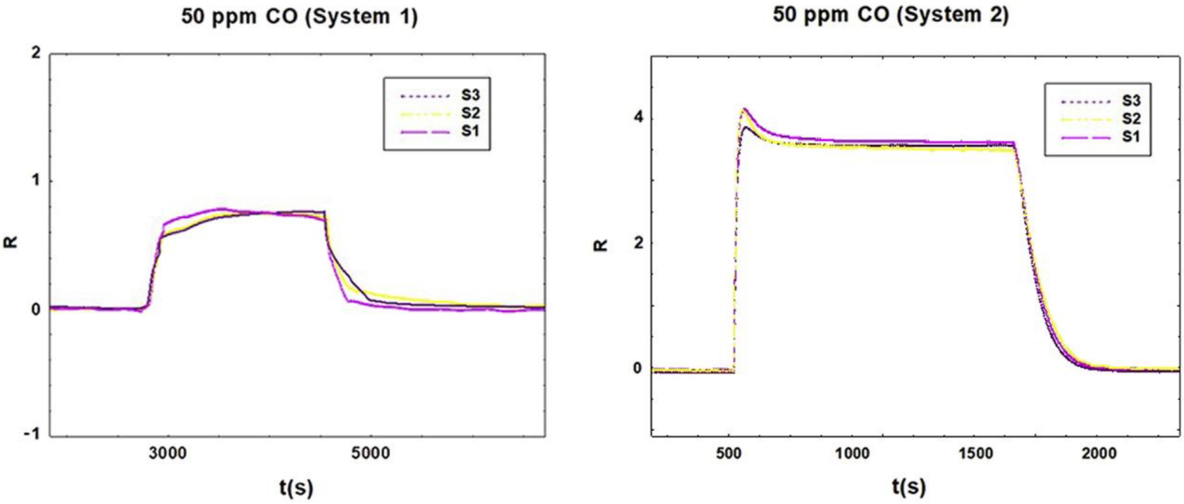

Fig. 19. Dynamic response curves comparison of S1, S2 and S3 at T = 450 °C inside System 1 (left) and System 2 (right) to 50 ppm of CO.

smaller chambers allow the gas to reach the sensor surface more quickly than the larger chamber, in which the gas is diffused from the center, taking a longer time. Regarding the recovery times, they are of 451 and 496 s, respectively for System 1 and 2. The shape of the response curves are similar, despite an initial peak in System 2, probably due to a small overpressure at the entrance to the chamber, which however does not affect the response.

Small serial chambers are the same employed for medical devices for tumor screening and monitoring [31,32] that require the lowest possible measurement time to guarantee the efficiency of medical protocol. This point is fundamental to meet the needs of doctors of performing the highest number of analyzes in the shortest possible time. Moreover, a small size of the measurement chambers is fundamental to ensure portability and compactness of the devices.

4. Conclusions

In conclusion, this work wants to state the repeatability of three ZnO sensors produced at the Sensor Laboratory of the University of Ferrara to different gases inside diverse laboratory set-ups, being reproducibility of sensing materials a crucial point for medical devices relying on the same recognition algorithm. As a matter of fact, to obtain the same information from twin devices, it is essential that the sensing core of the systems (sensors arrays) give the same response within a tolerable error margin.

Reproducibility tests performed in this work, show how the sensor responses always remain within an error margin of the average response value that is lower than 10% of the response itself. For some gases, also smaller percentages are also reached (e.g. 1% for 50 ppm of CO, 2% for 0,2 and 0,5 ppm of butanol), while a percentage of 3% is obtained from biological sample exhalations (stool samples). Two laboratory setups have been tested, one with single-sensor small measurement chambers in series with the gas-flow (System 1) and one with a unique large-chamber, in which all the sensors are inserted together and the gas is diffused from the center (System 2). By comparing the response of ZnO sensors to 50 ppm CO obtained in the two systems what emerges is that, even if the shape of the response curve follows the same trend in both systems, the response is about five times higher in System 2, while the time to reach the peak is smaller for System 1, making small chambers more practical for portable medical devices production.

By observing the data related to biological compounds (fecal samples from healthy subjects) what emerges is the reproducibility of the ZnO gas sensors which can be employed for SCENT medical trials, that require a strong reproducibility of material to use them as the core of serially replicated reliable devices. Notwithstanding the gas-sensing response is strongly affected by the configuration of the experimental setup (e.g. size and geometry of the gas chamber, flux set through mass flow controller), the reproducibility of the measurements between the three different ZnO sensors proved not to be affected by the various setups used. Thus, by establishing the system configuration, it is possible to develop reproducible gas-sensor arrays with comparable behavior.

Declaration of competing interest

The authors declare that they have no known competing financial interests or personal relationships that could have appeared to influence the work reported in this paper.

Acknowledgements

The authors have the pleasure to thank SCENT S.r.l. and LILT (Lega Italiana Lotta Tumori), for having contributed to the financing of the research work carried out and Daniela Palmieri (Centro Microscopia di Ferrara) for having performed SEM analysis on the sensors employed in this work.

References

[1] G. Zonta, G. Anania, B. Fabbri, A. Gaiardo, S. Gherardi, A. Giberti, N. Landini, C. Malagù, L. Scagliarini, V. Guidi, Preventive screening of colorectal cancer with a device based on chemoresistive sensors, Sens. Actuators B (2016), https://doi.org/10.1016/j.snb.2016.07.079.

[2] G. Zonta, G. Anania, A. de Togni, A. Gaiardo, S. Gherardi, A. Giberti, V. Guidi, N. Landini, C. Palmonari, L. Ricci, C. Malagù, Use of gas sensors and FOBT for the early detection of colorectal cancer, Sens. Actuators B Chem. 262 (1 June 2018) 884–891, https://doi.org/10.1016/j.snb.2018.01.225.

[3] N. Landini, G. Anania, B. Fabbri, A. Gaiardo, S. Gherardi, V. Guidi, G. Rispoli, L. Scagliarini, G. Zonta, C. Malagù, Neoplasms and metastasis detection in human blood exhalations with a device composed by nanostructured sensors, Sens. Actuators B Chem. 271 (2018) 203–214, https://doi.org/10.1016/j.snb.2018.05.102 15 October 2018.

[4] A. Wilson, J.D. Wright, J.J. Murphy, M.A.M. Stroud, S.C. Thorpe, Sol-gel materials for gas-sensing applications, Sens. Actuators B Chem. 19 (1–3) (1994) 506–510.

[5] C. Malagù, B. Fabbri, S. Gherardi, A. Giberti, V. Guidi, G. Zonta, Chemoresistive gas sensors for detection of colorectal cancer biomarkers, Sensors 14 (2014) 18982–18992, https://doi.org/10.3390/s141018982.

[6] G. Zonta, G. Anania, B. Fabbri, A. Gaiardo, S. Gherardi, A. Giberti, V. Guidi, N. Landini, C. Malagù, Detection of colorectal cancer biomarkers in the presence of interfering gases, Sens. Actuators B 218 (2015) 289–295.

[7] N. Landini, G. Zonta, C. Malagù, Detection of Tumor Markers on Feces with Nanostructured Sensors, Scholars' Press, 2015-06-15 ISBN-13: 978-3-639-76538-0.

[8] G. Zonta, G. Anania, M. Astolfi, C. Feo, A. Gaiardo, S. Gherardi, A. Giberti, V. Guidi, N. Landini, C. Palmonari, A. de Togni, C. Malagù, Chemoresistive Sensors for Colorectal Cancer Preventive Screening through Fecal Odor: Double-Blind Approach 301 (2019) 12706212 December.

[9] A. Gaiardo, B. Fabbri, A. Giberti, V. Guidi, P. Bellutti, C. Malagù, M. Valt, G. Pepponi, S. Gherardi, G. Zonta, A. Martucci, M. Sturaro, N. Landini, ZnO and Au/ZnO thin films: room-temperature chemoresistive properties for gas sensing applications, Sens. Actuators B 237 (2016) 1085–1094.

[10] Fabbri, A. Gaiardo, A. Giberti, V. Guidi, C. Malagù, A. Martucci, M. Sturaro, G. Zonta, S. Gherardi, P. Bernardoni, Chemoresistive properties of photo-activated thin and thick ZnO films, Sens. Actuators B 222 (2016) 1251–1256.

[11] V. Guidi, C. Malagù, M.C. Carotta, B. Vendemiati, Printed Semiconducting Gas Sensors, Electronics and Photonics, 2012, pp. 278–334 Printed Films: Materials Science and Applications in Sensors.

[12] Bruker AXS. TOPAS 4 – 1 User Manual; Bruker AXS GmbH,Karlsruhe, Germany.

[13] R.W. Cheary, A. Coelho, J. Appl. Crystallogr. 25 (1992) 109–121.

[14] R.W. Cheary, A. Coelho, J.P. Cline, J. Res. Natl. Inst. Stand.Technol. 109 (2004) 1–25.

[15] A. Kern, A. Coelho, A.R.W. Cheary, Diffraction Analysis of the Microstructure of Materials, 2004.

[16] P. Mittemeijer, P. Scardi (Eds.), Springer Series in Materials Science, Springer, Berlin, 2004.

[17] D. Balzar, In Microstructure Analysis from Diffraction.

[18] R.L. Snyder, H.J. Bunge, J. Fiala (Eds.), International Union of Crystallography, 1999.

[19] D. Casotti, M. Ardit, R. Dinnebier, M. Dondi, F. Matteucci, I. Zama, G. Cruciani, Limited crystallite growth upon isothermal annealing of nanocrystalline anatase, Cryst. Growth Des. 15 (5) (2015) 2282–2290.

[20] H.F. Lopez, H. Mendoza, Temperature Effects on the Crystallization and Coarsening of Nano-CeO2Powders 2013 ISRN Nanomaterials, 2013, p. 7. Article ID 208614.

[21] M.C. Carotta, A. Cervi, V. di Natale, S. Gherardi, A. Giberti, V. Guidi, D. Puzzovio, B. Vendemiati, G. Martinelli, M. Sacerdoti, D. Calestani, A. Zappettini, M. Zha, L. Zanotti, ZnO gas sensors: a comparison between nanoparticles and nanotetrapods-based thick films, Sens. Actuators B Chem. 137 (1) (2009) 164–169.

[22] P. Bhattacharyya, P.K. Basu, H. Saha, S. Basu, Fast response methane sensor using nanocrystalline zinc oxide thin films derived by sol–gel method, Sens. Actuators B Chem. 124 (Issue 1) (10 June 2007) 62–67.

[23] N.H. Hasanuddin, M.H.A. Wahid, M.M. Shahimin, N.A.M.A. Hambali, N.S. Nazir, N.Z. Khairuddin, M.M. Ramli, S.S.M. Isa, Design and development of ZnO based gas sensor for fruit ripening detection, MATEC Web of Conferences 7 (2016) 01109, , https://doi.org/10.1051/matecconf/20167801109.

[24] M. Hjiri, L. El Mir, S.G. Leonardi, N. Donato, G. Neri, CO and NO2 selective monitoring by ZnO-based sensors, Nanomaterials 3 (3) (2013 Sep) 357–369.

[25] F.E. Annanouch, G. Bouchet, P. Perrier, N. Morati, C. Reynard-Carette, K. Aguir, M. Bendahan, How the chamber design can affect gas sensor responses, Proceedings 3 (2018) 820, https://doi.org/10.3390/proceedings2130820.

[26] https://www.cdc.gov/niosh/npg/npgd0448.html.

[27] https://www.cdc.gov/niosh/pel88/630-08.html.

[28] https://www.cdc.gov/niosh/idlh/71363.html.

[29] https://pubchem.ncbi.nlm.nih.gov/compound/Methane#section = GHS-Classification.

[30] https://www.cdc.gov/niosh/ipcsneng/neng0475.html.

[31] Patent, C. Malagu, G. Zonta, S. Gherardi, A. Giberti, N. Landini, A. Gaiardo, Dispositivo per lo screening preliminare di adenomi al colon-retto, (2014) National #: RM2014A000595, European #: 3210013 (Germany, UK).

[32] Patent, C. Malagù, S. Gherardi, G. Zonta, N. Landini, A. Giberti, B. Fabbri, A. Gaiardo, G. Anania, G. Rispoli, L. Scagliarini, Combinazione di materiali semiconduttori nanoparticolati per uso nel distinguere cellule normali da cellule tumorali, (2015) National #: 102015000057717.

5 Development of a novel SCENT device

The idea to develop a completely new sensing device, derives from the need of SCENT S.r.l. company to overcome the weaknesses of the original SCENT B1 prototype, such as the poor computing power, serial communication protocol instability, recurrent electric shocks etc. This project requires a complete re-design of all the device components, such as electronics, pneumatics, software and enclosure, aiming to produce a completely reproducible and scalable definitive product, suitable for the market entry. At first, the implementation of a new electronic system based on the last generation electronic components (e.g., MOSFETs, LDO voltage regulators, integrated circuits (IC), low noise operational amplifier, etc.) is crucial to optimize the device dynamics and precision (i.e., reducing the power supply ripple, increasing the signal-to-noise ratio, stabilizing the sensor signal and reducing the device heating). The electronics is completely managed through an ad-hoc software written in Python programming language that, besides managing the electronical components through an i2c serial interface, includes also other useful functions and services to simplify the research work and the experiment data reportage and collection. This improved device has been conceived to completely replace the first SCENT B1 prototype in the biomedical research applications, with design and assembly procedure satisfying all the mandatory constraints to obtain the IDV medical device certification (CE), following the new European law 2017/746.

The new electronics is based on a Raspberry Pi4 developing board, used as computational and i2c serial communication unit. Raspberry Pi4 manages five electronic boards (a power supply board and four sensor control ones):

- the power supply board provides the required voltage outputs to each sensor board to feed the sensor sensing film, the active electronic components and the heater. It includes also a I2C MUX, suitable to split the unique Raspberry serial I2C interface in 8 different ones, so providing an own I2C interface to every sensor board, simplifying their software management and programming;
- the sensor board includes the heater and sensing film feeding electronic circuits. It is equipped also with an analog-to-digital converter (ADC) to acquire the output electric signals.

The management software is installed on the Raspberry Pi4 control board and it is executed at its boot. This software is made by three main parts:

- the electronics management system, indispensable to control the electronics and to acquire data;

- the real time data representation, storage and plotting;
- the record of sensor features and job setups in a constantly updated history sensor list.

In the next sub-paragraphs, the enclosure, electronics and software designs will be explained separately in details.

5.1 Device Enclosure

The device has been realized starting from the enclosure re-designing, making it suitable to contain two sensor channels to perform two analysis at the same time. It has been drawn as 3d model, by means of the Autodesk Fusion 360 software, optimizing the project for a metallic realization (probably in alloy). It shows generous dimensions, about 500 x 350 x 300 mm and the structure width is about 3 mm. The choice concerning the employment of metallic material derives from the need to produce a case capable of shielding the device electronic boards from possible environmental electromagnetic interferences, avoiding some device anomalies and malfunctioning. The frontal part hosts four slots to accommodate four fluxmeters (two for each analysis channel), a wide cooling air inlet and a wide slot to accommodate a 7-inch screen (figure 5.1.1a). Other cooling air inlets are placed on both the lateral sides. The top cover, hermetically closing the device, will be made in transparent plexiglass screwed to the guides included on top (figure 5.1.1b).

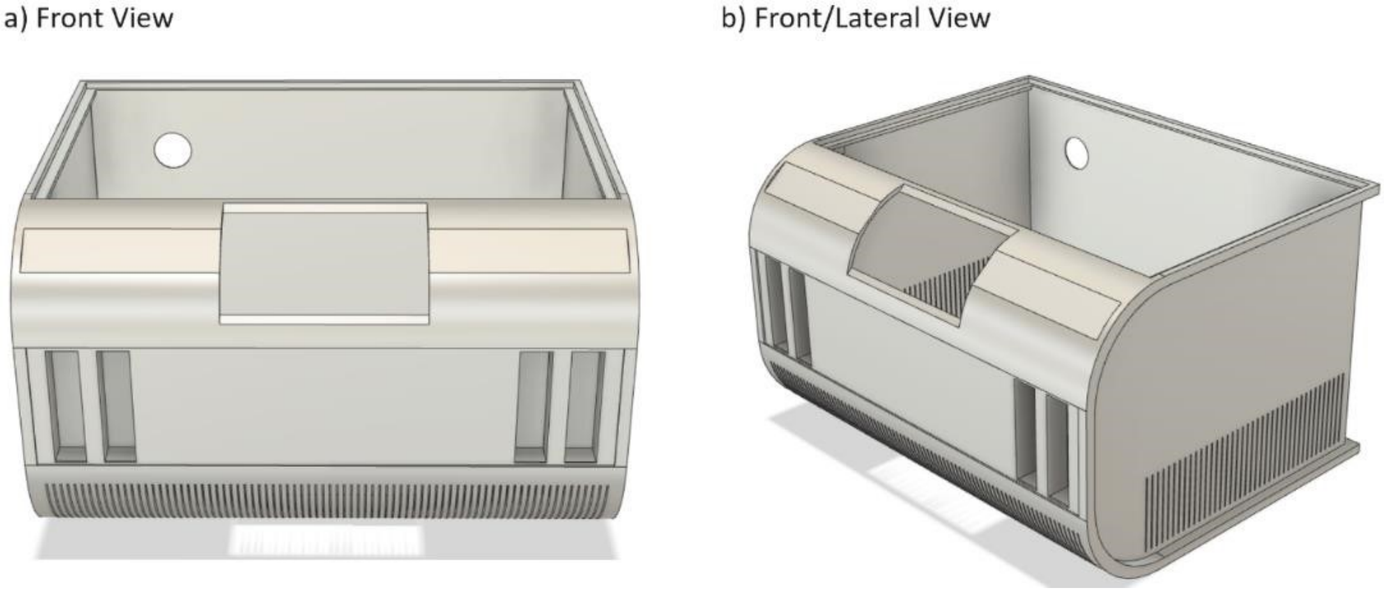
a) Front View
b) Front/Lateral View

Figure 5.1.1: a) Frontal view of the case; b) Frontal/lateral view of the case.

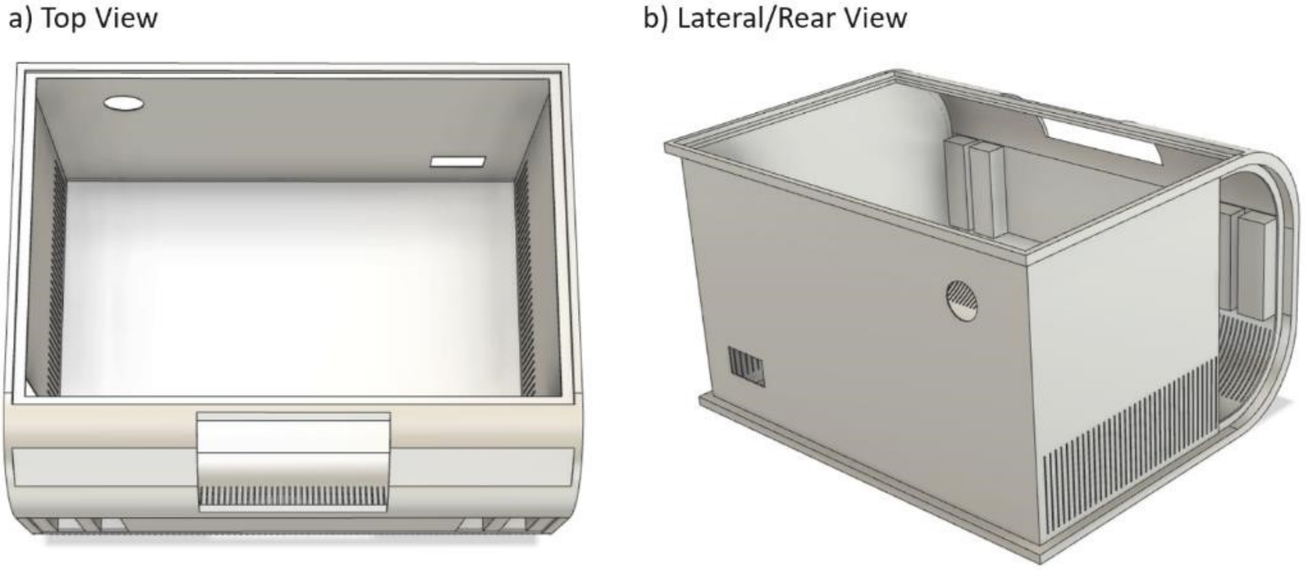

Figure 5.1.2: a) Top view of the case; b) Lateral/rear view of the case.

On the back side, a fan and a supply plug/on-button slots are applied. The next step consists in the optimization of the internal spaces on the basis of the encumbrance and the shape of the contained hardware (electronic boards, pneumatic system, power supply unit, Raspberry Pi4 control unit, etc.).

5.2 Device Electronics

The electronics has been completely re-designed on the basis of the newer and optimized electronic components existing on the market. The device is fed by a classic switching power supply, finely filtrated and stabilized through the power supply board (figure 5.2.1). It has to provide enough power to simultaneously feed the Raspberry Pi4 unit, two air pumps, a cooling fan, two 3-way electro valve and four sensor boards. Moreover, it includes also a I2C multiplexer (MUX), capable of splitting the unique Raspberry Pi4 I2C channel in 8 different ones, providing an own I2C channel to each sensor board, so simplifying its software programming and managing. The supply board feeds all the sensor boards and the Raspberry Pi4 as needed, with the possibility to swich off only the latter, leaving the electronics running. This step is strictly indispensable to ensure the sensor constant heating and stabilization of the resulting response in air conditioning, i.e., the baseline (see chapter 1). The four sensor boards, two per sensor channel, are connected to the supply board mainly through four wires: 12V supply (red wire), ground contact (GND; black wire), I2C SDA (data; orange wire) and I2C SCL (clock; yellow wire) as shown in figure 5.2.1. A sensor board includes, in turn, the sensor heating and the sensor feeding and signal acquisition circuits, as sketched in a block diagram in figure 5.2.2.

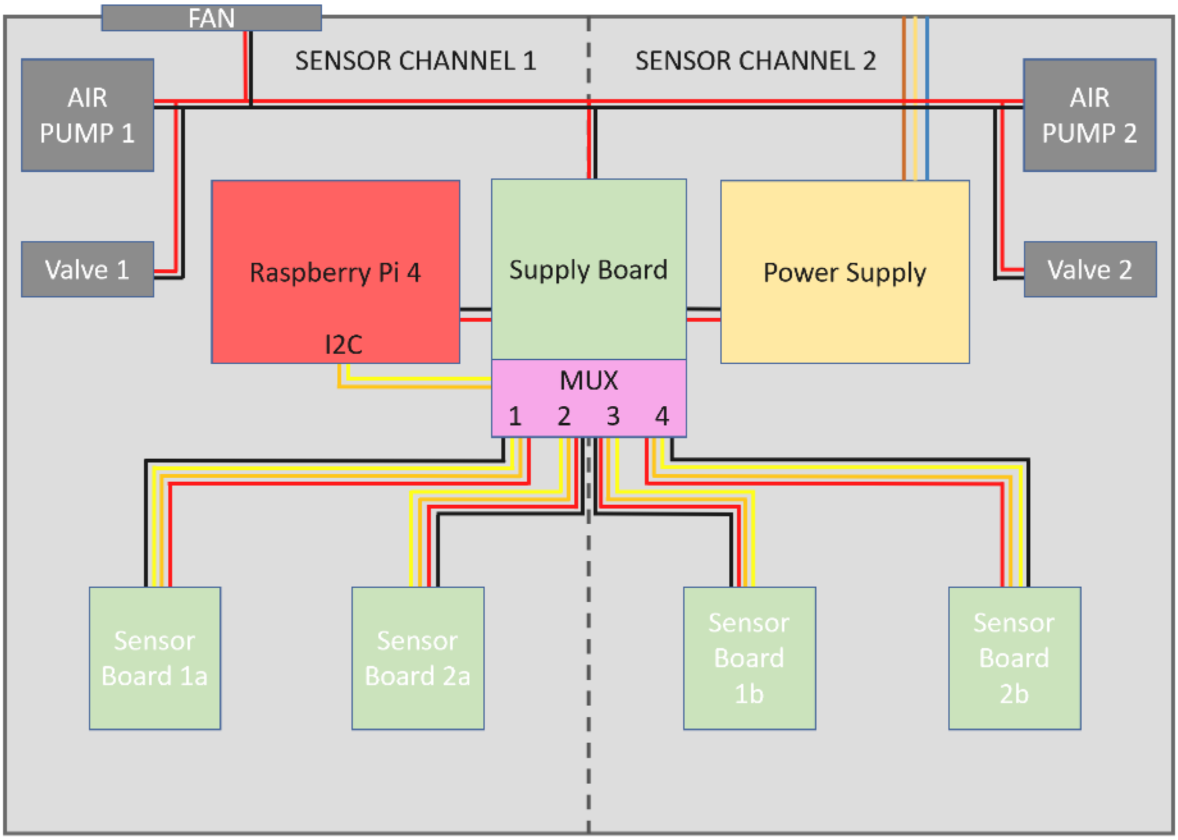

Figure 5.2.1: Block sketch of the electronic system inside the new SCENT device. It is structured into two sensor channels (two independent sub-devices) to perform two analysis concurrently. Each sensor channel shares the power supply and the Raspberry Pi4 with the other, but it has its own air pump, electro valve and two sensor boards.

The sensor heating circuit is based on a DAC (digital-to-analog converter; here a MCP4725 device has been employed) controlled LDO IC device (here a LT3083, produced by Linear Technology, has been employed). The LDO is suitable to provide an adjusted high power signal to a resistive load (here the sensor heater) controlled by a low power one (here provided by the DAC device). For a better understanding, the chain of events is the following: the Raspberry Pi4 unit controls the DAC output voltage, capable of providing a low power voltage signal ranging from 0 to 5 volts; the DAC output, amplified x 2, controls the LDO voltage output (see LDO LT3083 datasheet), so providing a high power voltage signal of the same amplitude as DAC one (figure 5.2.3).

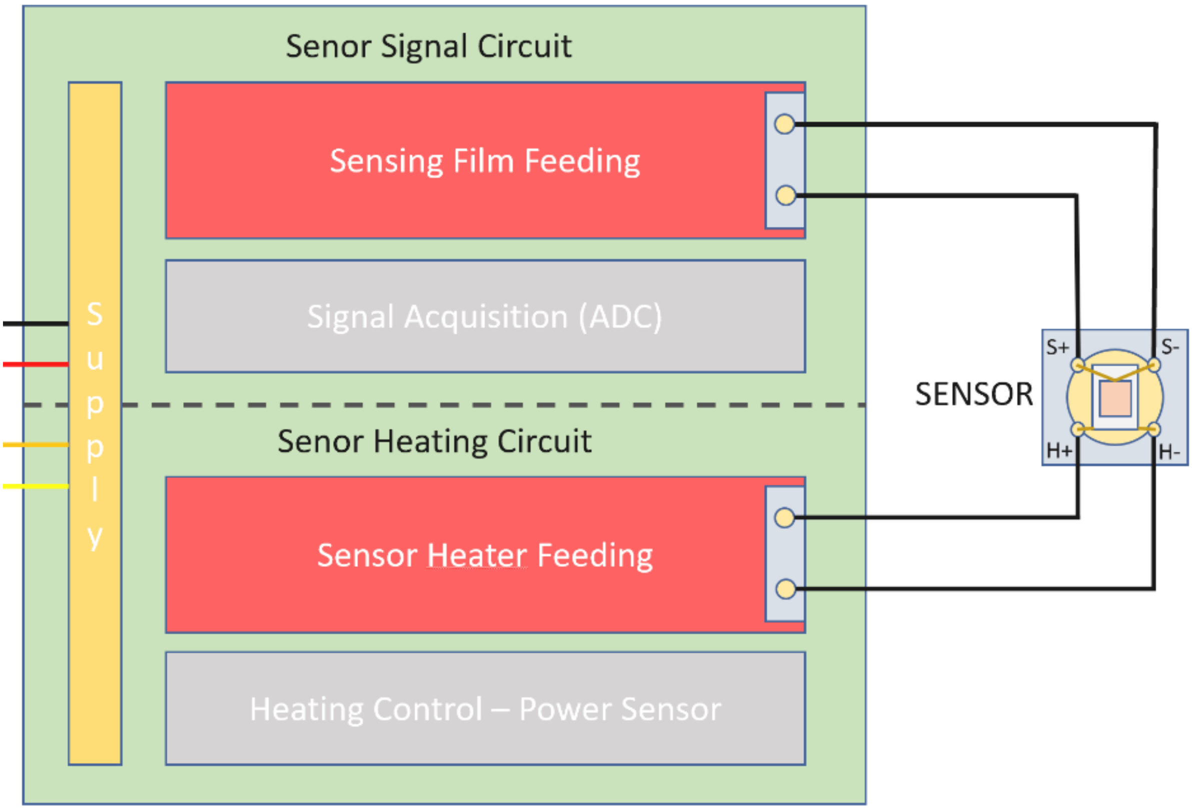

Figure 5.2.2: Block scheme sketch of a sensor supply board. It is divided into two parts: a sensor signal circuit, concerning the sensor sensing film feeding and the resulting signal acquisition; a sensor heating circuit, consisting in the heater feeding and a complementary unit to control the power directed to it, so ensuring its right tuning.

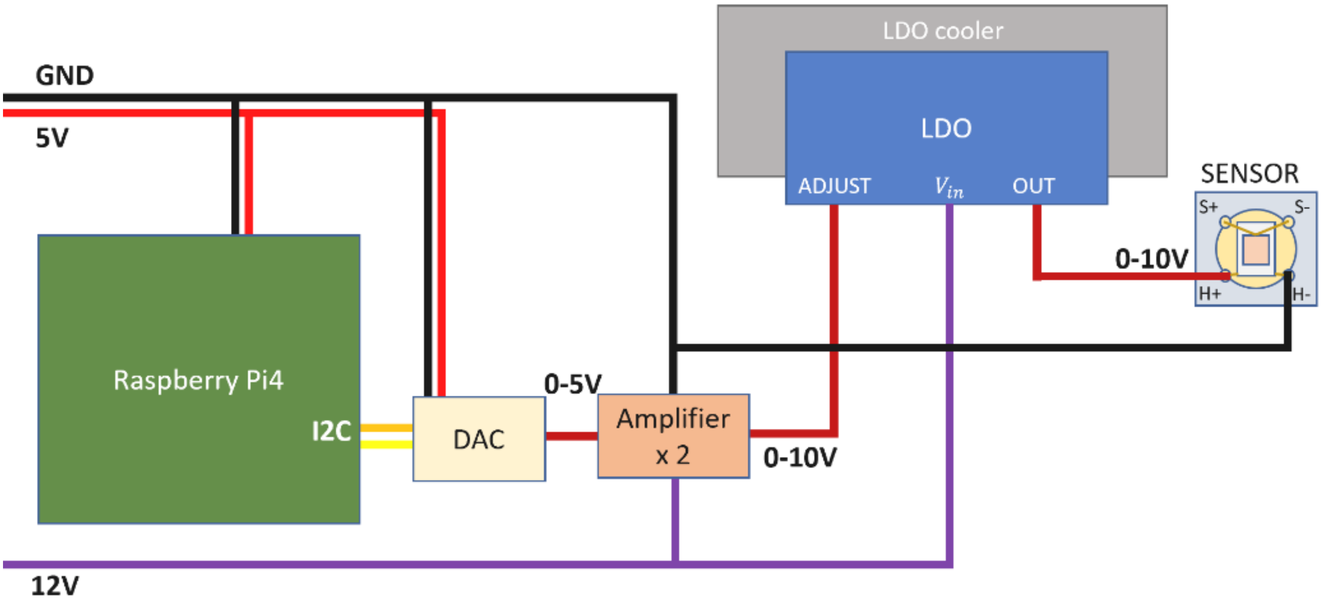

Figure 5.2.3: Block diagram of the sensor heater feeding.

The sensing film is supplied with a 5V accurately filtered low-noise signal (figure 5.2.4a). To transduce the sensor conductance variations, due to sensing mechanism detailed in Chapter 1 and 2, an operational amplifier in inverting configuration is employed (here an AD823N, produced by Analog Devices). Besides to amplify and further filter the sensor signal (low-pass active filter configuration), its output signal appears to be directly proportional to three parameters: the sensor conductance, the feedback resistance and the input voltage (as asserted by the figure 5.2.4a formula). This configuration results crucial to obtain a very clean and stable signal, where the values of R_{feed} and C_{feed}, representing the low-pass filtering RC circuit, must be carefully defined, considering the sampling frequency and the sensing film resistance. The sensor signal acquisition is based on the use of a precision analog-to-digital converter (ADC) IC module (here an ADS1115, produced by Texas Instruments). It converts a voltage signal ranging from 0 to 5 V with 65000 digital steps, ensuring an acquisition resolution of about 76 μV (figure 5.2.4b).

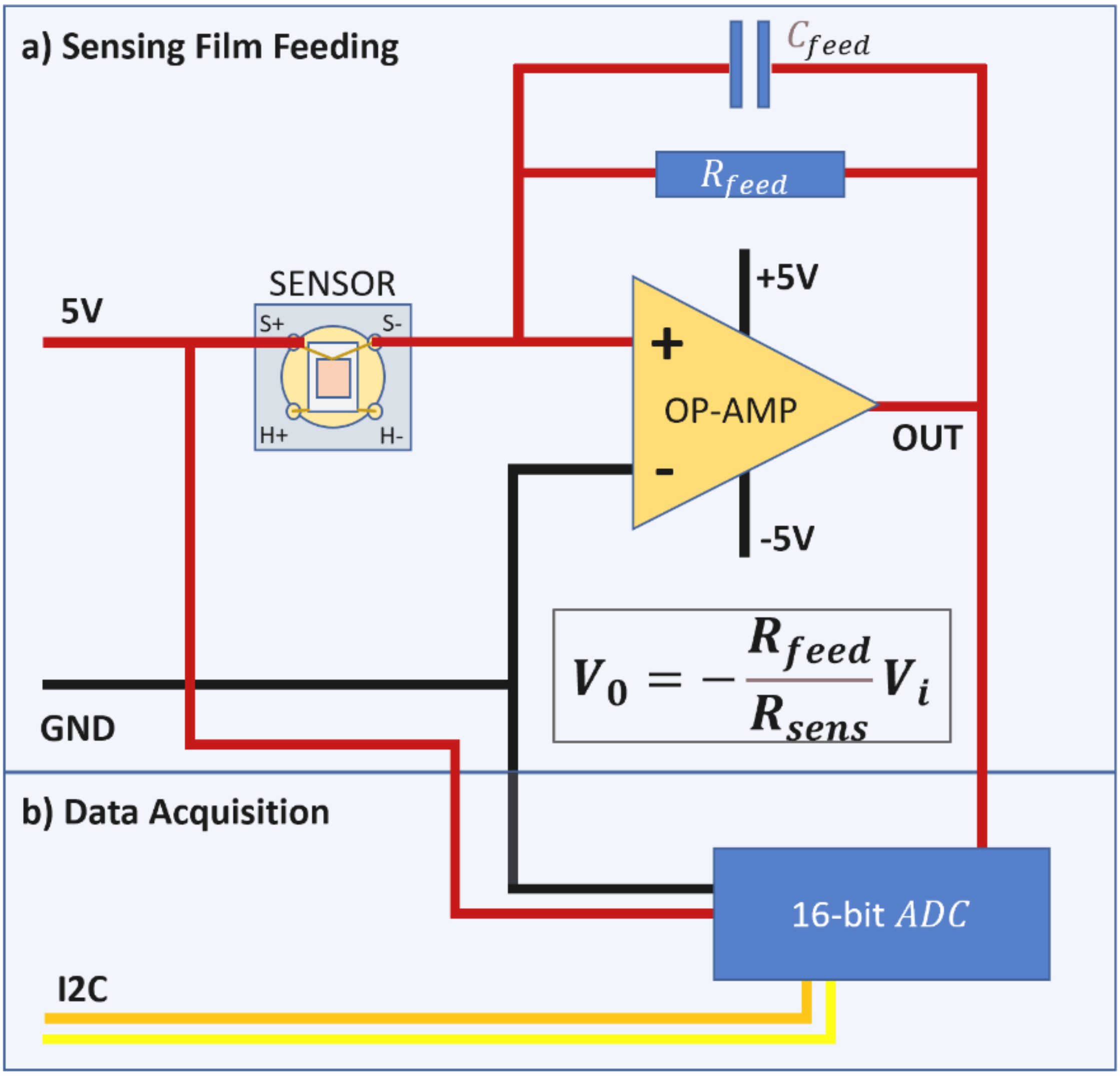

Figure 5.2.4: Block diagram of: a) sensor sensing film feeding and, b) 16-bit data acquisition system.

A single sensor channel electronics has been realized as a test, welding by hand the boards and making the electronic components interchangeable to define their best arrangement (figure 5.2.5), to produce the definitive printed circuit board (PCB).

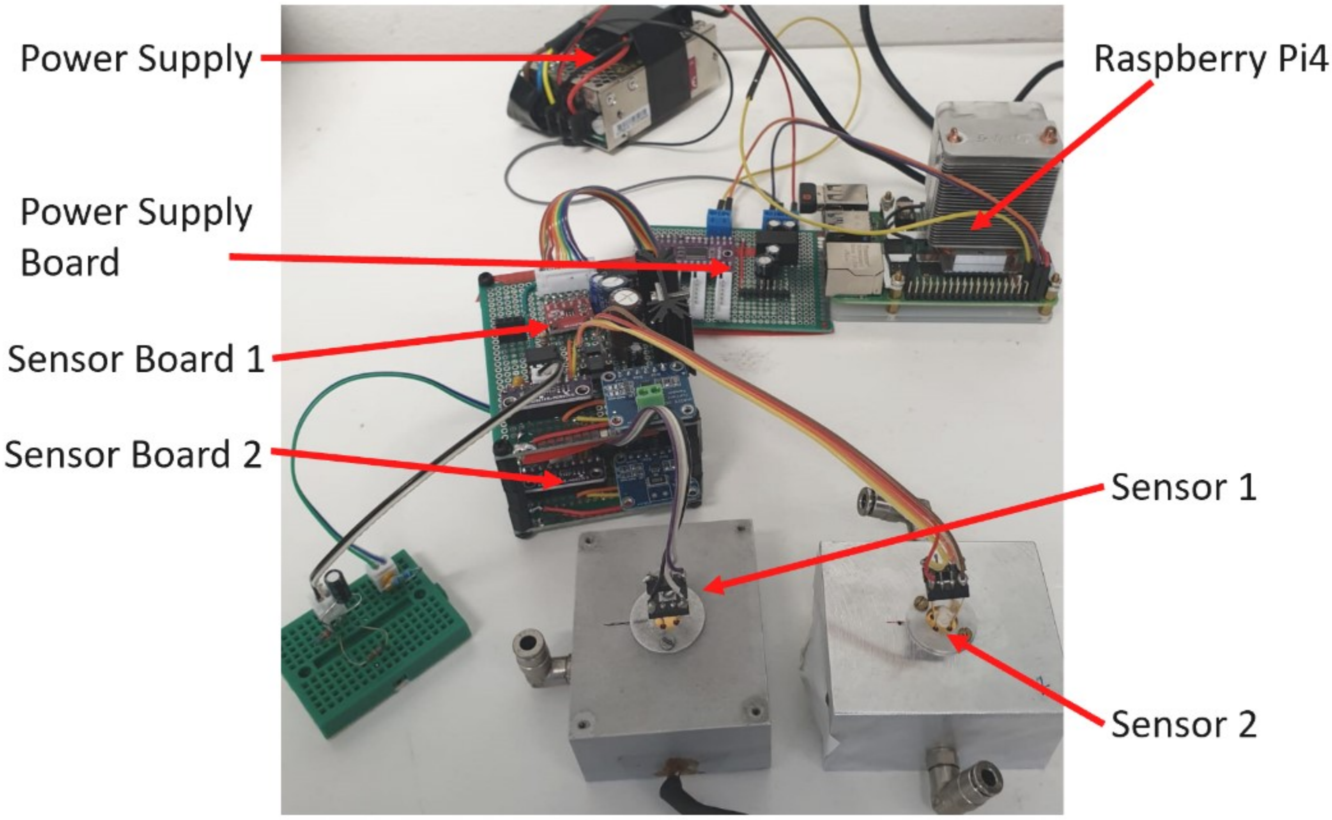

Figure 5.2.5: Single sensor channel by hand welded test electronics.

After two months of test, it demonstrated a good stability, a very low noise and a high signal-to-noise ratio. Figure 5.2.6. shows an example of sensor stabilization signal in air and at room temperature, carried out with a ZnO, i.e., Zinc-Oxide, and a $TiTaV$, i.e., Tin, Titanium and Vanadium Oxide, sensors. As evidenced, the electronic ripple is almost completely absent and the sensor signals appear straight and stabilized, despite the high amplification applied. The PCB production, on the basis of the test electronics, will be the next step forward in developing a reproducible new device.

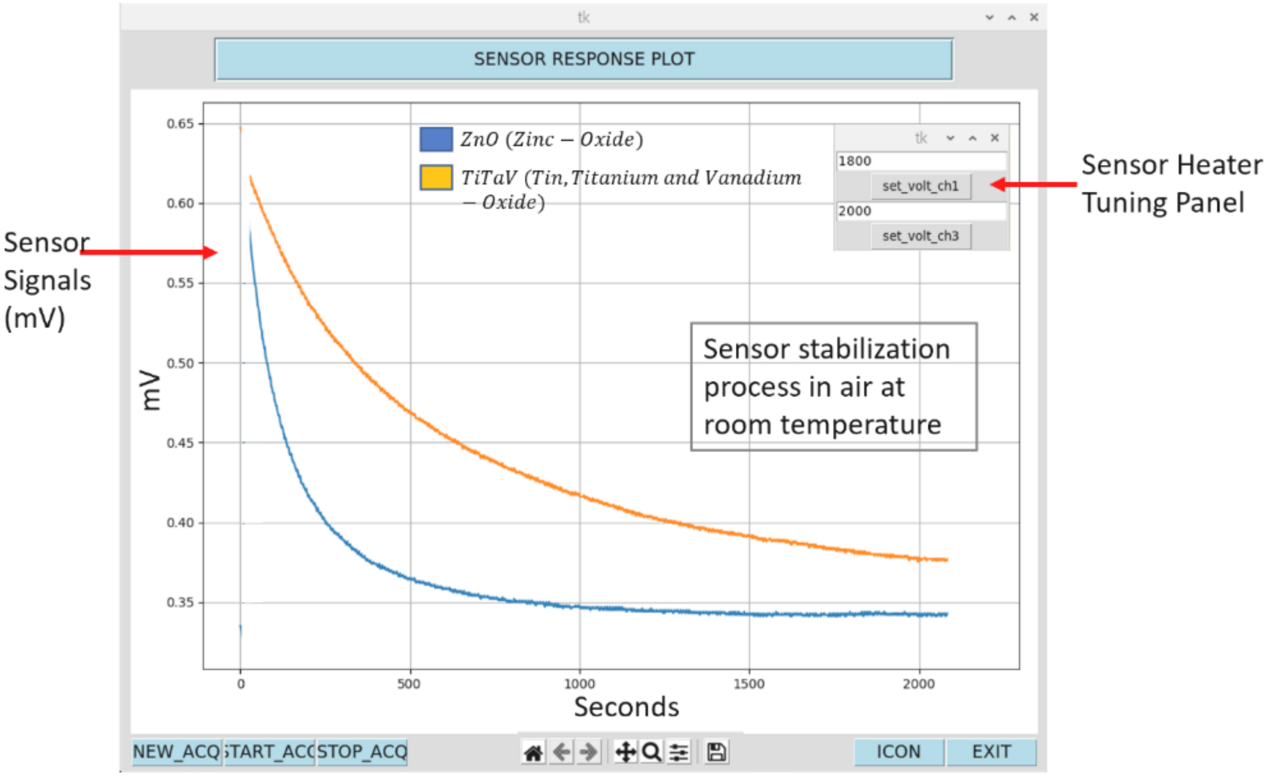

Sensor Signals (mV)

Sensor Heater Tuning Panel

Sensor stabilization process in air at room temperature

Figure 5.2.6: Single sensor channel hand made prototype stabilization signals.

5.3 Management Software

Simultaneously with the electronics development, a new management software has been designed and it is currently under construction. Till now, a basic beta software has been written and tested on the aforementioned test electronics, useful as a basis for the definitive one preparation. It will include different functions and services that, except the electronics management, were missing in the currently used SCENT B1 software. The additional functions consist in an advanced electronics management interface, a data storage (in different formats) and their real time graphing and, the creation of a database of the physical and working features of all the sensors employed in the device history.

- **Advanced electronics management interface.** It consists in the I2C serial interface protocol exploitation to control and interfere with the electronics with high safety and rapidity levels. The Python programming language has been chosen for these aims, considering its advantages in finding libraries and in the application of code to real cases. Through this language, a user-friendly graphical user interface has been programmed, already containing the sensor information storage and management code(figure 5.3.1).

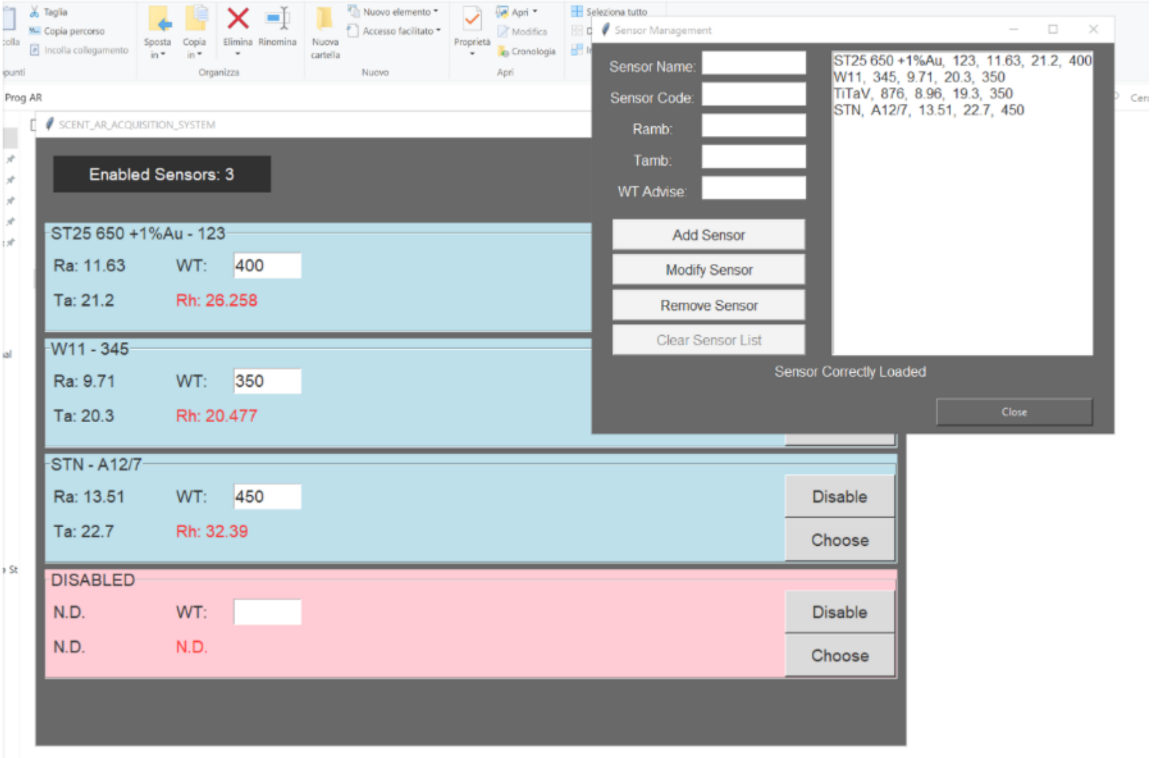

Enabled Sensors: 3

ST25 650 +1%Au - 123
Ra: 11.63 WT: 400
Ta: 21.2 Rh: 26.258

W11 - 345
Ra: 9.71 WT: 350
Ta: 20.3 Rh: 20.477

STN - A12/7
Ra: 13.51 WT: 450
Ta: 22.7 Rh: 32.39

DISABLED
N.D. WT:
N.D. N.D.

Sensor Name:
Sensor Code:
Ramb:
Tamb:
WT Advise:

ST25 650 +1%Au, 123, 11.63, 21.2, 400
W11, 345, 9.71, 20.3, 350
TiTaV, 876, 8.96, 19.3, 350
STN, A12/7, 13.51, 22.7, 450

Sensor Correctly Loaded

Figure 5.3.1: SCENT new prototype graphical user interface. SCENT_AR_ACQUISITION SYSTEM window provides the under-construction interface with the electronics (currently partially working). It permits to activate the required sensor boards and to send the desired sensor settings to the device. The Sensor management window (top-right corner) allows to create a sensor database to record and store all the employed sensors settings and features.

- **Real time data plotting and storage.** It foresees a software section, dedicated to the ADC data acquisition, storage and real time plotting.
  Sensor analog signals are converted into digital ones by means of the 16-bit ADC (previously mentioned) and they are read by Raspberry Pi4 through the I2C serial communication protocol. The acquired data are stored in both a txt file (easily readable by researchers) and in binary format. Then they are plotted in real time on a dedicated plotting window, including some curve handling functions, such as local zoom, graph scale changer, undo and redo, clean graph, etc.
  The intent is to equip the software also with a preliminary data analysis section, where it will be possible to perform some changes and processes on data to assess their quality and reliability.
- **Sensor database and history.** It consists in the creation of a sensor database where the sensor features and working parameters will be listed and kept updated during time in a cloud storage (figure 5.3.2). This procedure should limit the paper consumption and avoid any data loss, besides allowing the data access to the whole research team. Another advantage of this approach will be

the possibility to instantaneously recall all the working parameters of a sensor employed in the past, in the need to employ it again.

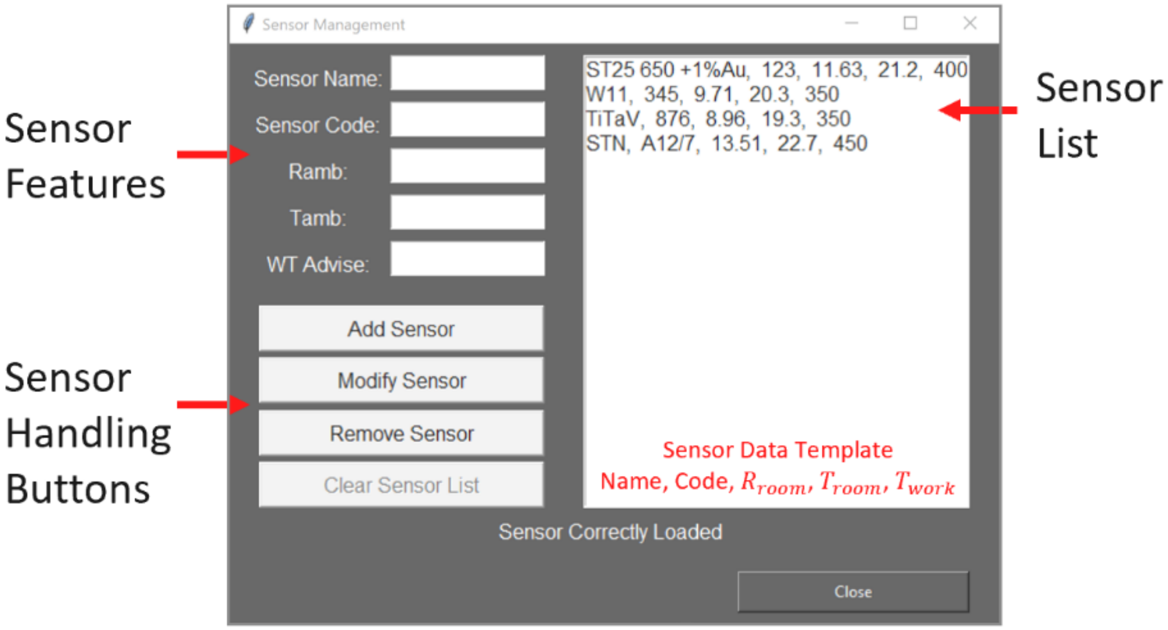

```
ST25 650 +1%Au, 123, 11.63, 21.2, 400
W11, 345, 9.71, 20.3, 350
TiTaV, 876, 8.96, 19.3, 350
STN, A12/7, 13.51, 22.7, 450
```

Sensor Data Template
Name, Code, R_{room}, T_{room}, T_{work}

Sensor Correctly Loaded

Figure 5.3.2: Software section concerning the sensor features and working parameters database.

6 Conclusions

In this thesis work, a discussion concerning the physics of nanostructured semiconductor grains, the thick-film sensor production and their applications for biomedical purposes has been done, to introduce the three-year research. After that it is important to highlight the several results attained during this period, starting with a brief content summary. In the Chapter 1 and 2, the semiconductor physics applied to chemoresistive grains has been explained to underline the potential of these nanotechnologies in the gas detection field. Basing on this knowledge, in Chapter 3, an innovative patented device (SCENT), based on a gas sensor array, has been presented and detailed. This prototype has been employed till now for research purposes in the biomedical field, analysing the complete VOCs spectrum exhaled by biological samples (i.e., feces, human blood, human tissues, cell cultures) with the final aim to detect and classify the CRC-VOCs.

Despite the specificity of this branch, currently it appears very promising for the development of future technologies, capable of improving the current tumor screening protocols. This work is focused only on the detection of the CRC biomarkers, thanks to the multiannual collaboration of SCENT S.r.l research team with the Department of Surgery of the University of Ferrara and the S. Anna Hospital of Ferrara, with the future aim of extending this study to other types of tumor.

The scientific articles presented in the Chapter 4 represent the detailed summary of the analysis performed and the results attained with SCENT device, underlining step by step the whole advances in this research field. The main results achieved are the discrimination between feces, blood and tissues collected from CRC-affected subjects and healthy controls, with high sensitivity and specificity. Concerning the immortalized cell cultures, a cell classification based on the initial plating concentration and the incubation period has been observed by means of SCENT device. This application highlights the capability of this device to monitor the cell health status as a function of their concentration and proliferation rate.

As mentioned at the end of the Chapter 4, a novel research has been started at the end of 2020, where a follow-up protocol has been approved and applied on CRC-affected patients. This protocol foresees the measure of four blood samples per patient, during the whole post-surgery period. This procedure aims to monitor the patient health status and to detect possible relapses. Up to now, twenty patients have been recruited for these tests with the aim of reaching up to forty recruitments within the end of June 2021, encouraged by the brilliant results attained up to now.

The novel device and managing software, detailed in Chapter 5, should be definitively working within June – July 2021 and it will replace the current SCENT B1 prototype to carry on the aforementioned follow-up project.

Since SCENT sensor array interacts with a complex gas mixture, providing an overall output pattern, it will be interesting to study the single components composing the analysed biologic samples. For this reason, a new collaboration with the Department of Chemistry of the University of Ferrara is starting, and it foresees the flanking of SCENT device with a mass spectrometer for liquid analysis. This initiative will be crucial to classify CRC-biomarkers, up to now analysed as a global mixture.

7 References

[1] J. Colinge, «Physics of Semiconductor Devices,» in *Physics of Semiconductor Devices*, New York, Kluwer Academic Pub, 2002, pp. 1-40.

[2] J. Colinge, «Physics of Semiconductor Devices,» in *Physics of Semiconductor Devices*, New York, Kluwer Academic Pub, 2002, pp. 29-30.

[3] J. Colinge, «Physics of Semiconductor Devices,» in *Physics of Semiconductor Devices*, New York, Kluwer Academic Pub, 2002, pp. 31-33.

[4] C. Malagù, V. Guidi, M. Stefancich, M. C. Carotta e G. Martinelli, «Model for Schottky barrier and surface states in nanostructured n-type semiconductors,» *Journal of Applied Physics,* vol. 91, n. 2, pp. 808-814, 2002.

[5] H. Luth, «Solid Surfaces, Interfaces and Thin Films,» in *Solid Surfaces, Interfaces and Thin Films*, New York, Springer, 2001, pp. 265-316.

[6] D. Puzzovio, «Surface Interaction Mechanisms In Metal-Oxide Semiconductors For Alkane Detection,» in *PhD Thesis*, Ferrara, 2006/2008, pp. 1-9.

[7] N. Barsan, C. Simion, T. Heine, S. Pokhrel e U. Weimar, «Modeling of Sensing and transduction for p-type semiconductiong metal oxide based gas sensors,» *Journal of Electroceramics,* pp. 11-19, 2009.

[8] P. Romppainen e V. Lantto, «The effect of microstructure on the height of potential energy barriers in porous tin dioxide gas sensors,» *Journal of Applied Physics,* vol. 63, n. 10, pp. 5159-5165, 1988.

[9] G. Martinelli e M. C. Carotta, «Thick-film gas sensors,» *Sensors and Actuators B: Chemical,* vol. 23, n. 2-3, pp. 157-161, 1995.

[10] A. Gaiardo, B. Fabbri, A. Giberti, V. Guidi, P. Bellutti, C. Malagù, M. Valt, G. Pepponi, S. Gherardi, G. Zonta, A. Martucci, M. Sturaro e N. Landini, «ZnO and Au/ZnO thin films: Room-temperature chemoresistive properties for gas sensing applications,» *Sensors and Actuators B: Chemical,* vol. 237, pp. 1085-1094, 2016.

[11] A. Ponzoni, E. Comini, I. Concina, M. Ferroni, M. Falasconi, E. Gobbi, V. Sberveglieri e G. Sberveglieri, «Nanostructured Metal Oxide Gas Sensors, a Survey of Applications Carried out at SENSOR Lab, Brescia (Italy) in the Security and Food Quality Fields,» *Sensors,* vol. 12, p. 17023–17045, 2012.

[12] C. Wang, L. Yin, L. Zhang, D. Xiang e R. Gao, «Metal Oxide Gas Sensors: Sensitivity and Influencing Factors,» *Sensors,* vol. 10, pp. 2088-2106, 2010.

[13] G. Zonta, G. Anania, M. Astolfi, C. Feo, A. Gaiardo, S. Gherardi, A. Giberti, V. Guidi, N. Landini, C. Palmonari, A. De Togni e C. Malagù, «Chemoresistive sensors for colorectal cancer preventive screening through fecal odor: Double-blind approach,» *Sensors and Actuators B: Chemical,* vol. 3012, p. 127062, 2019.

[14] C. M. Aldao e M. C, «Non-parabolic intergranular barriers in tin oxide and gas sensing,» *Journal of Applied Physics,* vol. 112, n. 2, p. 024518, 2012.

[15] A. Giberti, M. Benetti, M. Carotta, V. Guidi, C. Malagù e G. Martinelli, «Heat exchange and temperature calculation in thick-filmsemiconductor gas sensor systems,» *Sensors and Actuators B: Chemical,* vol. 130, p. 277–280, 2008.

[16] C. J. Brinker e G. W. Scherer, Sol-gel science: the physics and chemistry of sol-gel processing, Academic press, 2013.

[17] H. Abdi e L. J. Williams, «Principal component analysis,» *Wiley interdisciplinary reviews: computational statistics,* vol. 2, n. 4, pp. 433-459, 2010.

[18] L. Wang, Support vector machines: theory and applications, Berlin: Springer Science & Business Media, 2005.

[19] K. .. Hajian-Tilaki, «Receiver Operating Characteristic (ROC) Curve Analysis for Medical Diagnostic Test Evaluation,» *Caspian Journal of Internal Medicine,* vol. 4, n. 2, p. 627, 2013.

[20] M. Astolfi, G. Rispoli, G. Anania, V. Nevoso, E. Artioli, N. Landini, M. Benedusi, E. Melloni, P. Secchiero, V. Tisato, G. Zonta e C. Malagù, «Colorectal Cancer Study with Nanostructured Sensors: Tumor Marker Screening of Patient Biopsies,» *Nanomaterials,* vol. 10, n. 4, p. 606, 2020.

[21] N. Landini, G. Anania, M. Astolfi, B. Fabbri, V. Guidi, G. Rispoli, M. Valt, G. Zonta e C. Malagù, «Nanostructured Chemoresistive Sensors for Oncological Screening and Tumor Markers Tracking: Single Sensor Approach Applications on Human Blood and Cell Samples,» *Sensors,* vol. 20, n. 5, p. 1411, 2020.

[22] M. Astolfi, G. Rispoli, G. Anania, E. Artioli, V. Nevoso, G. Zonta e C. Malagù, «Tin, Titanium, Tantalum, Vanadium and Niobium Oxide Based Sensors to Detect Colorectal Cancer Exhalations in Blood Samples,» *Molecules,* vol. 26, n. 2, p. 466, 2021.

[23] S. Gherardi, G. Zonta, M. Astolfi e C. Malagù, «Humidity effects on SnO2 and (SnTiNb)O2 sensors response to CO and two-dimensional calibration treatment,» *Materials Science and Engineering B,* vol. 265, p. 115013, 2021.

[24] G. Zonta, M. Astolfi, D. Casotti, G. Cruciani, B. Fabbri, A. Gaiardo, S. Gherardi, V. Guidi, N. Landini, M. Valt e C. Malagù, «Reproducibility tests with zinc oxide thick-film sensors,» *Ceramics International,* vol. 46, n. 5, pp. 6847-6855, 2020.